

**DESIGN, DEVELOPMENT AND CONTROL OF A NEW
GENERATION HIGH PERFORMANCE LINEAR ACTUATOR FOR
PARALLEL ROBOTS AND OTHER APPLICATIONS**

By

© Md Toufiqul Islam

A thesis submitted to the School of Graduate Studies
in partial fulfillment of the requirement for the degree of
Master of Engineering

Faculty of Engineering and Applied Science

Memorial University of Newfoundland

May, 2016

St. John's, Newfoundland, Canada

ABSTRACT

The main focus of this research is to design and develop a high performance linear actuator based on a four bar mechanism. The present work includes the detailed analysis (kinematics and dynamics), design, implementation and experimental validation of the newly designed actuator. High performance is characterized by the acceleration of the actuator end effector. The principle of the newly designed actuator is to network the four bar rhombus configuration (where some bars are extended to form an X shape) to attain high acceleration.

Firstly, a detailed kinematic analysis of the actuator is presented and kinematic performance is evaluated through MATLAB simulations. A dynamic equation of the actuator is achieved by using the Lagrangian dynamic formulation. A SIMULINK control model of the actuator is developed using the dynamic equation. In addition, Bond Graph methodology is presented for the dynamic simulation. The Bond Graph model comprises individual component modeling of the actuator along with control. Required torque was simulated using the Bond Graph model. Results indicate that, high acceleration (around 20g) can be achieved with modest (3 N-m or less) torque input.

A practical prototype of the actuator is designed using SOLIDWORKS and then produced to verify the proof of concept.

The design goal was to achieve the peak acceleration of more than 10g at the middle point of the travel length, when the end effector travels the stroke length (around 1 m). The actuator is primarily designed to operate in standalone condition and later to use it in the 3RPR parallel robot.

A DC motor is used to operate the actuator. A quadrature encoder is attached with the DC motor to control the end effector. The associated control scheme of the actuator is analyzed and integrated with the physical prototype. From standalone experimentation of the actuator, around 17g acceleration was achieved by the end effector (stroke length was 0.2m to 0.78m). Results indicate that the developed dynamic model results are in good agreement.

Finally, a Design of Experiment (DOE) based statistical approach is also introduced to identify the parametric combination that yields the greatest performance. Data are collected by using the Bond Graph model. This approach is helpful in designing the actuator without much complexity.

ACKNOWLEDGEMENT

First and foremost, all praise to God, the most gracious and merciful who gave me the opportunity and patience to carry out this research work.

I would like to express my sincerest gratitude to my academic supervisor, Dr. Luc Rolland for his invaluable guidance, supervision and constant encouragement throughout this research work. Working with him was a great learning experience and indeed without his assistance and support, this thesis would not have been completed.

Sincere thanks to all the members of High Performance Robotics Research group, Memorial University for their valuable suggestions and help during this work.

This investigation has been funded by Research and Development Corporation (RDC). I am grateful to them for their financial support.

I would like to extend my gratitude to my parents, wife and brother for their inspiration and motivation in my higher study.

TABLE OF CONTENTS

ABSTRACT.....	ii
ACKNOWLEDGEMENTS.....	iv
TABLE OF CONTENTS.....	v
LIST OF TABLES.....	xi
LIST OF FIGURES.....	xii
LIST OF SYMBOLS.....	xix
Chapter 1 Introduction.....	1
1.1 Motivation and Background.....	2
1.2 Requirements for the New Actuator.....	3
1.3 Objectives.....	4
1.4 Thesis Outlines.....	4
Chapter 2 Literature Review.....	6
2.1 Introduction.....	6
2.2 Actuator Classifications.....	7
2.2.1 Hydraulic Actuator	7
2.2.2 Pneumatic Actuator.....	9
2.2.3 Linear Motors.....	11
2.2.4 Electrostatic Linear Motors.....	12
2.2.5 Pneumatic Artificial Muscles (PAMs) Actuators.....	14

2.2.6	Mechanical Actuators.....	15
2.2.7	Micro and Nano Actuators.....	16
2.2.8	Actuator using piezo elements.....	17
2.2.9	Actuator Based on Parallel Mechanisms.....	18
2.2.10	Magnetically Levitated Planar Actuator.....	19
2.2.11	Voice Coil Actuator.....	20
2.2.12	Unconventional Actuator.....	20
2.3	Brief History of Straight Line Mechanisms	21
2.4	Effective Solutions.....	22
2.5	Final Decision.....	24
Chapter 3 Scissor Lift as Linear Actuator.....		25
3.1	Introduction.....	25
3.2	Kinematic Analysis of the Mechanism.....	27
3.3	Dynamic Analysis of the Mechanism.....	29
3.3.1	Bond Graph Model of Each Link.....	30
3.3.2	Parasitic Stiffness and Damping.....	32
3.3.3	Motor Modeling.....	33
3.3.4	Control Mechanism.....	34
3.3.5	Simulation.....	37
3.3.6	Result Interpretation.....	40

3.4	Parametric Design Optimization using DOE.....	40
3.4.1	Experimental Factors and Responses.....	41
3.4.2	Fractional Factorial Design of the Experiment.....	42
3.4.3	Analysis of Experimental Data.....	43
3.4.4	Pareto Chart and Half Normal Plot.....	45
3.4.5	ANOVA analysis and Regression Model.....	46
3.4.6	Residual Analysis.....	46
3.4.7	Interactions.....	50
3.4.8	Model Optimization.....	54
3.5	Discussions.....	54
 Chapter 4 Kinematic Analysis of the Actuator.....		55
4.1	Introduction.....	55
4.2	Kinematic Formulation.....	56
4.3	Singularity Analysis	58
4.4	Range of Motion	57
4.5	Encumbrance.....	61
4.6	Networking of Rhombus Configuration.....	60
4.7	Motion Analysis.....	65
4.8	Discussions.....	66
 Chapter 5 Lagrangian Dynamic Analysis of the Actuator.....		67
5.1	Introduction.....	67

5.2	Lagrangian Formulation for Single Network.....	68
5.2.1	Lagrangian Function.....	69
5.2.2	Lagrangian Analysis.....	70
5.3	Lagrangian Formulation for Double Network	78
5.4	Discussions.....	94
Chapter 6 Bond Graph Dynamic Analysis of the Actuator.....		95
6.1	Introduction.....	95
6.2	Bond Graph Modeling.....	96
6.2.1	Control Mechanism.....	96
6.2.2	Torque Transmission System.....	98
6.3	End Effector Loading	99
6.4	Simulation.....	100
6.4.1	Simulation Properties.....	100
6.4.2	Simulation Parameters.....	101
6.5	Result Interpretation.....	123
6.6	Discussions.....	123
Chapter 7 Practical Design and Calculations.....		124
7.1	Introduction.....	124
7.2	Bar Length Calculation.....	124
7.3	Workspace and Encumbrance Calculation.....	126
7.4	Required Speed Calculation.....	126
7.5	Deflection Calculation.....	128

7.6	Solidworks Model.....	128
7.7	High Performance Actuator with 3RPR robot.....	135
7.8	Design Recommendations.....	135
Chapter 8 Control of the Actuator.....		137
8.1	Introduction.....	137
8.2	General Control Schematic.....	138
8.3	Control Scheme and Algorithm.....	141
8.4	Simulation and Result Interpretation.....	145
8.5	Practical Controller Implementation.....	148
Chapter 9 DOE Data Analysis and Design Optimization.....		154
9.1	Introduction.....	154
9.2	Experimental Factors and Responses.....	155
9.3	Optimal (custom) Design of the Experiment.....	156
9.4	ANOVA Analysis and Regression Model.....	157
9.5	Residual Analysis.....	158
9.6	Model Transformation.....	160
9.7	Model Optimization.....	163
9.8	Discussions.....	164
Chapter 10 Contributions and Future Work.....		165
10.1	Contributions.....	165
10.2	Future Works.....	167

Appendix A: Bond Graph and Motor Specifications	169
Appendix B: Introduction to Design of Experiment (DOE) and Term Definitions	173
Appendix C: Controller Specification and Sample MATLAB code	176
References	183

LIST OF TABLES

Table 3.1	Scissor Lift Simulation Results.....	37
Table 6.1	Dynamic Simulation Properties for Actuator.....	101
Table 6.2	Dynamic Simulation Summary (Horizontal Simulation).....	122
Table 6.3	Dynamic Simulation Summary (Vertical Simulation).....	123
Table 8.1	Motor Specifications.....	148
Table 8.2	Encoder Specifications.....	149
Table 8.3	Control Performance Summary.....	153
Table 9.1	ANOVA Analysis.....	157
Table 9.2	ANOVA Analysis after Transformation.....	160
Table 9.3	Optimization Run.....	164

LIST OF FIGURES

Figure 2.1	Schematic of a Typical Hydraulic Actuator.....	8
Figure 2.2	3D view of the EHA.....	8
Figure 2.3	Double Pneumatic Cylinder Tool.....	9
Figure 2.4	Deburring Robot.....	10
Figure 2.5	Schematic of a Linear Actuator.....	12
Figure 2.6	Electrostatic Motor Structure.....	13
Figure 2.7	Driving Principle.....	13
Figure 2.8	PAM bladder and PAM robot arm.....	15
Figure 2.9	Rack and Pinion.....	16
Figure 2.10	ECF Micro Motors.....	17
Figure 3.1	Basic Construction of a 2 stage Scissor Lift Mechanism.....	26
Figure 3.2	Kinematic Analysis Figure.....	27
Figure 3.3	Schematic of a Single Link.....	30
Figure 3.4	Bond Graph of a Single Link.....	32
Figure 3.5	Parasitic Stiffness and Damping.....	33
Figure 3.6	DC Motor Circuit Diagram.....	33
Figure 3.7	DC motor schematic:	
	(a) Bond Graph of DC motor with motor shaft.....	34
	(b) DC motor gear ratio representation.....	34
Figure 3.8	Control Schematic:	

	(a) Controller Block.....	35
	(b) Control Simulation of Scissor Lift.....	35
Figure 3.9	Bond Graph Model of Scissor Lift Mechanism with 2 rhombus stages...36	
Figure 3.10	Simulation for Upward Movement (Desired Height = 2.5 m, Initial Height = 2.0 m).....	38
Figure 3.11	Simulation for Downward Movement (Desired Height = 1.5 m, Initial Height = 2.0 m).....	39
Figure 3.12	Alliased terms including run list and Data for Experiment.....	44
Figure 3.13	Effect List.....	44
Figure 3.14	Pareto Chart.....	45
Figure 3.15	Half Normal Plot.....	45
Figure 3.16	ANOVA Table with Summary.....	47
Figure 3.17	Regression Model.....	48
Figure 3.18	Normal Plot.....	46
Figure 3.19	Residuals vs. Predicted Plot.....	49
Figure 3.20	Residuals vs. Run Plot	49
Figure 3.21	Box-Cox plot for Power Transformation.....	50
Figure 3.22	Single Factor Interaction Graph.....	52
Figure 3.23	Two Factors Interactions.....	53
Figure 3.24	Optimization Runs for Validation.....	53
Figure 4.1	Four bar Rhombus.....	56
Figure 4.2	Rhombus Extreme Positions.....	60

Figure 4.3	The Rhombus Encumbrance.....	62
Figure 4.4	Double Rhombus and Tripple Rhombus Configurations.....	63
Figure 4.5	Single Network Rhombus Kinematic Performance.....	65
Figure 4.6	Double Network Rhombus Kinematic Performance	66
Figure 5.1	Four bar Rhombus Configuration for Dynamic Analysis.....	68
Figure 5.2	Four bar Double Network Rhombus Configuration for Dynamic Analysis.....	78
Figure 6.1	(a) Input angle of the actuator (Network # 3).....	97
	(b) Control Schematic.....	97
Figure 6.2	Torque Transmission Schematic	
	(a) Bond Graph.....	98
	(b) Physical Model.....	98
Figure 6.3	End Effector Load Simulation.....	99
Figure 6.4	Bond Graph Schematic of the System (Network # 1: Horizontal).....	102
Figure 6.5	Simulation Graph of the System(Network # 1: Horizontal)	
	(a) 3D Schematic.....	103
	(b) Dynamic Behavior.....	103
Figure 6.6	Bond Graph Schematic of the System (Network # 1: Vertical).....	104
Figure 6.7	Simulation Graph of the System(Network # 1: Vertical)	
	(a) 3D Schematic.....	105
	(b) Dynamic Behavior.....	105
Figure 6.8	Bond Graph Schematic of the System (Network # 2: Horizontal).....	106

Figure 6.9	Simulation Graph of the System(Network # 2: Horizontal)	
	(a) 3D Schematic.....	107
	(b) Dynamic Behavior.....	107
Figure 6.10	Bond Graph Schematic of the System (Network # 2: Vertical).....	108
Figure 6.11	Simulation Graph of the System(Network # 2: Vertical)	
	(a) 3D Schematic.....	109
	(b) Dynamic Behavior.....	109
Figure 6.12	Bond Graph Schematic of the System (Network # 3: Horizontal).....	110
Figure 6.13	Simulation Graph of the System(Network # 3: Horizontal)	
	(a) 3D Schematic.....	111
	(b) Dynamic Behavior.....	111
Figure 6.14	Bond Graph Schematic of the System (Network # 3: Vertical).....	112
Figure 6.15	Simulation Graph of the System(Network # 3: Vertical)	
	(a) 3D Schematic.....	113
	(b) Dynamic Behavior.....	113
Figure 6.16	Bond Graph Schematic of the System (Network # 4: Horizontal).....	114
Figure 6.17	Simulation Graph of the System(Network # 4: Horizontal)	
	(a) 3D Schematic.....	115
	(b) Dynamic Behavior.....	115
Figure 6.18	Bond Graph Schematic of the System (Network # 4: Vertical).....	116
Figure 6.19	a) Simulation Graph of the System(Network # 4: Vertical)	
	b) 3D Schematic.....	117

	c) Dynamic Behavior.....	117
Figure 6.20	Bond Graph Schematic of the System (Network # 5: Horizontal).....	118
Figure 6.21	a) Simulation Graph of the System(Network # 5: Horizontal)	
	b) 3D Schematic.....	119
	c) Dynamic Behavior.....	119
Figure 6.22	Bond Graph Schematic of the System (Network # 5: Vertical).....	120
Figure 6.23	Simulation Graph of the System(Network # 5: Vertical)	
	(a) 3D Schematic.....	121
	(b) Dynamic Behavior.....	121
Figure 7.1	Long Bar with Dimensions	125
Figure 7.2	Maximum Velocity and Acceleration Curve.....	127
Figure 7.3	Motor Stator Bar.....	129
Figure 7.4	Rotor Shaft Bar.....	129
Figure 7.5	Upper Bar (Short and Long).....	130
Figure 7.6	Lower Bar.....	130
Figure 7.7	Bearings and Shoulder Screw Assembly.....	131
Figure 7.8	Actuator Assembly.....	131
Figure 7.9	Fixed Base.....	132
Figure 7.10	Base Flange.....	132
Figure 7.11	Base Connector.....	133
Figure 7.12	Base Assembly.....	133
Figure 7.13	Actuator and Base Assembly.....	134

Figure 7.14	Actuator Prototype.....	134
Figure 7.15	Schematic of a 3RPR parallel robot.....	135
Figure 8.1	Block Diagram of Actuator Control.....	138
Figure 8.2	Controller Block Diagram.....	138
Figure 8.3	Schematic of a H bridge drive.....	139
Figure 8.4	Microcontroller-Encoder flow Diagram.....	140
Figure 8.5	Electrical Model of the Actuator.....	143
Figure 8.6	General Block Diagram of Actuator Control.....	143
Figure 8.7	Simulation Diagram of Direct PID Control.....	144
Figure 8.8	Desired Position and Actual Trajectory.....	145
Figure 8.9	Desired Angle and Actual Angle.....	146
Figure 8.10	End Effector Velocity.....	146
Figure 8.11	End Effector Acceleration.....	147
Figure 8.12	Trajectory Error.....	147
Figure 8.13	Phidget Controller.....	150
Figure 8.14	Linear Actuator with Controller.....	151
Figure 8.15	Controller Connection Window.....	151
Figure 8.16	Controller Performance Window.....	152
Figure 9.1	Run Data.....	156
Figure 9.2	Box-Cox Plot.....	159
Figure 9.3	Mathematical Equation for Output.....	161
Figure 9.4	Normal Plot of Residuals (with inverse square root transformation).....	161

Figure 9.5	Residuals vs. Actual Plot (with inverse square root transformation).....	162
Figure 9.6	Residuals vs. Run Plot (with inverse square root transformation).....	162
Figure 9.7	Box-Cox Plot (with inverse square root transformation).....	163

LIST OF SYMBOLS

K_S	Sensor Stiffness
d_S	Sensor Damping
m_a	Actuator Piston Mass
m_e	Environmental Mass
d_e	Environmental Damping
K_e	Environmental Stiffness
G_i	Entering Mass Flow
P_i	Chamber Pressure
V_i	Volume of Chamber
A_i	Area of Piston
F_{ek}	External Forces
F_{rk}	Frictional Forces
X_K	Position
m_l	Mass of Each Link
l	Length of Each Link
q_i	Each Joint angle and displacement
θ	Control Angle
θ'	Input Angle of Scissor Lift
h	Height of First Moving Central Joint of Scissor Lift
S	Input Link Length of Scissor Lift
H	Total Height of Scissor Lift Platform

v	Linear Velocity of a Point
r	Linear Distance Between Two Point
R_a	Motor Resistance
L_a	Motor Inductance
J	Rotor Inertia
V_c	Voltage of the Coil
ω	Angular Velocity
x	Linear Distance
α	Angular Acceleration
a	Linear Acceleration
W	Width of Bar
I	Inertia at the Centre of the mass of a link
K	Kinetic energy
L	Lagrangian Function
U	Potential Energy
g	Gravitational Acceleration
R	Damping Element
C	Compliance
TF	Transformer
I	Inertia Element
GY	Gyrator
E	Encumbrance

K_B	Back EMF Constant
F_a	Actuator Force
M	Mass Matrix
N	Non Linear Matrix
G	Gravity Matrix

Chapter 1

Introduction

The linear actuator develops force and provides motion through a straight line. There are different designs and concepts for linear actuator technology to attain high performance in terms of speed, acceleration, precision etc. Based on the working principles, these designs and concepts are broadly categorized (i.e. mechanical, electrical, hydraulic, pneumatic, magnetic etc.). However, very few of these can actually obtain rapid acceleration with modest repeatability for industrial and practical applications.

This thesis presents the design, development and control of a new generation linear actuator based on a four bar mechanism, namely the rhombus configuration. The main concept is to network the rhombus configuration to obtain high performance (rapid acceleration). Like any other parallel mechanism, the proposed architecture is also providing a more rigid linkage compared to the serial mechanisms. The rigidity advantage leads to larger actuator bandwidth, thereby allowing for increased accelerations which result in larger force being applicable to the extremity while keeping the overall mass very low [1].

1.1 Motivation and Background

Over the past few decades actuators have been widely used for motion control of various machines and in industrial automation. An actuator is an energy conversion device that employs one or more energy sources to achieve mechanical motion. Depending on the specific applications, such mechanical motion can be linear, or rotary, or a combination of both (translation and rotation). For many years conventional electric motors played the most important role in the linear actuation technology along with hydraulic and pneumatic systems. Despite important breakthroughs, linear motors are still limited to low accelerations (around 5g) and limited torque [2]. Translation actuators are now widely proposed in parallel robots, such as the Gough platform (often referred to as the Stewart platform) [3]. The available actuators are limited to low acceleration (reaching hardly 2g). There are also alignment problems that are difficult to overcome and create non-linear friction in the translation motion [4].

The key challenge for these actuator technologies is to achieve both high acceleration and precise control simultaneously. The performance of the actuator is mainly represented by the output force, the motion stroke, the mover mass, the power density, etc.

1.2 Requirements for the New Actuator

The major requirements of the newly designed linear actuator are described as follows:

1. The proposed new actuator needs to be compact and mechanically rigid, so that it can be installed on the robots or can work in standalone condition. The actuator will provide enough force to the actuation with very high acceleration (10g or more).
2. The main design will be based on the networking of a four bar rhombus mechanism. The stroke length of the actuator is around 1m.
3. Extremity positions will be having a minimum offset.
4. Actuator acceleration is a more important factor than speed. The desired acceleration is 10g, when the end effector travels the stroke length.
5. Actuator position has to be selected the closest to the base (i.e. non moving joints).
6. An encoder will be connected to the DC motor shaft for position feedback. PID controller will be used to control the actuator.

1.3 Objectives

The major objectives of this thesis include the design, development and control of the newly designed linear actuator. They are described as follows:

1. To design a high performance linear actuator that is able to achieve high acceleration (10g or more).
2. To perform design optimization for the newly designed actuator.
3. To implement the proper control system.
4. To test and characterize the performance of the actuator by experiments.

1.4 Thesis Outline

Chapter 2 summarizes the relevant concepts and advancements pertaining to the linear actuator modeling and control. This chapter also introduces the design concept of the new linear actuator to satisfy the design requirements and goals.

Chapter 3 determines the feasibility of the scissor lift mechanism as prismatic actuator. It includes the dynamic analysis and parametric optimization of the mechanism.

Chapter 4 represents brief kinematic analysis of the four bar rhombus mechanism and their networking formulation.

Chapter 5 provides detailed dynamic analysis of the actuator with different networking performance. Lagrangian analysis has been used to construct the conventional dynamic formulation.

Chapter 6 shows detailed dynamic simulation through bond graph modeling of the newly designed actuator.

Chapter 7 introduces the practical design aspects and associated calculations for the actuator body and the base.

Chapter 8 discusses the detailed control features of the newly designed actuator for forward and backward movement.

Chapter 9 shows the data collection procedure and analysis method for parametric design optimization through DOE (Design of Experiment) procedures.

Chapter 10 outlines the contribution of the research, and discusses more potential applications and suggestions for future work to improve the design.

Chapter 2

Literature Review

2.1 Introduction

An actuator converts energy in a controllable way from one or more external energy sources into mechanical motion. Different mechanisms can be involved in an individual or hybrid actuating device. This chapter describes the most significant linear actuator designs which are currently available.

2.2 Actuator Classifications

For linear actuator design, many concepts have been introduced and used practically based on the requirements and resources available. Still, development of the high performance actuator is recognized as one of the key technologies for the next generation. Based on the available actuators, we can classify them on some broad categories: (1) Power Actuators, (2) Mechanical Actuators, (3) Micro and Nano Actuators, (4) Actuators Based on Parallel Mechanism (5) Actuators for Special Environment, and (6) Unconventional Actuators.

2.2.1 Hydraulic Actuator

Hydraulic actuators are famous for their very high force to weight ratio and very fast response time. These types of actuators are capable of maintaining their loading capacity indefinitely, provided their hydraulic circuit is not leaking. For this property, excessive heat is generated in the electrical components. This is a backdrop for this type of actuator [5]. Figure 2.1 is showing a typical hydraulic actuator with environmental interaction design [6]. The sensor with stiffness k_s and damping d_s connects the actuator piston, represented by the mass m_a , to the environment. The environment is represented by mass m_e , damping d_e , and stiffness k_e . In the hydraulic actuation system, control signals activate the spool valve that controls the flow of the hydraulic fluid. The flow causes a differential pressure build up and this is proportional to the actuator force [6]. Compared to the electrical system, force control is a very difficult problem for the hydraulic actuation system [7, 8].

Hydraulic systems are also highly nonlinear and subject to parameter uncertainty. To resolve the control problem, a quantitative feedback theory (QFT) based control method was proposed by *Navid et al.* (2001). To improve the performance and resolve the drawbacks extensive research is going on the hydraulic actuation system. Electro hydraulic actuators (EHA) are now much more popular instead of only hydraulic actuation system (HAS).

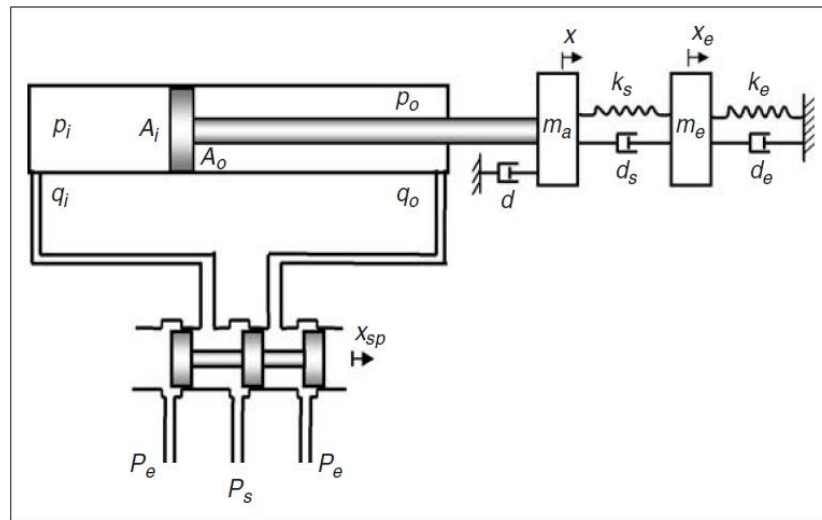


Figure 2.1 Schematic of a Typical Hydraulic Actuator [6]

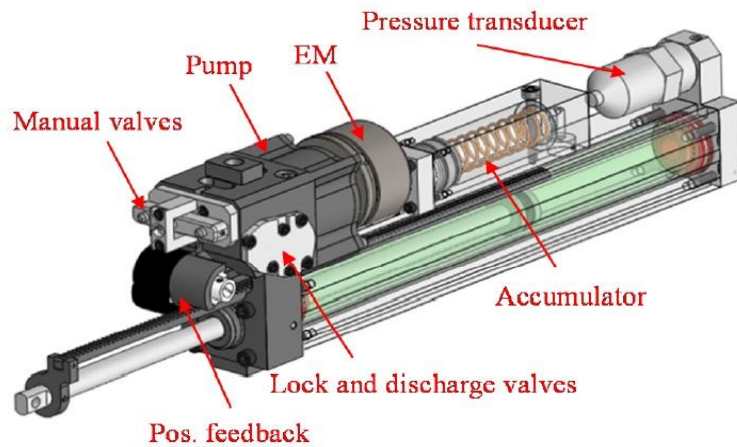


Figure 2.2 3D view of the EHA [9]

EHA's have superior energy efficiency. The use of the compact EHA's, permit to combine the power to weight ratio of hydraulic actuators with the ease of control and wiring advantage of electrical system. *Altare et al. (2014)* proposed a complete EHA system for industrial production [9]. Schematic of the proposed compact EHA system is shown in Figure 2.2.

2.2.2 Pneumatic Actuators

Pneumatic actuators are based on the pneumatic actuation system. This kind of actuator offers several advantages: low cost, high power to weight ratio, ease of maintenance, cleanliness, and having a readily available cheap power source [10]. Actuation system design depends on the application areas. Pneumatic actuators are actually widely used in industrial machines.

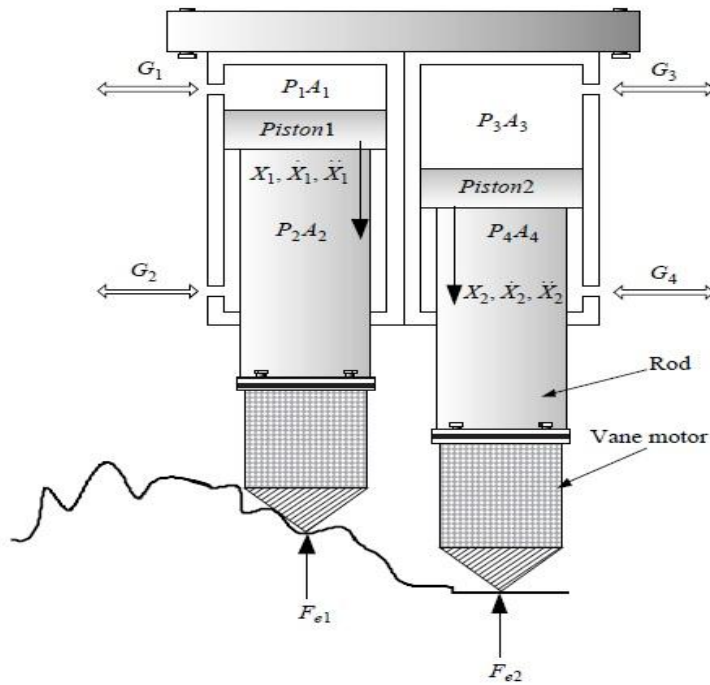


Figure 2.3 Double Pneumatic Cylinder Tool [11]

Figure 2.3 shows a double active pneumatic tools for robotic deburring [11]. In the figure, $i=1, 2, 3, 4$. G_i is the entering mass flow, P_i is the chamber pressure, V_i is the volume of the chamber, A_i is the area of the piston, F_{ek} and F_{rk} are the external and friction forces, respectively, X_k is the position. Further differentiation of X_k gives the velocity and acceleration of the piston, X_0 is the initial position of the piston where, $k = 1; 2$. Pneumatic actuators can also be used in the robotic manipulator. Figure 2.4 shows a robotic manipulator with the pneumatic actuation system [11].

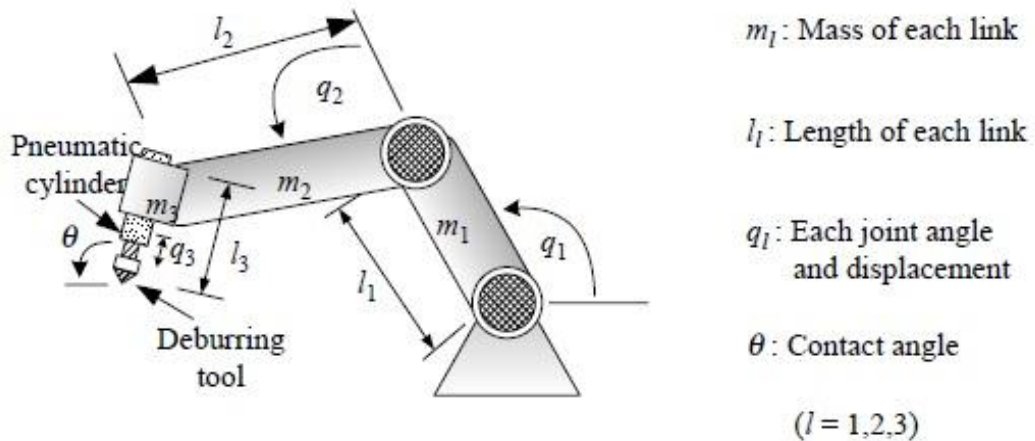


Figure 2.4 Deburring Robot [11]

The pneumatic actuator is hardly used for continuous position control, since it requires very complex secondary control units which are highly non-linear in nature and compressible property of the air introduces flexibility in the system. The best control method for these actuators can be achieved through the hybrid control method, when the actuator is working individually.

However, with the robotic system this control method is not so much effective. Because, hybrid control explicitly controls the position and the force. So, for effective control design one should consider the task space rather than the joint space and actuator space. Still, the control problem limits the use of this type of actuator on the robotic manipulator.

2.2.3 Linear Motors

Linear motor drives are mostly used actuation technology for different applications of machining and automated systems. They can achieve high performance and good resolution, but their configuration for multiple degrees of freedom is difficult to realize. To use them into the parallel structures angular guides are required, which create friction [12]. The friction can be eliminated by the air bearings, leading to enhanced precision [13]. Unfortunately, air bearings have the detrimental behavior that their stiffness varies in relation to the applied load. As the air bearings are exposed to tensile and compression stress, the natural frequencies of the entire system vary in a nonlinear manner. These varying natural frequencies limit the attainable system dynamics, since control theory still has problems in treating them without the loss of bandwidth. Further disadvantages of these solutions are their complex designs (e.g. 3 planar air bearings) and mass resulting from the angular guides, which is to be moved. Magnetization problem is also a great concern for this type of actuator.

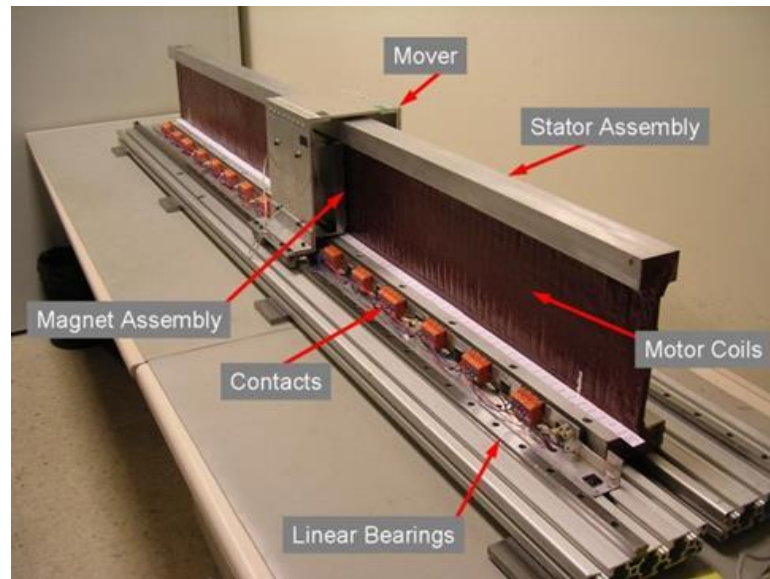


Figure 2.5 Schematic of a Linear Motor [www2.mae.ufl.edu]

2.2.4 Electrostatic Linear Motors

Figure 2.6 shows the basic structure of the electrostatic motor. These motors have been used when the actuation stroke length is not important. The structure consists of slider and stator that are made of a pair of thin plastic films. Both films are made using the flexible printed circuit (FPC) technology. Three-phase parallel electrodes are fabricated in both of them, which are aligned with regular intervals like $200\ \mu\text{m}$ [14, 15]. The two films are stacked without using any linear guides. Thus, the two films are in direct friction when the motor operates. Since, such direct friction causes considerably large loss of thrust force; glass beads with diameter of $20\ \mu\text{m}$ are often inserted between films to reduce friction. In Figure 2.7, by applying three-phase sinusoidal voltage to the three poles of the slider and stator, two potential distributions traveling in opposite directions are excited.

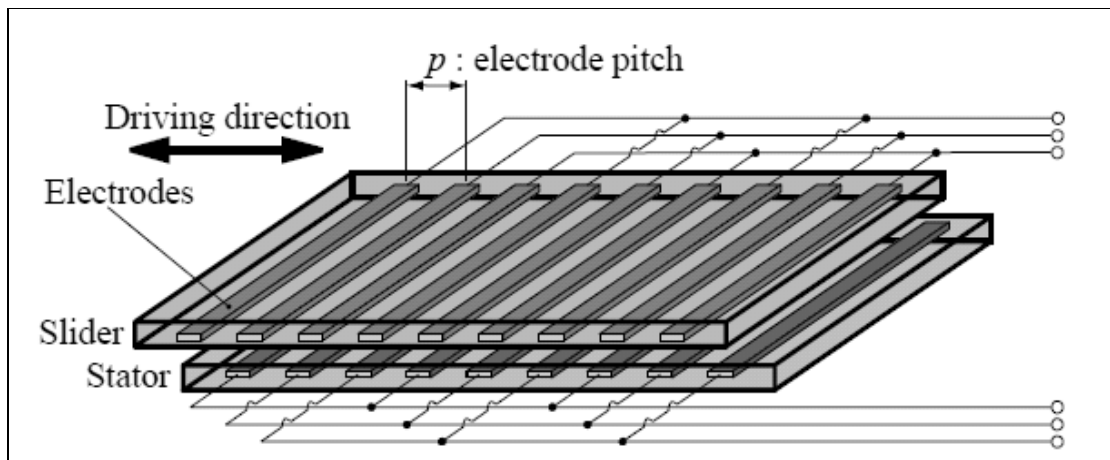


Figure 2.6 Electrostatic Motor Structure [14]

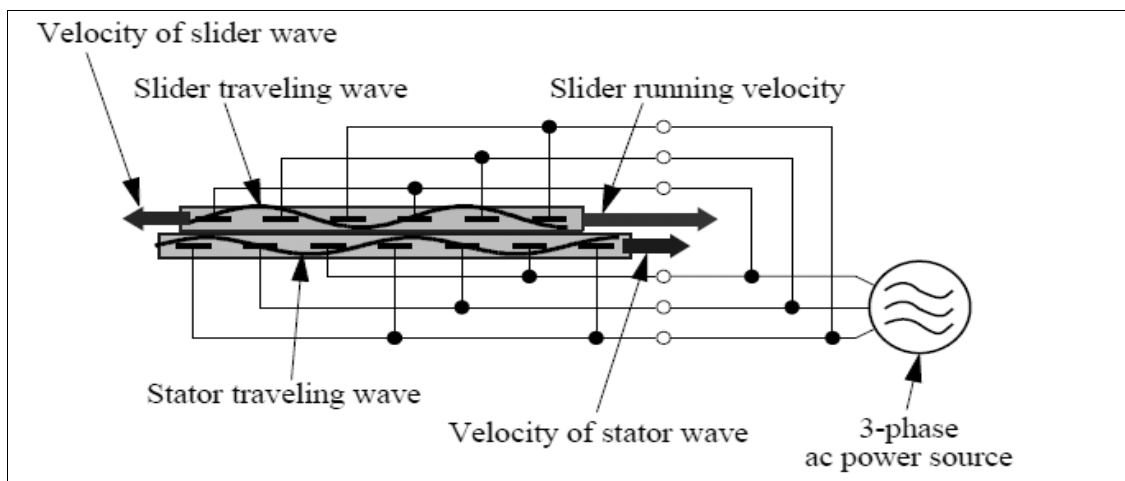


Figure 2.7 Driving Principle [15]

The interaction between those two distributions actuates the slider, so that the spatial phase difference between two distributions is kept at stable phase. This causes the slider to run twice as fast as potential distributions. Thrust force is proportional to the square of amplitude of the applied voltage. It can operate from the lowest applied voltage of around 500V. However, to obtain practical force, it requires higher voltage than 1kV.

With such a high voltage of over 1kV, electric discharge may occur in the atmospheric air, which disturbs the electrostatic field inside the motor and causes improper motor behavior. To prevent such discharge, a dielectric liquid like Fluorinert is used for insulation. Another disadvantage of this system is, the stroke length is not sufficient for machine design where important ranges are required.

2.2.5 Pneumatic Artificial Muscles (PAMs) Actuators

PAMs are new generation actuators. This type of actuator contains electrostatic bladder surface surrounded by a braided sleeve. Applying pressure inside the soft bladder (i.e., inflation) increases the diameter and decreases the length of the actuator through reorientation of the stiff braid fibers, generating a contractile stroke and pulling force similar to human muscle [16]. PAMs can achieve much higher power-to-weight ratios than electrical and hydraulic actuators [17]. They are capable of producing high forces at high speed [18]. No gears are necessary, thus there is no inertia or backlash added to the system. Other benefits of these devices include durability, reliability, operation without precise mechanical alignment, and high force capability at comparably low operational pressures (0_150 psi) [19]. Figure 2.8 shows a typical PAM bladder with braided sleeves and a PAM actuation based robotic arm. The bladder is made of low viscosity additional cure silicone rubber and two end fittings are integrated at the end of the bladder.

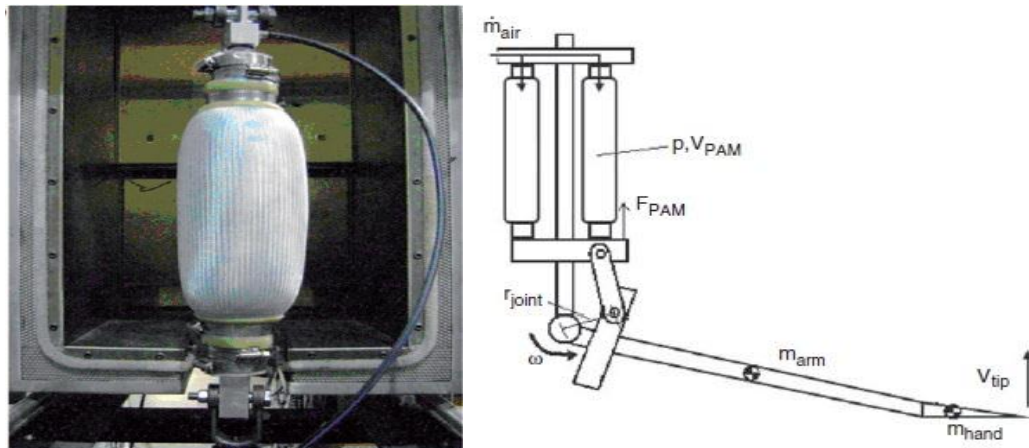


Figure 2.8 PAM bladder and PAM robot arm [16].

Due to the lightweight structure compared to the hydraulic system, use of PAM actuator can add some advantages. Reliability is a great concern for this type of actuator. The actuation principle is mainly based on the pneumatic principle and this actuation is error prone when dealing with large loads. Precise flow control is required for accurate functioning and research is going on the controller design.

2.2.6 Mechanical Actuators

Mechanical linear actuators convert the rotary motion into linear motion (motion in a straight line) of a control knob or handle into linear displacement using the screws and/or gears to which the knob or handle is attached. This type of actuators have great use in the lasers and optics field to manipulate the position of linear stages, rotary stages, mirror mounts, goniometers and other positioning instruments [20]. For accurate and repeatable positioning, index marks may be used on control knobs. Some linear actuator designs include an encoder and digital position readout.

Mechanical actuators can be classified in three broad categories:

1. Machine Screws (lead screw, screw jack, ball screw and roller screw etc.)
2. Wheel and axle (Hoist, winch, rack and pinion, chain drive, belt drive, rigid chain and rigid belt linear actuators etc.)
3. Cam type



Figure 2.9 Rack and pinion [en.wikipedia.org]

Mechanical actuators are very rigid only if they have low backlash. They have a very high load handling capability. Their main disadvantages are their teeth being flexible limiting their accelerations and also often requiring guiding for long strokes (hard to implement without being fixed). Another problem is matching the gears perfectly to avoid backlash and shocks. Cam and plunger often has problem of slip and wear. Plunger also needs guiding that limit its use in robotics. Mechanical actuators are mainly used in the human operated system to ease the workload.

2.2.7 Micro and Nano Actuators

With the advancement of MEMS (micro electro mechanical systems) technologies, many kinds of micro and nano actuators have been developed.

As micro and nano actuators need to be very precise, research is going on to develop the next generation micro and nano actuators. For higher precision, the micro actuator has an advantage that it is allowed to employ various kinds of materials, since the cost of material is not so serious in micro actuators. *Takemura et al.* (1997) proposed a micro motor model with ECF [21]. Electro-conjugate fluid (ECF) is a kind of functional fluid that generates jet flow in high inhomogeneous electric field (Figure 2.10). *Baughman et al.* described an effective design for carbon nanotube actuator [22]. However, this type of actuator is not very popular even in micro application.

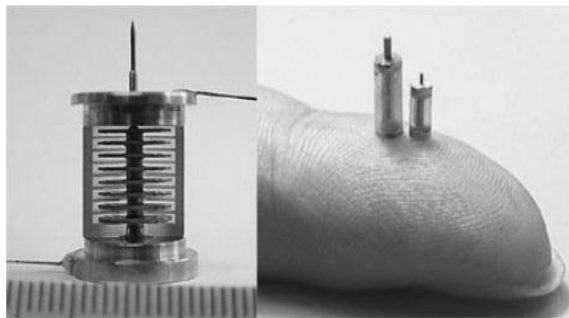


Figure 2.10 ECF Micro motors [21].

2.2.8 Actuators using piezo elements

For precise positioning and resolution from several nanometers to sub microns, piezoelectric elements are the most useful actuators. Piezoelectric actuators are also becoming more and more popular with the development in the MEMS technologies. The motivation of this type of actuator mainly came from three areas [23]. Piezoelectric actuators are commercially used for STM (scanning tunneling microscope) and AFM machine.

The success of STM and AFM proves that this type of actuator can manipulate probes and specimens at an atomic scale. The STM probe positioned with the resolution of nm, even angstroms. Now only the piezoelectric elements can satisfy the nano positioning requirements commercially. For the frequency response, a piezo element itself can deform much faster than usual electric linear motors (i.e. a voice coil motor). So, the piezoelectric element seems to be the most convenient actuator when we need to position a rather small object with high accuracy. On the other hand, the maximum deformation of a piezo element itself is limited to very small, like 10 micrometers for a 10 mm long piezo element. Since the displacement of a piezo itself is limited, several methods have been developed to realize longer or boundless movement by combining some mechanism with piezo elements. The typical mechanisms are “inchworm,” “impact drive mechanism,” [24] and ultrasonic motors [25]. Since PZT contains lead that should be eliminated from all consumer goods. Development of lead-free piezo elements with good property of actuation becomes a serious and urgent problem [26, 27, 28]. The miniature size of this type of actuator provides opportunity to arrange them in several ways.

2.2.9 Actuator Based on Parallel Mechanisms

Fast parallel drives similar to the Delta-Robot [29], have the advantage that their motors are fixed and don't have to be moved. This reduces the moved mass and allows the achievement of high acceleration. But these robots use ball bearings for the joints, which have radial run-out of several μm . The inaccuracy accumulates with each joint of the robot arranged in a chain-like structure.

Other problems are the low stiffness of these structures, the frictional forces in the joints and the complex kinematics and dynamics. All these effects make it difficult to achieve high precision combined with large acceleration. This may be improved when using direct visual feedback, however, the limit cycles resulting from the frictional forces and the speed of image processing will still be the limiting factors. Research is now going on the high performance linear actuator based on the parallel mechanism.

2.2.10 Magnetically Levitated Planar Actuator (MLPA)

MLPAs are alternatives of the xy drive stacked linear motors. The translator of these actuators is suspended above the stator with no support other than the magnetic fields. The gravitational force is fully counteracted by the electromagnetic force. The translator of these ironless planar actuators can move over relatively large distances in the xy plane only, but it has to be controlled in six degrees of freedom (6-DOF) because of the active magnetic bearing. The advantage of the magnetically levitated planar actuators is that they can operate in vacuum (e.g. extreme-UV lithography equipment). Planar actuators can be constructed in two ways. The actuator has either moving coils and stationary magnets [30] or moving magnets and stationary coils [31]–[34]. The last type of planar actuator does not require a cable to the moving part. The change of magnetization between the active coils causes the movement of the translator. The problem of this type of actuator is that the coil at the edge of the magnet can produce significant force and torque. To overcome that problem, current amplifiers were used for the coil with weak force and torque generation capacity [35].

The controller for this type of actuator calculates a force and torque reference or wrench command every sample time. Then this wrench command is converted to the current set points for the power amplifiers.

2.2.11 Voice Coil Actuator

Voice-coil actuators are the simplest form of electric motor. They consist of a non-commutated single coil or winding moving through a fixed magnetic field produced by the stationary permanent magnets. It is generally the end user's responsibility to couple the voice-coil actuator with a linear bearing system, position feedback device, switch-mode or linear servo amplifier, and motion controller. The integration of multiple discrete components adversely affects the system reliability and renders minimization and packaging difficult, particularly when multiple actuators are required. Current voice coil (i.e., linear electric) actuators are simple electromechanical devices that generate precise forces in response to an electrical input signal. Fundamentally, they are the simplest form of electric motor consisting of a non-commutated single coil or winding moving through a fixed magnetic field produced by stationary permanent magnets[36] [37] [38].

2.2.12 Unconventional Actuator

According to the advancements of science and technology, the use of unconventional environments such as super-clean, ultra high vacuum, high temperature and cryogenic environment must be increasing. For the material handling and processing in the unconventional environments, conventional electric motors do not always act well. As a permanent magnet loses its magnetic potential at Curie temperature, conventional

electromagnetic actuators are difficult for use in high temperature. For shape memory alloy actuators, new materials which can work in cryogenic condition [39] and in high temperature [40] have been developed. Combination of direct drive motors and contact free bearings (i.e. magnetic bearings) is a typical solution for super clean environment actuator [41]. If a magnetic field is avoided, electrostatic motor combined with electrostatic levitation seems to be promising [42].

2.3 Brief History of Straight Line Mechanisms

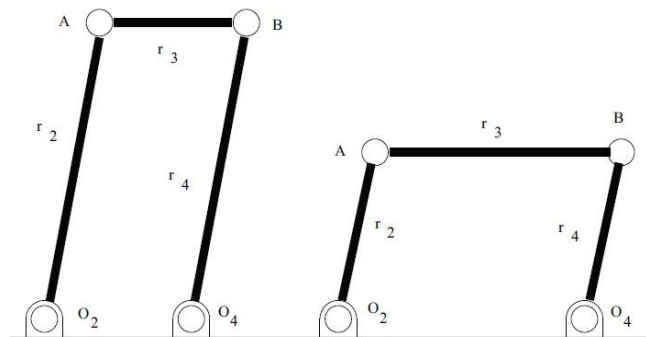
Inventing a straight line mechanism has been the concern for many researchers and engineers even long before the industrial revolution. In seventeenth century, Christopher Scheiner invented the pantograph that may be regarded as the first example of the four bar linkage [43]. In that design, the actuator was located to one end and the device can make a straight line provided that the input follows a straight line. At that time it was extremely difficult to machine the straight and flat surface. Prismatic pair construction without backlash had become difficult and much effort was then devoted towards the straight line motion by linkage coupler contains only revolute joint. Later James Watt proposed a four bar mechanism which was able to generate roughly a straight line. In 1864, Peaucellier introduced the first planar linkage capable of transforming rotary motion into exact straight line motion. After that Grashof linkage also provided exact straight line. A Grashof linkage is a “Crank-Rocker”. The input link rotates through 360 degree while the output rocks back and forth [44]. Then in Hart’s linkage and in A-frame they used only five links to produce straight line motion [3]. The Kmoddl library from

Cornell University presents 39 linkages imagined to produce linear motion [45, 46]. But most of them were relatively complex architecture and difficult to use in robot design. There were several other proposals of linkage designs to produce the straight line motion. Hoekens, Chebyshev, Evens, Roberts and Burmester are few of them. These designs could produce straight lines over some limited range of their motion. The commonality of these mechanisms is most of the designs are based on parallel topology [3].

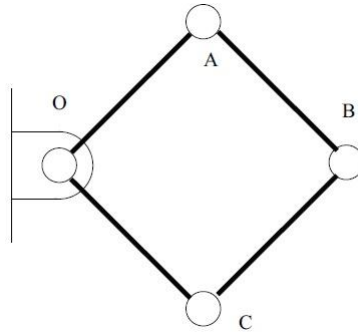
2.4 Effective Solutions:

The simplest forms of parallel mechanisms are the ones producing one degree of freedom. Among these mechanisms there are several classes which can produce straight line motion. Out of these classes some four bar mechanism can produce approximate straight line motion of a point on the coupler, not the coupler itself. So, specific four bar linkage can be made to produce straight line path if they are made with appropriate dimensions and their coupler curves are considered on the link extensions. For designing fast linear actuator from different configuration of four bar mechanism some effective solutions can be:

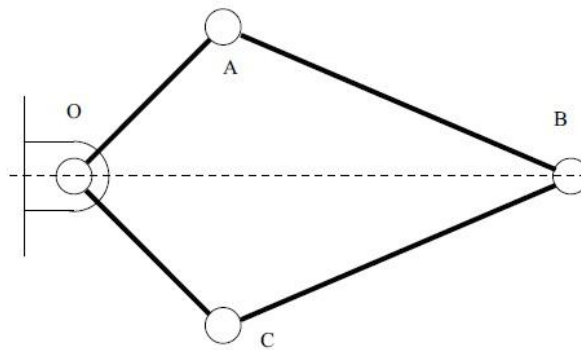
1. The parallelogram configuration



2. The rhombus configuration



3. The kite or diamond configuration



4. Scissor lift mechanism



[Figure Source: highaccessgroup.com.au]

2.5 Final Decision

All the proposed effective solutions are single DOF mechanism. Among these, four bar rhombus configuration was chosen to design the new actuator. Kinematic analysis of the four bar rhombus was performed on the following criteria:

1. Range of Motion
2. Singularity Avoidance
3. Linkage Encumbrance
4. Linearity in Motion Transmission

Chapter 3

Scissor Lift as Linear Actuator

3.1 Introduction

During the development of the newly designed actuator at the very beginning, the scissor lift mechanism was also studied to verify its suitability as a fast linear actuator. Therefore, a proper dynamic model is necessary to investigate the dynamic behavior of the system. This chapter describes the implementation of general multibody system dynamics on the scissor lift Mechanism within a bond graph (Appendix A) modeling framework. There are several methods for deriving the dynamic equations of rigid bodies in classical mechanics (i.e. Classic Newton-D'Alembert, Newton-Euler, Lagrange, Hamilton, Kanes to name a few). But, these are labor-intensive for large and complicated systems and thereby error prone. Here, the multibody dynamics model of the mechanism is developed in bond graph formalism, because it offers flexibility for modeling of closed loop kinematic systems

without any causal conflicts, and control laws can be included. The proposed multibody dynamics model of the mechanism offers a method to analyze the dynamics of the mechanism knowing that there is no such work available for scissor lifts. Figure 3.1 shows the complete system model of a scissor lift mechanism. There is a driving mechanism connected with the lower end of the moving link which is located at the ground platform. The driving mechanism can be electric, hydraulic or pneumatic based on the design criteria. Here, we considered a DC motor as the driving mechanism. It is located at the base and connected with the prismatic link. Design of Experiment (DOE) based statistical approach has been used for optimizing the parametric design and performance (e.g. height) of the scissor lift elevators.

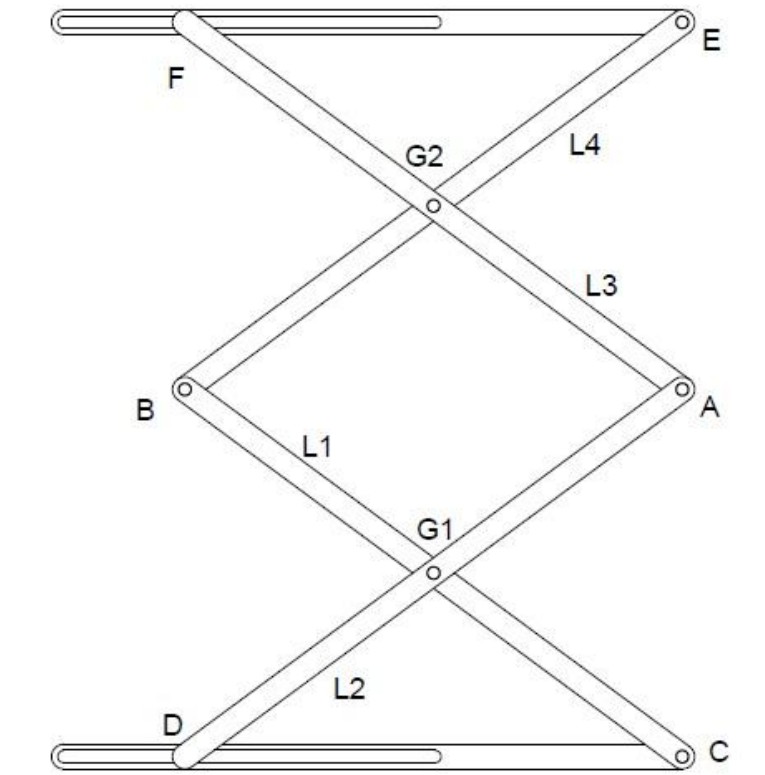


Figure 3.1 Basic Construction of a 2 stage Scissor Lift Mechanism

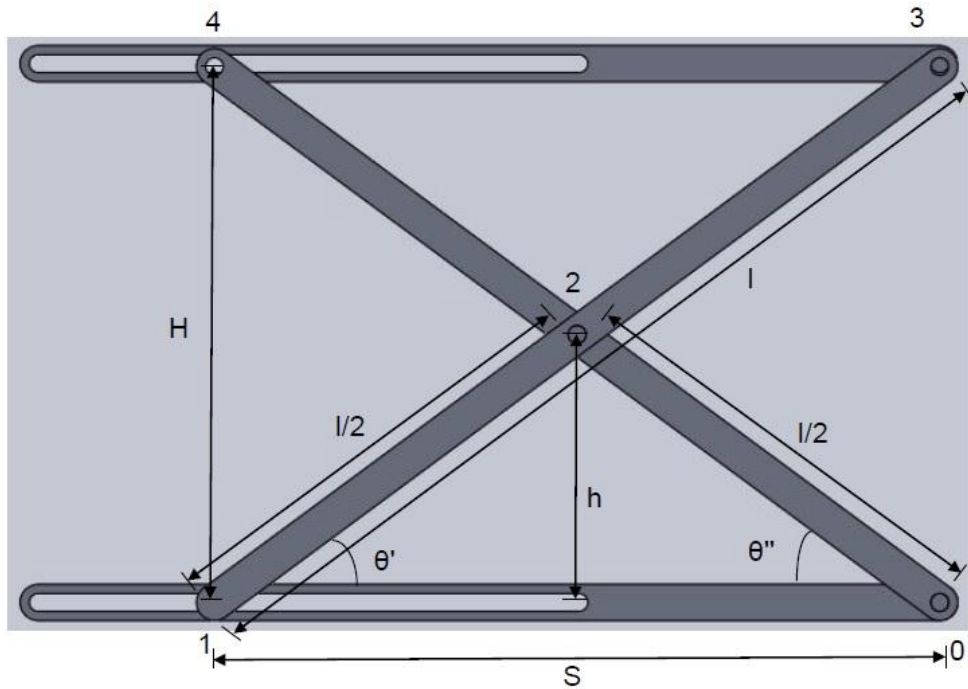


Figure 3.2 Kinematic Analysis Figure

3.2 Kinematic Analysis of the Mechanism

Kinematic analysis can be done by looking at the loops. For the design in Figure 3.2, link length (l) is equal for each of the link. Input distance is S and the midpoint height is h .

Total height for one stage is, $H = H_1 = 2h$.

The height h with respect to the input angle θ' is:

$$h = \left(\frac{l}{2}\right)\sin(\theta') \quad (3.1)$$

The inverse kinematics problem is expressed as:

$$\theta' = \arcsin\left(\frac{2h}{l}\right) \quad (3.2)$$

Height h can be expressed in terms of input link length (S):

$$h = \sqrt{\frac{l^2}{4} - \frac{S^2}{4}} \quad (3.3)$$

From Eq. (3.3) we can write inverse kinematics in terms of input link length:

$$S = \sqrt{l^2 - 4h^2} \quad (3.4)$$

Derivative of Eq. (3.4) gives the velocity of the platform for one stage:

$$\frac{dH_1}{dt} = \left(\frac{1}{\sqrt{\frac{l^2}{4} - \frac{S^2}{4}}} \right) \left(\frac{l}{2} \frac{dl}{dt} - \frac{S}{2} \frac{dS}{dt} \right) \quad (3.5)$$

Further derivation of Eq. (3.5) gives the acceleration of the end effector (platform):

$$\begin{aligned} \frac{d^2H_1}{dt^2} = & \left(-\frac{1}{2} \right) \left(\frac{1}{\left(\frac{l^2}{4} - \frac{S^2}{4} \right)^{\frac{3}{2}}} \right) \left(\frac{l}{2} \frac{dl}{dt} - \frac{S}{2} \frac{dS}{dt} \right)^2 + \left(\frac{1}{2} \right) \left(\frac{1}{\sqrt{\frac{l^2}{4} - \frac{S^2}{4}}} \right) \left[\left(\frac{dl}{dt} \right)^2 + l \frac{d^2l}{dt^2} - \right. \\ & \left. \left(\frac{dS}{dt} \right)^2 - S \frac{d^2S}{dt^2} \right] \end{aligned} \quad (3.6)$$

For two stage scissor lift total height is, $H = H_2 = 4h$.

$$H_2 = 2l \sin(\theta') \quad (3.7)$$

Inverse kinematics in terms of the input angle θ' is:

$$\theta' = \arcsin\left(\frac{H_2}{2l}\right) \quad (3.8)$$

Inverse kinematics in terms of the input link length:

$$S = \sqrt{l^2 - \frac{H_2^2}{4}} \quad (3.9)$$

For n stages, height of the platform will be:

$$H_n = 2nh = n\sqrt{l^2 - S^2} \quad (3.10)$$

Derivative of the Eq. (3.10) gives the velocity of the end effector for n stages:

$$\frac{dH_n}{dt} = n\left(\frac{1}{\sqrt{l^2 - S^2}}\right)\left(l \frac{dl}{dt} - S \frac{dS}{dt}\right) \quad (3.11)$$

Further derivative of the Eq. (3.11) gives the acceleration for n stages:

$$\begin{aligned} \frac{d^2H_n}{dt^2} = n\left[-\frac{1}{(l^2 - S^2)^{\frac{3}{2}}} \right] \left(l \frac{dl}{dt} - S \frac{dS}{dt} \right)^2 + \left(\frac{1}{\sqrt{l^2 - S^2}} \right) \left[\left(\frac{dl}{dt} \right)^2 + l \frac{d^2l}{dt^2} \right. \\ \left. - \left(\frac{dS}{dt} \right)^2 - S \frac{d^2S}{dt^2} \right] \end{aligned} \quad (3.12)$$

3.3 Dynamic Analysis of the Mechanism

To investigate the dynamics of the scissor lift mechanism, a lumped parameter model was developed based on the dynamic characteristics resulted from the simulation [47]. It was an approach based on the practical work and no dynamic model was presented on the whole system. This chapter presents a dynamic model of the complete system, which is attractive and fast compared to the time and effort intensive previous work. To model the mechanism through bond graph, 20-sim software is used.

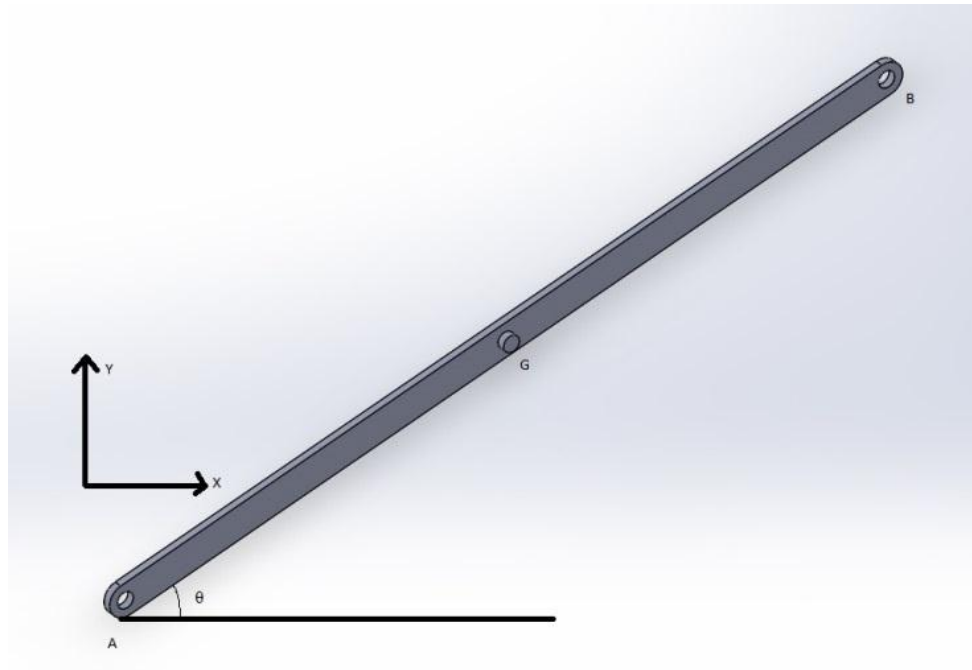


Figure 3.3 Schematic of a Single Link

3.3.1 Bond Graph Model of Each Link

For the bond graph modeling, a single beam is considered with mass and rotational inertia. External forces are applied at port A and B. Formulation becomes much easier, when all bodies in a multibody system contains three inertial coordinate (x,y,θ) . Velocity of the point B with respect to the point G can be formulated as:

$$\mathbf{V}_B = \mathbf{V}_G + (\mathbf{V}_{B/G}) \quad (3.13)$$

Where, the point G is the center of the gravity of the link. If the distance from the point G to the point B is r , then the equation will be:

$$\mathbf{V}_B = \mathbf{V}_G + \frac{d}{dt} (\mathbf{r}_{B/G}) \quad (3.14)$$

$$\mathbf{r}_{B/G} = BG \cos \theta \mathbf{i} + BG \sin \theta \mathbf{j} \quad (3.15)$$

$$\frac{d}{dt}(\mathbf{r}_{B/G}) = -BG\dot{\theta} \sin \theta \mathbf{i} + BG\dot{\theta} \cos \theta \mathbf{j} \quad (3.16)$$

From the above equation, we can get the velocity towards x direction and velocity towards y direction of the point B.

$$V_{Bx} = \dot{Gx} - BG\dot{\theta} \sin \theta \quad (3.17)$$

$$V_{By} = \dot{Gy} + BG\dot{\theta} \cos \theta \quad (3.18)$$

For point A velocity with respect to the point G is :

$$\mathbf{V}_A = \mathbf{V}_G + (\mathbf{V}_{A/G}) \quad (3.19)$$

The x and y velocity components of the point A can be written as follows:

$$V_{Ax} = \dot{Gx} + AG\dot{\theta} \sin \theta \quad (3.20)$$

$$V_{Ay} = \dot{Gy} - AG\dot{\theta} \cos \theta \quad (3.21)$$

To make A or B fixed, we need to apply zero flow source or approximately zero on parasitic spring in the bond graph. MTF is used in the bond graph to get the velocity constraints. Figure 3.4 shows the bond graph model of a single beam where length, mass and inertia parameters are considered as global parameter.

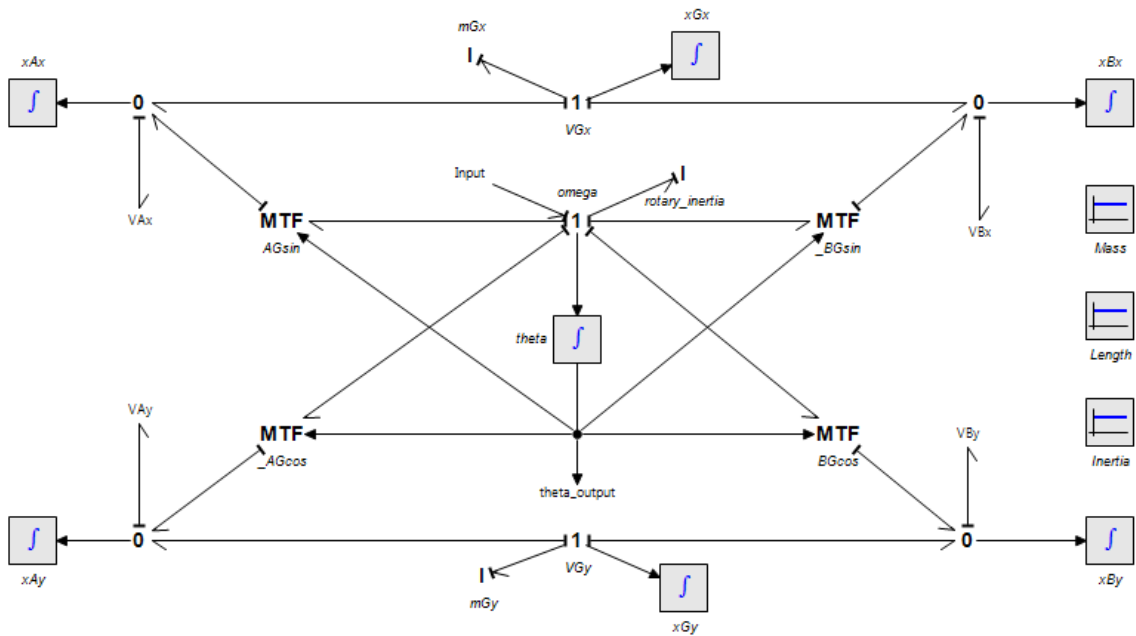


Figure 3.4 Bond graph of a single link

3.3.2 Parasitic Stiffness and Damping

In this work, to model each mechanical joint parasitic stiffness and damping are considered. Stiffness and damping are important criteria for many mechanical system designs. Stiff coupling springs are useful to use at mechanical joints to eliminate derivative causality of the system. Introduction of parasitic stiffness and/or resistive elements also remove dependencies among energy storage elements [48]. Figure 3.5 shows the parasitic stiffness and damping structure used in the bond graph design.

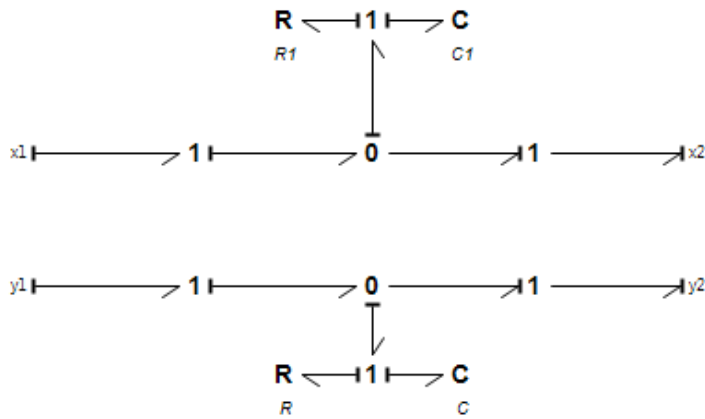


Figure 3.5 Parastic Stiffness and Damping

3.3.3 Motor Modeling

In a dc motor, supplied voltage goes to the armature through series connected inductor and resistance. Then armature converts the supplied emf to mechanical output. To model the DC motor in bond graph Inertia, Resistance and Gyrator elements are used to represent the aforementioned criteria. Motor shaft is modeled by the inductive and resistive element. To represent the gear ratio, transformer is used. Gear shaft inertia is represented by inductive element. Figure 3.7 shows the bond graph model of a DC motor.

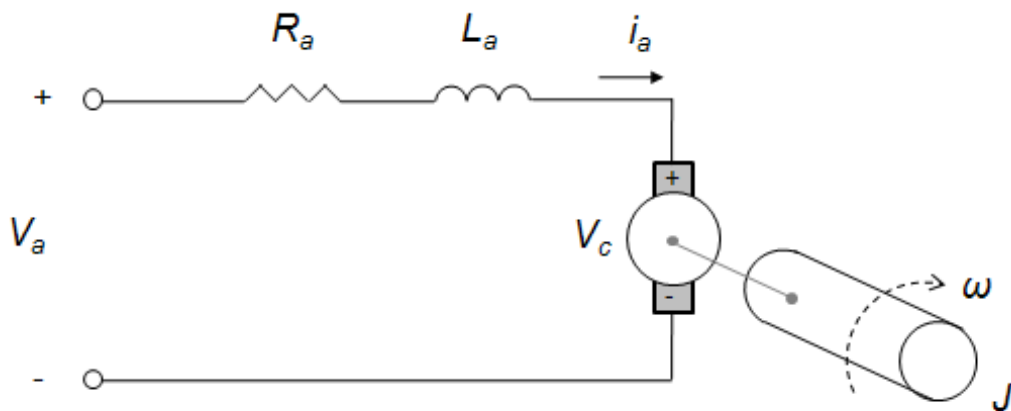
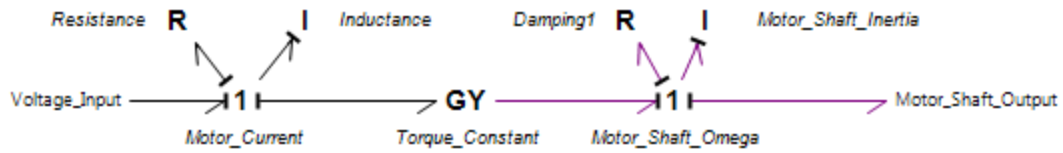
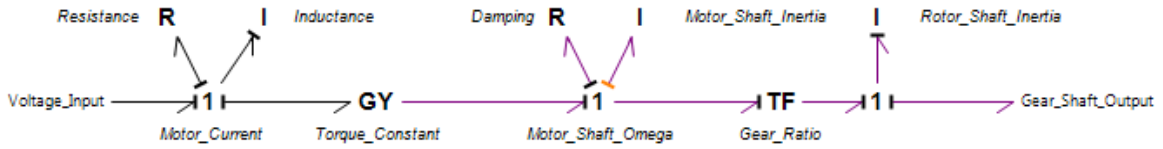


Figure 3.6 DC motor circuit diagram



(a)



(b)

Figure 3.7 DC Motor Schematics (a) Bond Graph of DC motor with motor shaft (b) DC motor with gear ratio representation

3.3.4 Control Mechanism

For controlling the mechanism, PID controller has been used. The PID will compare between the angle of present platform position and desired platform position. Based on the discrepancies between the two angles, it will control the motor output. To calculate the required angle for desired position, inverse kinematic equation has been used (Eq. (3.8)). Present position angle will be the angle of the fixed base link. Figure 3.8 shows the schematic of the whole control mechanism. PID stands for proportional, integral and derivative respectively. There are constant for each one of them inside the PID controller so that we can vary them to get our desired output. There are several ways to tune the PID controller parameters. We have used the trial and error tuning method. This is mainly

based on guess-and-check. In this method, the proportional action is the main control, while the integral and derivative action refines it. There is a limit block in the control mechanism. It will limit the output within a specified range of values so that, no unrealistic value can go to motor input. After the limit block there is a modulated effort source. There are two types of effort source available in bond graph. One is fixed and another one is variable. Here we are using the variable effort source for different input of the motor suggested by the PID controller. After the motor, the transformer is converting the rotary motion into linear motion.

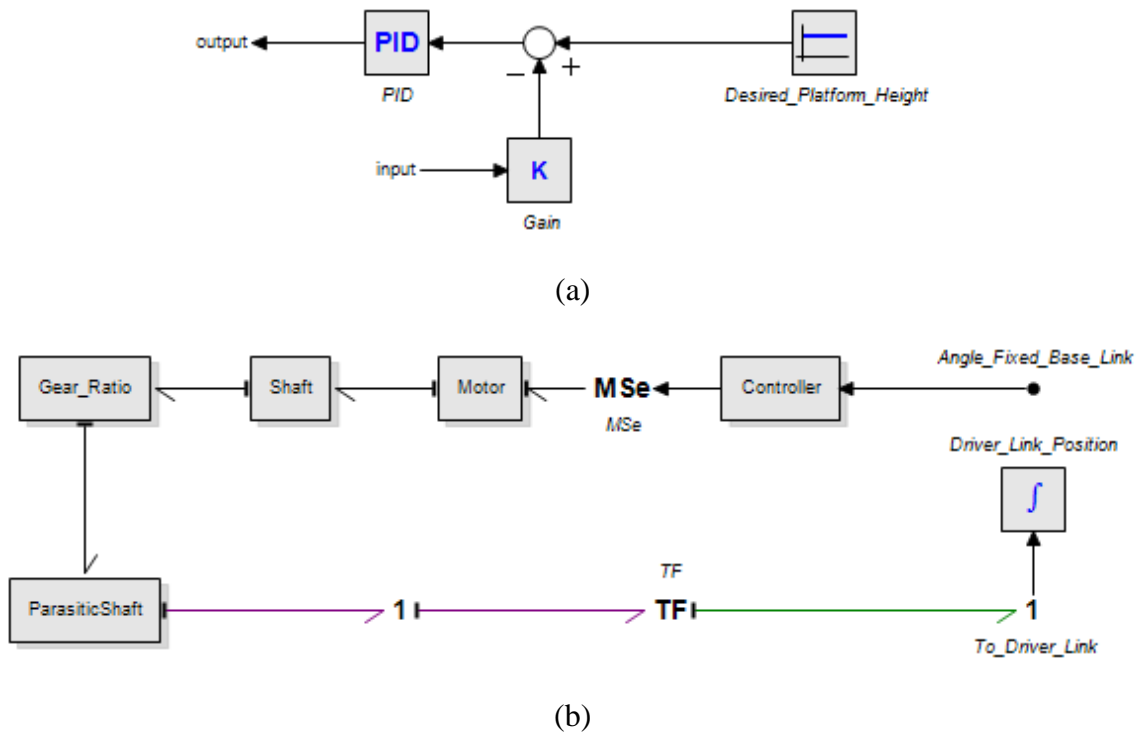


Figure 3.8 Control Schematic (a) controller block (b) control structure of scissor lift

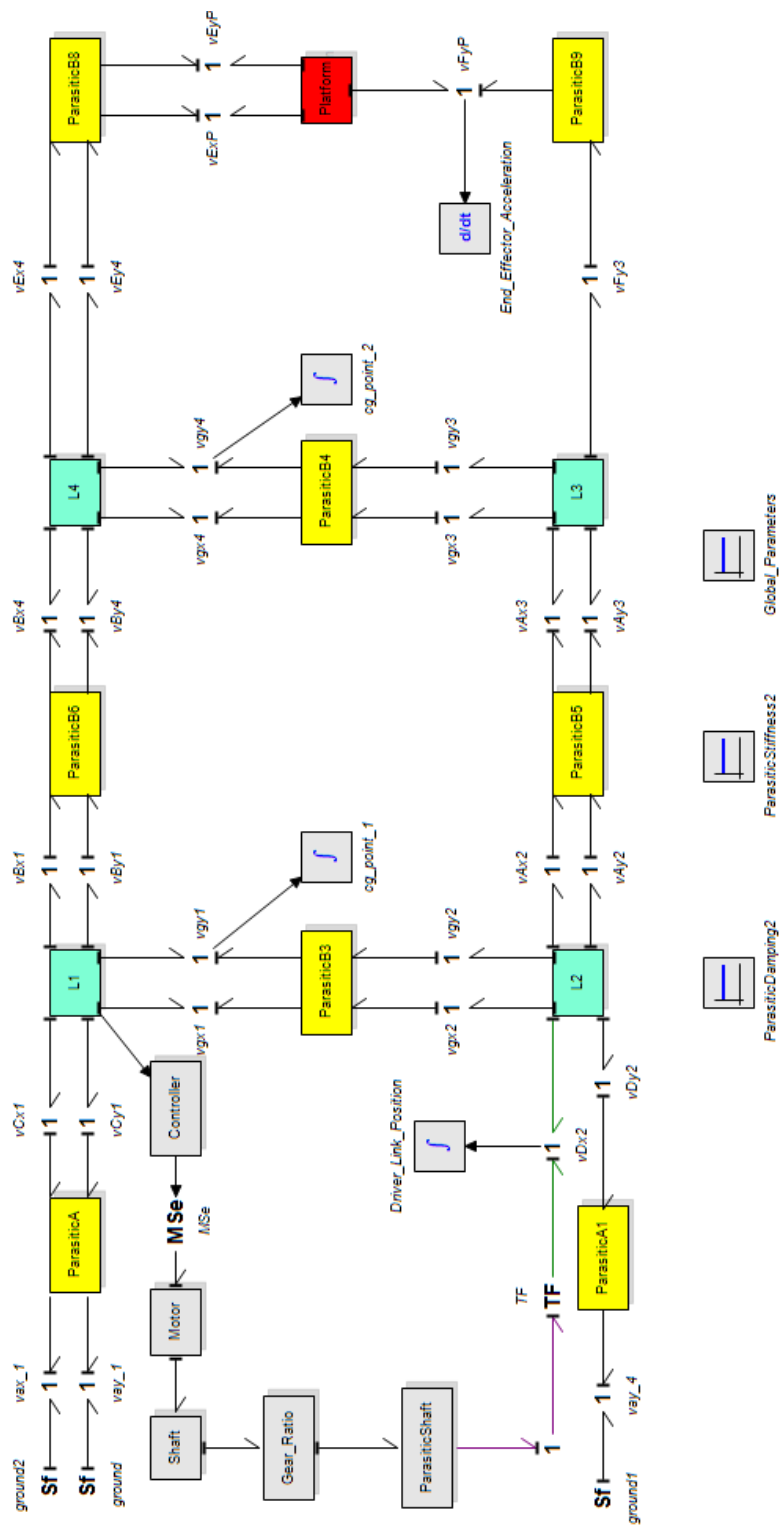


Figure 3.9 Bond graph model of Scissor-lift mechanism with two rhombus stages

3.3.5 Simulation

For the simulation, considered length for each of the link is set to 2 m. Width is 0.05 m and thickness is also 0.05m. To calculate mass properties, Carbon Fiber (Zoltek Panex 33) material has been used. Maxon motor (Model # 167131) is chosen as a DC motor with maxon gearhead (model # 110408). Material properties and motor specifications are mentioned in Appendix A.

Table 3.1 Simulation Result

Simulation Direction	PID Controller Parameter	Simulation Data
Forward Simulation Initial Height = 2 m Desired Height = 2.5 m	Proportional gain $k_p = -32.0 \{ \};$ Derivative time constant $\tau_D = 7.0 \{ s \};$ Tameness constant $\beta = 0.05 \{ \};$ Integral time constant $\tau_I = 40.0 \{ s \};$	Driver Link position = 1.56 m Max Velocity = 0.27 m/s Max Acceleration = 0.7 m/s^2 Peak Torque Duration = 0.4 s
Backward Simulation Initial Height = 2 m Desired Height = 1.5 m	Proportional gain $k_p = -32.0 \{ \};$ Derivative time constant $\tau_D = 11.0 \{ s \};$ Tameness constant $\beta = 0.05 \{ \};$ Integral time constant $\tau_I = 40.0 \{ s \};$	Driver Link position = 1.85 m Max Velocity = 0.25 m/s Max Acceleration = 0.7 m/s^2 Peak Torque Duration = 0.7 s

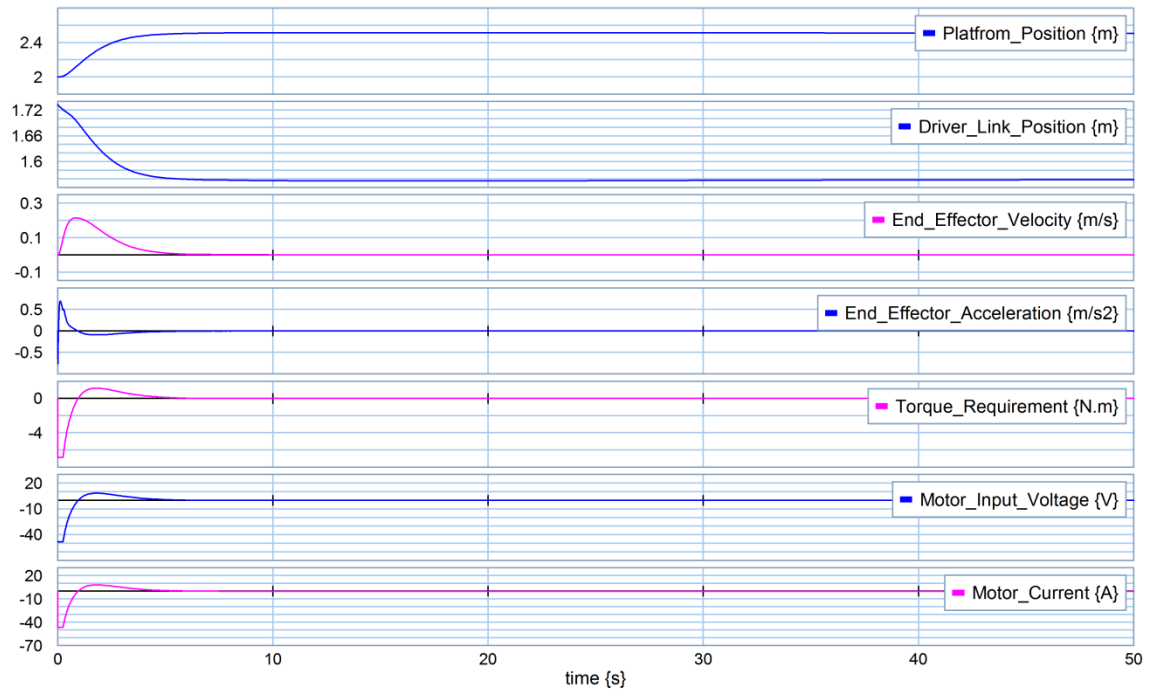


Figure 3.10 Simulation for Upward Movement (Desired Height = 2.5m, Initial Height = 2m)

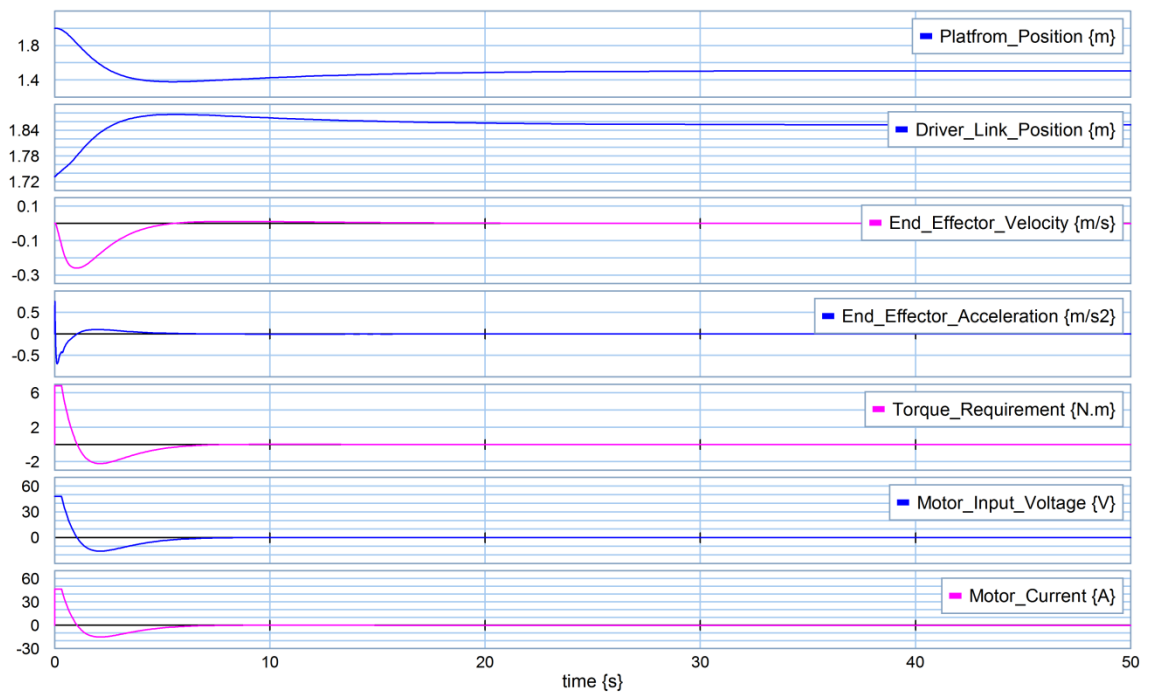


Figure 3.11 Simulation for Downward Movement (Desired Height = 1.5m, Initial Height = 2.0m)

3.3.6 Result Interpretation

In Figure 3.10, the platform moved towards a height of 2.5m higher than its initial height of 2 m. Driver link on the base should move in the backward direction from its initial position. From the inverse kinematics calculation, required position was 1.56 meter. Simulation shows exactly the same position of the driver link. Figure 3.11 shows simulation curves for the downward movement. Simulation results follow the calculation closely, which signifies the effectiveness of the dynamic modeling. It is more like the steady state of the dynamics under control is actually reaching the value calculated by the inverse kinematics.

3.4 Parametric Design optimization using Design of Experiment (DOE)

The objective of the DOE optimization is to find out the ideal parametric combination of a scissor lift mechanism for a certain height. Using dynamic and kinematic analysis of the scissor lift elevator, performance of the mechanism is simulated for different parametric combination to achieve certain height by the end effector or the platform. *Liu et al.* in [49] proposed a simulative calculation based optimal design approach of scissor lift, where the actuation principle is based on a hydraulic system. Usually, the performances of the scissor lift elevators are tested in the laboratory associated with important cost and time. That is why, effective statistical analysis is a great addition for this type of mechanism. From the analysis, link length was screened out as the most important factor for the height performance, compared to the stage repetition and motor torque. Brief description of the DOE is presented in Appendix B.

3.4.1 Experimental Factors and Response

Various parameters influencing the performance of a scissor lift are identified based on their kinetic and dynamic analysis. We considered five parameters as input factors and the output response is the height of the platform.

- **Mass of Link (A):** Each of the links has an effect on mechanism performance. For experiment, link mass is allowed to have two different levels (Two different material properties have been used). We considered, link mass – 1.36 Kg (low level) and link mass– 2.27 Kg (high level) for analysis.
- **Link Length (B):** If the length of the link increases, then it will increase the height coverage of the scissor lift. But, on the other hand mass will also increase. The DC motor needs to supply more torque. Considered two different link lengths are 0.4 m (low level) and 0.6 m (high level).
- **Platform Load (C):** There is a platform on the top of the scissor lift elevator to carry load. Platform load combines the mass of the platform as well as the carrying load. Here in this design the chosen platform loads are 5 Kg (low level) and 8 Kg (high level).
- **Motor Torque (D):** Based on the supplied motor torque, the end effector will move. When the mass of the system or load increases, then the motor needs to supply more torque. The considered two levels are 2.26 Nm (low level) and 3.4 Nm (high level). Motor torque is constant at low and high level.

- Repetition of Stages (E): Repetition of stages is done since, it reduces the transverse width thereby mechanism space utilization. Two links connected in their center of mass form a stage. Increase in the number of stages, will cause increase in the height performance of the mechanism. But increase of stages will also cause increase in weight and requires more torque to lift the same load up to certain height. Here, we considered 2 stage repetition as low level and 3 stage repetition as high level.

The response is the platform movement lifted by the scissor lift. For different level of the considered five factors, response (height) was recorded from the simulation. For five factors, a full factorial design needs a total of $2^5 = 32$ runs. Instead, we have used a half fractional factorial design with a total of $2^{5-1} = 16$ runs. One effect has to be confounded (Appendix B) and we choose $I = ABCDE$ as the confounding effect. As this is a resolution V design, all the main effects and two factor interactions can be estimated clearly. Three factor interactions are aliased with two factor interactions. But, they are not significant and can be ignored. Response data collected from 20 sim simulation.

3.4.2 Fractional Factorial Design of the Experiment

A 2^{5-1} fractional factorial (requiring 16 runs) design is used to determine the influence of the five factors and interactions of factors. Design Expert software (version 8.0.6) by Stat-Ease has been used to develop a design of Resolution V. An alias structure automatically chosen by the software takes the advantage of the sparsity of effects - that is, high order interactions are aliased with main and two factor interactions. Figure 3.12 shows the run order data. Figure 3.13 shows the effect list.

3.4.3 Analysis of Experimental Data

While analyzing data, most important factors and their significant interaction effects are considered. Figure 3.14 and Figure 3.15 shows the effect of A, B, C, D, E and the interaction BE are the main contributors as their percentage contributions are very high. Remaining factors have no significant contributions to the height performance, as their percentage contributions are less.

Select	Std	Run	Factor 1 A:Mass of Link Kg	Factor 2 B:Link Length m	Factor 3 C:Platform Load Kg	Factor 4 D:Motor Torque Nm	Factor 5 E:Repitition of Stages	Response 1 Platform Height m
1		1	-1	-1	-1	-1	1	1.05
	2	13	1	-1	-1	-1	-1	0.71
	3	7	-1	1	-1	-1	-1	1.1
	4	16	1	1	-1	-1	1	1.55
	5	3	-1	-1	1	-1	-1	0.65
	6	15	1	-1	1	-1	1	0.98
	7	12	-1	1	1	-1	1	1.65
	8	2	1	1	1	-1	-1	1
	9	8	-1	-1	-1	1	-1	0.75
	10	9	1	-1	-1	1	1	1.13
	11	10	-1	1	-1	1	1	1.74
	12	14	1	1	-1	1	-1	1.11
	13	11	-1	-1	1	1	1	1.08
	14	6	1	-1	1	1	-1	0.66
	15	5	-1	1	1	1	-1	1.13
	16	4	1	1	1	1	1	1.63

Figure 3.12 Aliased terms including run list and Data for Experiment

Term	Stdized Effect	Sum of Squares	% Contribution
Intercept			
A-Mass of Link	-0.048	9.025E-003	0.48
B-Link Length	0.49	0.95	50.32
C-Platform Load	-0.045	8.100E-003	0.43
D-Motor Torque	0.067	0.018	0.96
E-Repitition of Stages	0.46	0.86	45.30
AB	-0.035	4.900E-003	0.26
AC	-0.012	6.250E-004	0.033
AD	5.000E-003	1.000E-004	5.294E-003
AE	-1.000E-002	4.000E-004	0.021
BC	0.022	2.025E-003	0.11
BD	1.000E-002	4.000E-004	0.021
BE	0.095	0.036	1.91
CD	-0.012	6.250E-004	0.033
CE	0.013	6.250E-004	0.033
DE	0.020	1.600E-003	0.085

Figure 3.13 Effect List

3.4.4 Pareto Chart and Half Normal Plot

From the pareto chart and half normal plot (Appendix B), we can screen out the most significant factors and their interaction effects.

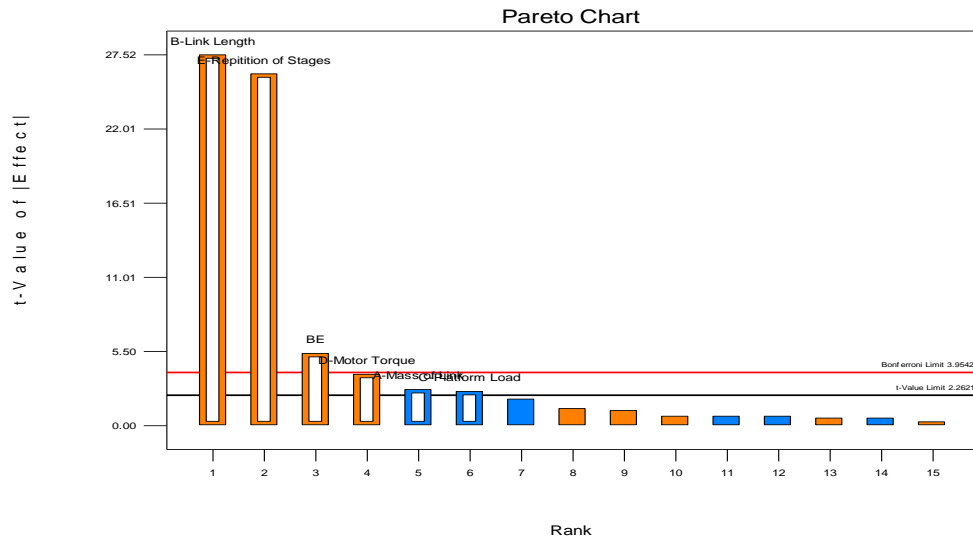


Figure 3.14 Pareto Chart

Design-Expert® Software
Platform Height

Shapiro-Wilk test
W-value = 0.930
p-value = 0.477
A: Mass of Link
B: Link Length
C: Platform Load
D: Motor Torque
E: Repitition of Stages
■ Positive Effects
■ Negative Effects

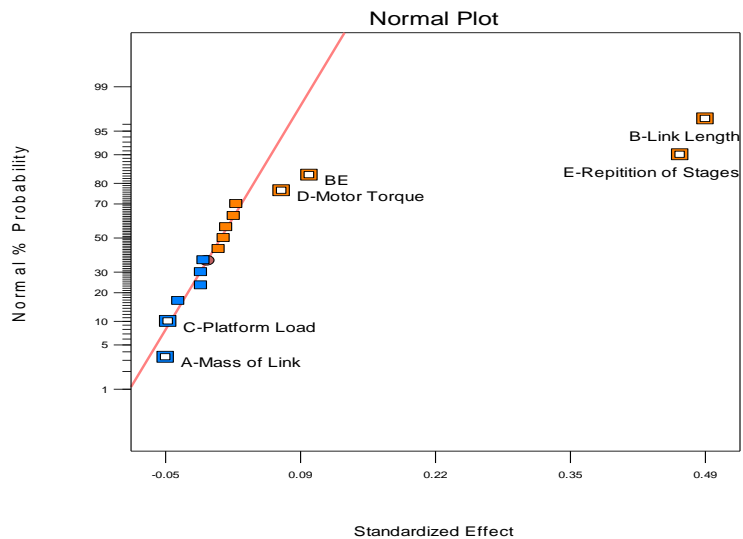


Figure 3.15 Half Normal Plot

Figure 3.14 shows that from our considered parameters, all the single factor effects are significant. Interactions between BE is the most dominant interaction effect. Figure 3.15 shows the half normal plot and it justifies the same result for the effects. The most significant factors will be away from the line in the half normal plot.

3.4.5 ANOVA Analysis and Regression Model

The ANOVA table summarizes the significance. From the F-value and probability value comparison of the effects, the software computes the significance. In summary, the standard shows the deviation of the error term. R^2 presents the percentage of total variability explained by the model. Addition of effect will increase the R value. That is why we should look at the adjusted R value produced by the model. The difference between the two R^2 should be very small. Precision should be greater than 4 for an adequate model. Figure 3.16 shows the ANOVA table and the ANOVA summary for the proposed model. The R^2 values are very close and precision is much greater than 4 which signify the adequacy of the model. Figure 3.17 represents a mathematical model for the output response of the scissor lift.

3.4.6 Residual Analysis

Residual analysis checks whether the assumptions of the ANOVA are correct or not. We made following assumptions:

1. Random Samples from their respective population.
2. All samples are independent.
3. Departures from group mean are normally distributed for all data groups.
4. All data groups have equal variance.

Response	1	Platform Height				
Hierarchical terms added after manual regression						
E						
ANOVA for selected factorial model						
Analysis of variance table [Partial sum of squares - Type III]						
Source	Sum of Squares	df	Mean Square	F Value	p-value Prob > F	
Model	1.88	6	0.31	249.25	< 0.0001	significant
<i>A-Mass of Link</i>	9.025E-003	1	9.025E-003	7.19	0.0252	
<i>B-Link Length</i>	0.95	1	0.95	757.13	< 0.0001	
<i>C-Platform Load</i>	8.100E-003	1	8.100E-003	6.45	0.0317	
<i>D-Motor Torque</i>	0.018	1	0.018	14.52	0.0042	
<i>E-Repitition of Stages</i>	0.86	1	0.86	681.47	< 0.0001	
<i>BE</i>	0.036	1	0.036	28.75	0.0005	
Residual	0.011	9	1.256E-003			
Cor Total	1.89	15				

Std. Dev.	0.035	R-Squared	0.9940
Mean	1.12	Adj R-Squared	0.9900
C.V. %	3.16	Pred R-Square	0.9811
PRESS	0.036	Adeq Precisiorn	45.440

The "Pred R-Squared" of 0.9811 is in reasonable agreement with the "Adj R-Squared" of 0.9900; i.e. the difference is less than 0.2.

"Adeq Precision" measures the signal to noise ratio. A ratio greater than 4 is desirable. Your ratio of 45.440 indicates an adequate signal. This model can be used to navigate the design space.

Figure 3.16 ANOVA table with the summary

Final Equation in Terms of Coded Factors:	Final Equation in Terms of Actual Factors:
Platform Height =	Platform Height =
+1.12	+1.12000
-0.024 * A	-0.023750 * Mass of Link
+0.24 * B	+0.24375 * Link Length
-0.023 * C	-0.022500 * Platform Load
+0.034 * D	+0.033750 * Motor Torque
+0.23 * E	+0.23125 * Repitition of Stages
+0.047 * BE	+0.047500 * Link Length * Repitition of Stages

Figure 3.17 Regression Model

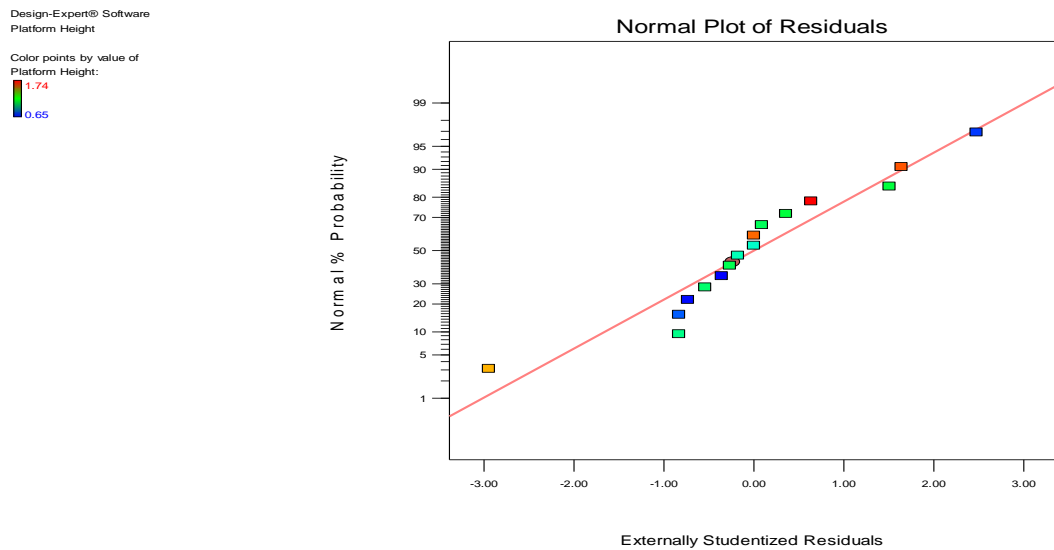


Figure 3.18 Normal Plot

From the normal probability plot (Figure 3.18), one can observe that maximum points follow a straight line. So, the distributions of residuals are almost normal. The plot of Residuals vs. Predicted (Figure 3.19) looks like well scattered, which indicates constant variance. Figure 3.20 shows the Residuals vs Run plot. From the plot we can see, most of the data are random (i.e. no trend and points are beyond the red line). Finally, from the Box-Cox plot of Figure 3.21 we can see that the current line (blue line) is between the

ranges (between Low & High Confidence Interval). This result means no transformation.

So, we can conclude that the assumptions of ANOVA are satisfied.

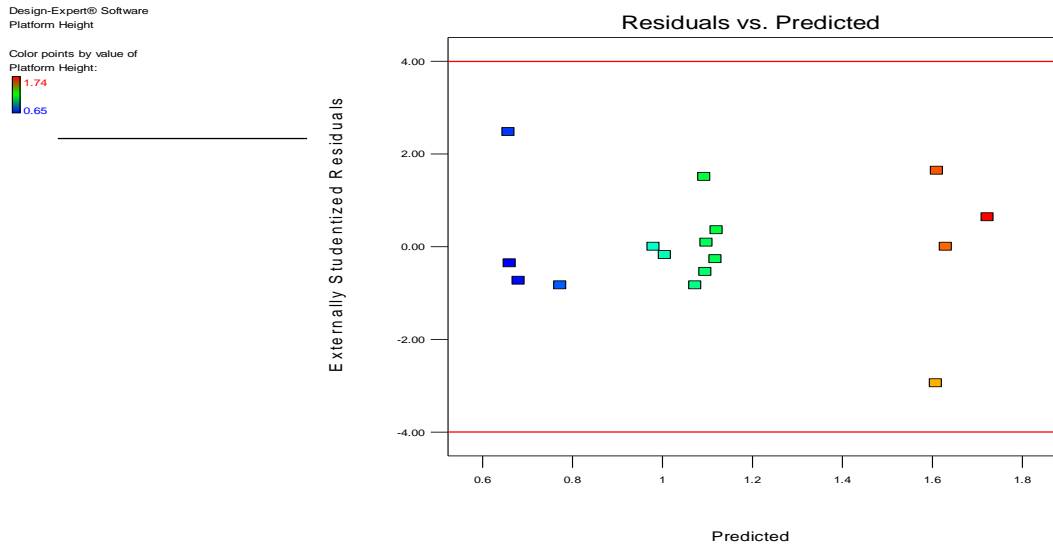


Figure 3.19 Residuals vs. Predicted Plot

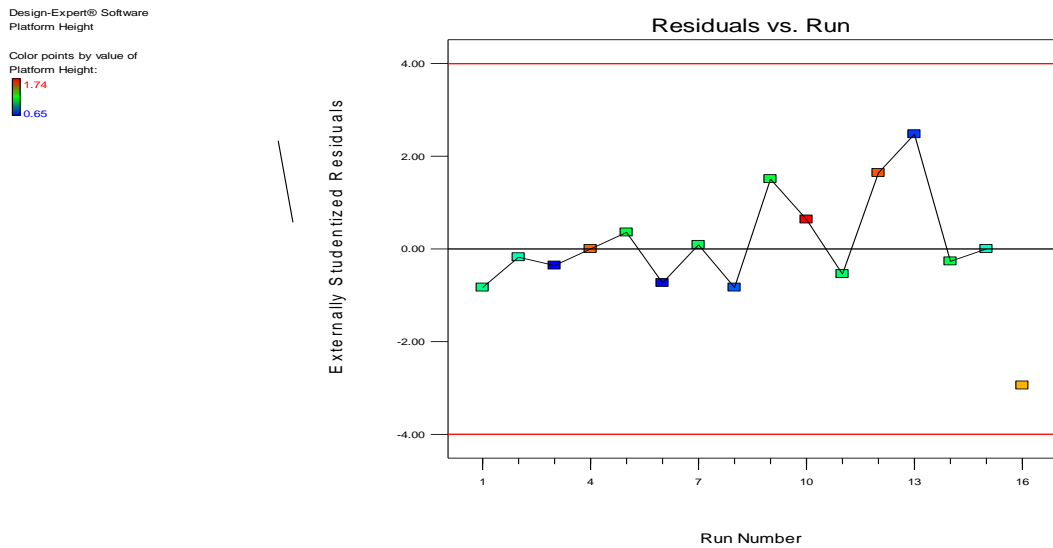


Figure 3.20 Residuals vs. Run Plot

Design-Expert® Software
Platform Height

Lambda
Current = 1
Best = 0.43
Low C.I. = -0.61
High C.I. = 1.45

Recommend transform:
None
(Lambda = 1)

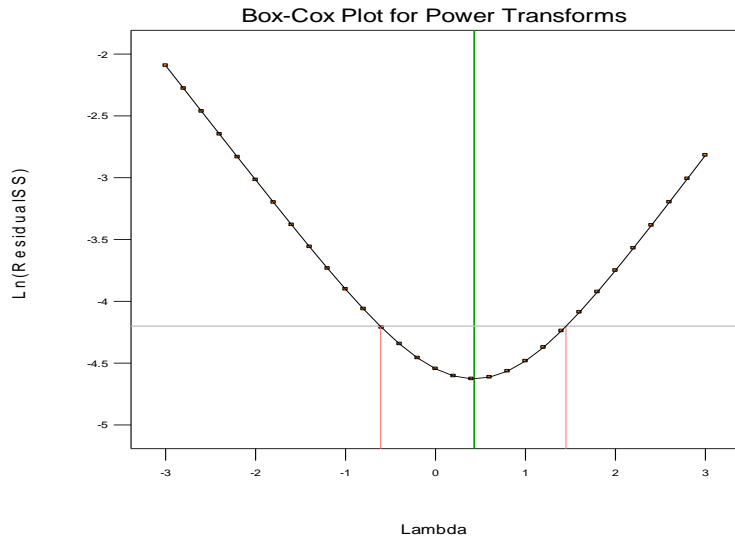


Figure 3.21 Box-cox Plot for power transformation

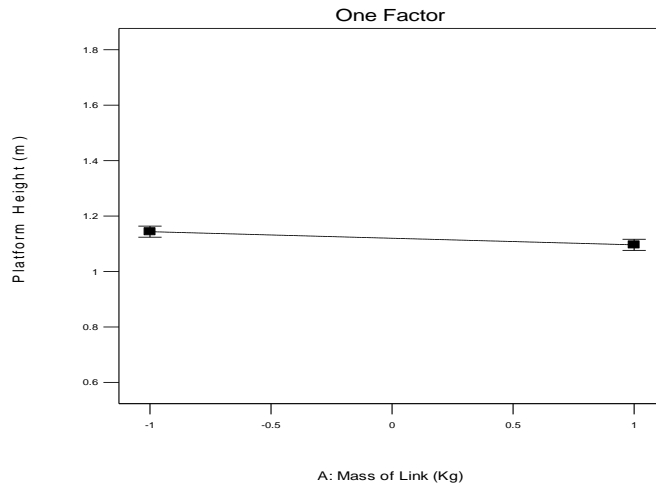
3.4.7 Interactions

From the interactions graph, we can determine the effect of the parameters on the response. Figure 3.22 shows the single factor effect on the height performance for main factors. We can see that factor A and C has negative effect on performance. As we move from low to high level, performance is decreasing. On the other hand, B, D and E have positive effect on performance. Parameter E has most significant effect. Figure 3.23 shows the two factor interaction curve of B and E. It indicates that the height performance will increase with the increase of B from low level to high level for both level of E. At high level (towards 1) improvement is more rapid compared to the low level (towards -1). This signifies that link length increment is the most dominant one to increase the performance of scissor lift. It is more significant compared to the networking. Figure 3.24 shows the outcome of the model optimization run.

Design-Expert® Software
Factor Coding: Actual
Platform Height (m)

X1 = A: Mass of Link

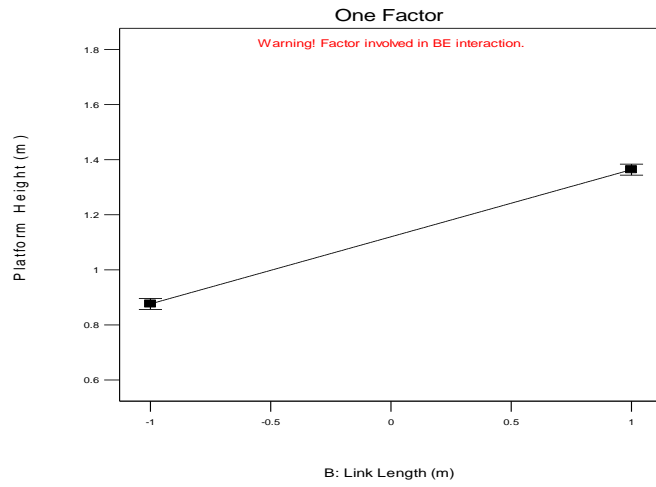
Actual Factors
B: Link Length = 0
C: Platform Load = 0
D: Motor Torque = 0
E: Repetition of Stages = 0



Design-Expert® Software
Factor Coding: Actual
Platform Height (m)

X1 = B: Link Length

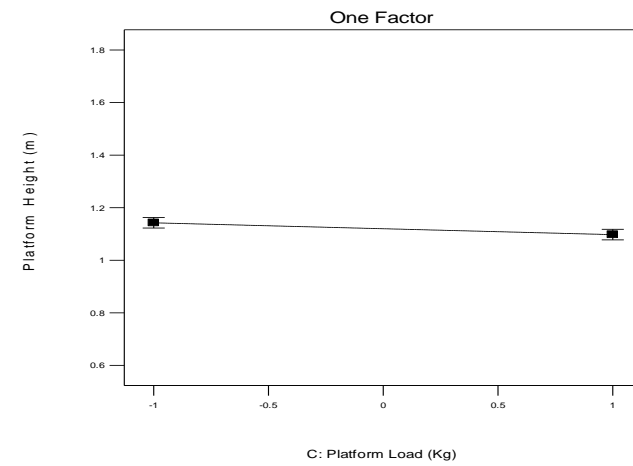
Actual Factors
A: Mass of Link = 0
C: Platform Load = 0
D: Motor Torque = 0
E: Repetition of Stages = 0



Design-Expert® Software
Factor Coding: Actual
Platform Height (m)

X1 = C: Platform Load

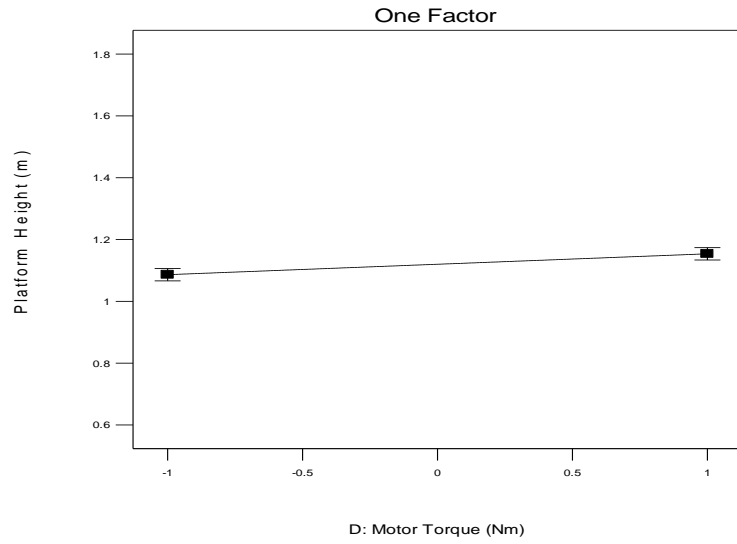
Actual Factors
A: Mass of Link = 0
B: Link Length = 0
D: Motor Torque = 0
E: Repetition of Stages = 0



Design-Expert® Software
Factor Coding: Actual
Platform Height (m)

X1 = D: Motor Torque

Actual Factors
A: Mass of Link = 0
B: Link Length = 0
C: Platform Load = 0
E: Repitition of Stages = 0



Design-Expert® Software
Factor Coding: Actual
Platform Height (m)

X1 = E: Repitition of Stages

Actual Factors
A: Mass of Link = 0
B: Link Length = 0
C: Platform Load = 0
D: Motor Torque = 0

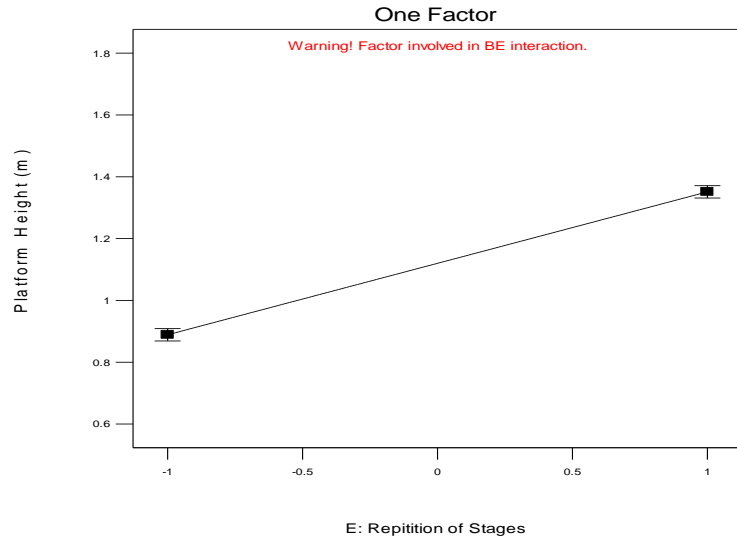


Figure 3.22 Single Factor Interaction Graph

Design-Expert® Software
 Factor Coding: Actual
 Platform Height (m)

X1 = B: Link Length
 X2 = E: Repitition of Stages

Actual Factors
 A: Mass of Link = 0
 C: Platform Load = 0
 D: Motor Torque = 0

■ E- -1
 ▲ E+ 1

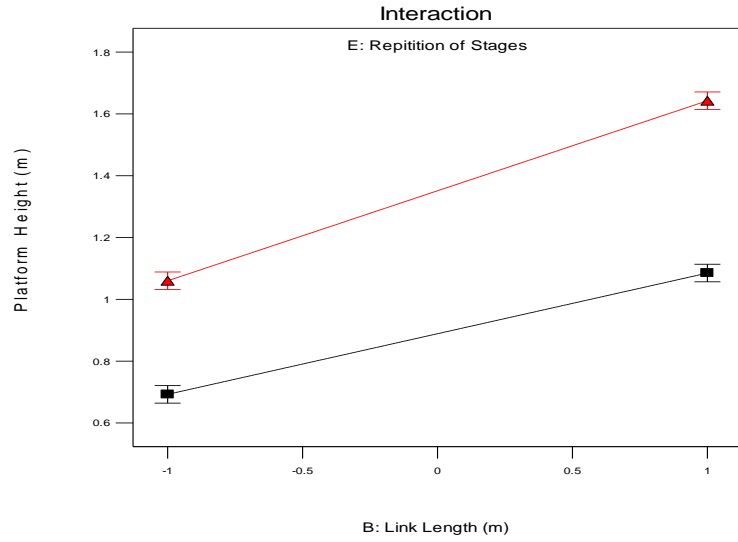


Figure 3.23 Two factors interaction

Constraints

Name	Goal	Lower Limit	Upper Limit	Lower Weight	Upper Weight	Importance
A:Mass of Link	is in range	-1	1	1	1	3
B:Link Length	is in range	-1	1	1	1	3
C:Platform Load	is target = 1	-1	1	1	1	3
D:Motor Torque	is in range	-1	1	1	1	3
E:Repitition of St	is in range	-1	1	1	1	3
Platform Height	is target = 1.65	0.65	1.74	1	1	3

Solutions

Number	Mass of Link	Link Length	Platform Load	Motor Torque	Repitition of Stages	Platform Height	Desirability	Selected
1	<u>-0.213</u>	<u>1.000</u>	<u>1.000</u>	<u>0.910</u>	<u>0.980</u>	<u>1.650</u>	<u>1.000</u>	Selected
2	-0.993	1.000	1.000	0.210	0.998	1.650	1.000	
3	-0.918	0.947	1.000	0.743	0.995	1.650	1.000	
4	-0.984	0.973	1.000	0.997	0.931	1.650	1.000	
5	-0.706	0.999	1.000	0.443	0.995	1.650	1.000	

Figure 3.24 Optimization Runs for validation

3.4.8 Model Optimization

The model was optimized and extra runs performed for validity check. Four factors were kept in range and the platform height was fixed at 1.65m to get the optimum runs with maximum platform load. First five combinations were verified in 20 sim. Figure 3.24 shows that for the certain height all factors are in their specified range and we can determine the values for each of the factor. Output confirms the validity of the model to find the parametric combination and their respected values for certain height coverage. Factor values are given in their coded form.

3.5 Discussions

Dynamic behavior of the scissor lift mechanism is modeled and verified through the application of desired output criteria. Design optimization of scissor lift type elevating platform using the DOE methodology has also been presented. From the simulation, we can conclude the DC motor based scissor elevator can also be used as linear actuator for parallel manipulator. But this actuator has the following backdrops:

- Presence of slider
- Friction
- Prismatic pair
- Low acceleration

These problems limit their use as a high performance linear actuator. But, this chapter can be used as a good reference for practical designing of scissor type actuator and it was a good learning experience for designing the high performance linear actuator.

Chapter 4

Kinematic Analysis of the Actuator

4.1 Introduction

This chapter presents the detailed kinematic analysis of the newly designed actuator along with the networking formulations. To build a linear actuator using a parallel topology, we can put them into a cross, or X, or scissors. Then we need to close them and there are two ways to achieve that: (1) by closing with a bar containing a slide (i.e the scissor lift mechanism), or (2) by closing with two bars, separated by a revolute joint (X-track with one DC motor at one revolute end). Figure 4.1 shows a single network rhombus configuration (X-Track with the DC motor) of the newly designed actuator. Hence, the newly designed actuator is different from the scissor lift platforms, since there are no sliders that produce dynamic problems forbidding high acceleration.

The four bar rhombus configuration is a special case of the four bar linkage, where all the link lengths are equal. All sides of a rhombus are congruent and they can have any angle. The identical nature of the structure gives the opportunity of networking them very easily to improve performance. Networking of these identical linkages helps to reduce the encumbrance. Brief kinematic analysis of the four bar actuator is described in [3].

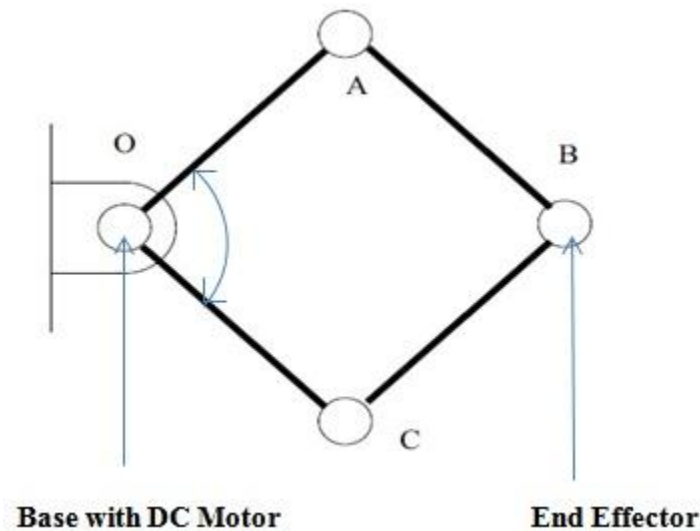


Figure 4.1 Four Bar Rhombus Configuration

4.2 Kinematic Formulation

From Figure 4.1, we can see $OA = AB = BC = OC$. For our analysis, we considered the link length as r . The mechanism configuration even includes the square, when angles are set to 90 degrees. The forward kinematics problem becomes:

$$x = 2r \cos\left(\frac{\theta}{2}\right) \quad (4.1)$$

Where,

x = Linear distance between the point O and B.

θ = Angle between the bar OA and OC

The Inverse kinematics problem is expressed as:

$$\theta = 2 \arccos\left(\frac{x}{2r}\right) \quad (4.2)$$

Derivation of Eq. (4.2) will give us the linear velocity. The forward differential kinematics is expressed by the following equation:

$$v = -r\omega \sin\left(\frac{\theta}{2}\right) \quad (4.3)$$

where,

$$\omega = \frac{d\theta}{dt}$$

We take the following geometric property:

$$\cos\left(\frac{\theta}{2}\right) = \frac{x}{2r} \quad (4.4)$$

Applying Pythagoras theorem:

$$\sin\left(\frac{\theta}{2}\right) = \left(\frac{1}{2}\right) \sqrt{4 - \left(\frac{x^2}{r^2}\right)} \quad (4.5)$$

After putting the values from Eq. (4.5) the linear velocity of the end effector becomes:

$$v = -\omega \left(\frac{r}{2}\right) \sqrt{4 - \left(\frac{x^2}{r^2}\right)} \quad (4.6)$$

From Eq. (4.6) we can calculate the angular velocity. Angular velocity can be rewritten as:

$$\omega = -\frac{v}{r \sin\left(\frac{\theta}{2}\right)} \quad (4.7)$$

After putting the value of $\sin\left(\frac{\theta}{2}\right)$ from the Eq. (4.5) the angular velocity will be:

$$\omega = -\left(\frac{v}{r}\right)\sqrt{1 - \left(\frac{x}{2r}\right)} \quad (4.8)$$

Further differentiation of the Eq. (4.3) will give the acceleration of the extremity:

$$a = -r\alpha \sin\left(\frac{\theta}{2}\right) - \frac{1}{2} r \omega^2 \cos\left(\frac{\theta}{2}\right) \quad (4.9)$$

After substituting values from Eq. (4.4) and (4.5) we can write:

$$a = -\frac{1}{2} r\alpha \sqrt{4 - \left(\frac{x^2}{r^2}\right)} - \frac{1}{4} \omega^2 x \quad (4.10)$$

From Eq. (4.9) the angular acceleration α is:

$$\alpha = -\frac{-a - \frac{1}{2} r \omega^2 \cos\left(\frac{\theta}{2}\right)}{r \sin\left(\frac{\theta}{2}\right)} \quad (4.11)$$

After substituting values of $\cos\left(\frac{\theta}{2}\right)$ and $\sin\left(\frac{\theta}{2}\right)$ we will get the final equation for angular acceleration:

$$\alpha = 2ar^{-1} \frac{1}{\sqrt{4 - \left(\frac{x^2}{r^2}\right)}} - \frac{1}{2} vx \sqrt{2} r^{-4} \left(\frac{x}{r}\right)^{-\frac{3}{2}} \quad (4.12)$$

4.3 Singularity Analysis

Singularity is a point at which a function takes an infinite value. It is either addition or loss of DOF; meaning a point where the torque becomes infinite and mechanism locks itself or a point where the mechanism is moving whatever the motor torque. In actuator design these points are very important as we need to identify those points to avoid them

during the movement of the actuator. Geometrically links have no material existence (no mass) and they can occupy the same position in space. In reality, the mass doesn't allow such cases. Here, we calculated singularity in terms of the input angle and the extremity positions. First, we can calculate the singularity in terms of the input angle θ :

$$\sin\left(\frac{\theta}{2}\right) = 0 \quad (4.13)$$

Hence, we find a singularity at $\theta = 0$ and its counterpart, $\theta = 360$ degrees. So, during construction of the actuator we have to be careful so that the configuration can't reach to those points. To avoid those point's, we have to introduce some physical constrain.

In terms of the extremity position (x):

$$\sqrt{4 - \left(\frac{x^2}{r^2}\right)} = 0 \quad (4.14)$$

By solving the above equation we can see the singular position exist at $x = 2r$ corresponds to the same in terms of the input angle as $\theta = 0$.

4.4 Range of Motion

The second important performance criterion is usually the range of motion of the end effector. For single DOF mechanism, range of motion reduces itself to a single DOF curve segment. In our case, it becomes a line segment. We always wish to maximize the range of motion as much as we can. Considering the Forward Kinematics equation, the maximum value is obtained when $\cos\left(\frac{\theta}{2}\right) = 1$ and the minimum value will be at $\cos\left(\frac{\theta}{2}\right) = -1$. Hence, from the Eq. (4.4) we can write, $x_{max} = 2r$ and the related angle is then $\theta = 0$. Moreover, $x_{min} = -2r$ and the related angle is then $\theta = -2\pi$.

Pure geometric nature of the kinematics allows mechanism to reverse by going unto itself. Hence, the minimum can be seen on the left or negative side of the reference frame and the maximum is on the right side or positive in the reference frame. But, the rhombus configuration will have a pair of opposite linkages below and above. This leads to a physical constraint equation. The opposite links are parallel and they will touch each other alongside at two mechanism rotation. From the singularity analysis we have already seen that at $\theta = 0$ or $\theta = 360$ we will reach singular points. So, we need to set an operating range for the input angle θ , to avoid the singularity points. Considering identical width of the bar as W , the minimal rotation angle increases to:

$$\theta_{min} > 0 \quad (4.15)$$

$$\theta_{min} = 2 \arcsin\left(\frac{W}{r}\right) \quad (4.16)$$

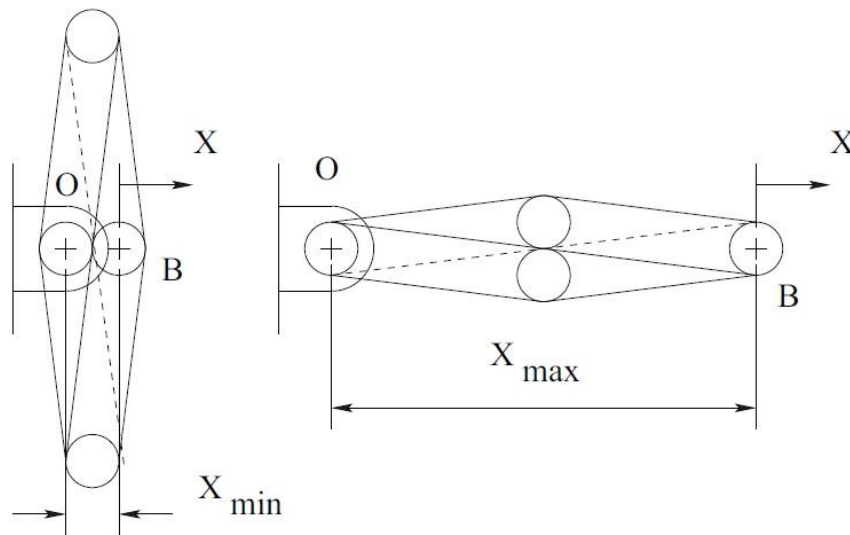


Figure 4.2 Rhombus Extreme Positions

For the upper range of the theta values, we have to calculate the θ_{max} :

$$\theta_{max} < \pi \quad (4.17)$$

$$\theta_{max} = 2 \arccos\left(\frac{W}{r}\right) \quad (4.18)$$

Extreme positions can be calculated from these values. Minimum length would be:

$$x_{min} = 2rcos\left(\frac{\theta_{max}}{2}\right) \quad (4.19)$$

Substituting θ_{max} we get:

$$x_{min} = 2rcos\left(2 \arccos\left(\frac{W}{r}\right)\right) \quad (4.20)$$

Similarly, maximum length will occur at minimum angular displacement:

$$x_{max} = 2rcos\left(\frac{\theta_{min}}{2}\right) \quad (4.21)$$

Substituting θ_{min} we get:

$$x_{max} = 2rcos\left(2 \arcsin\left(\frac{W}{r}\right)\right) \quad (4.22)$$

4.5 Encumbrance

Encumbrance is the distance from one side of the mechanism to the other side taking into account the linkage width. Encumbrance is an important issue considering that the mechanism spread sideways making them subjects to collisions, if other actuator would be in the vicinity. To use them with parallel manipulator this has even much more importance.

A rhombus would have minimum encumbrance of $E_{min} = 2W$ at angle θ_{min} . Maximum encumbrance occurring at the maximum input angle θ_{max} .

$$E_{max} = W + 2\sqrt{r^2 - W^2} \quad (4.23)$$

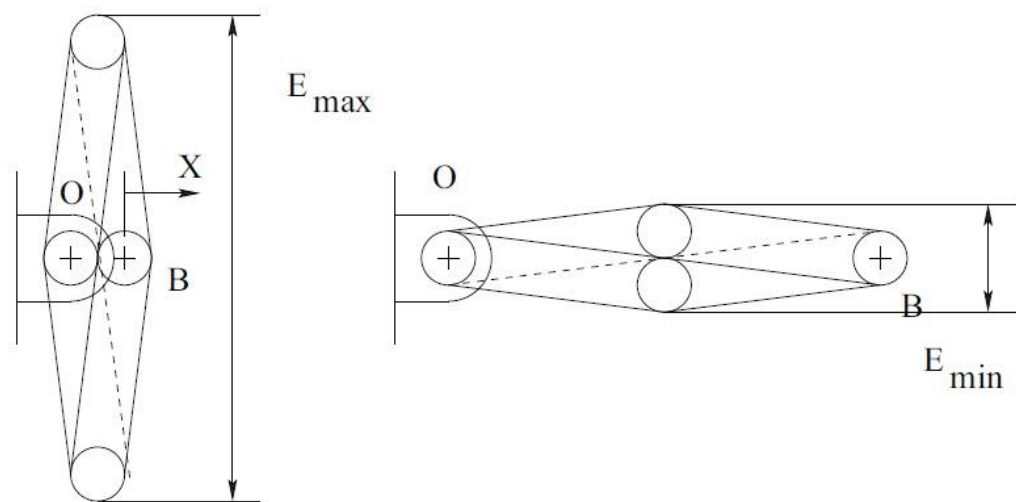


Figure 4.3 The Rhombus Encumbrance

4.6 Networking of Rhombus Configuration

The main advantage of the four bar rhombus configuration is that we can easily increase its range of motion (stroke length) by doing networking. As in the rhombus configuration all the four bars are identical, it becomes very easy to network the mechanism to achieve certain end effector position based on the calculation. Figure 4.4 shows the networking of double and triple rhombus.

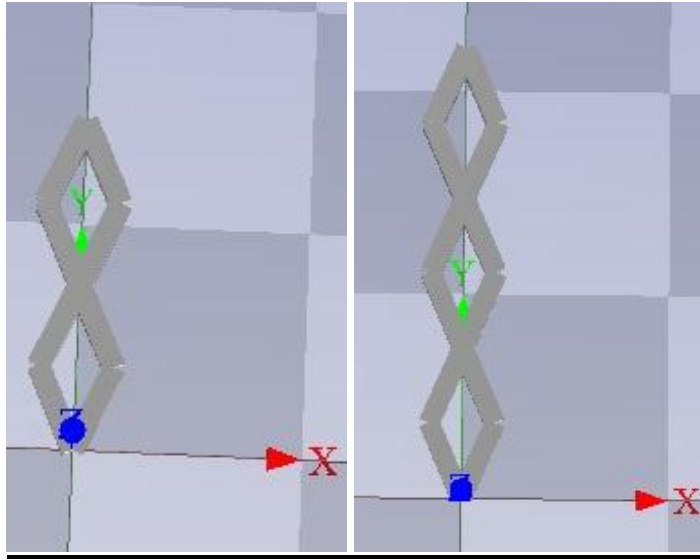


Figure 4.4 Double rhombus and triple rhombus configuration

For the double rhombus configuration distance traveled by the first moving central joint:

$$x_1 = 2r \cos\left(\frac{\theta}{2}\right) \quad (4.24)$$

This formula is similar to the forward kinematics of the four bar rhombus without any networking. Then distance traveled by the second moving joint or the end effector for the double rhombus:

$$x_2 = 2x_1 = 4r \cos\left(\frac{\theta}{2}\right) \quad (4.25)$$

Distance traveled by the third moving central joint of triple rhombus:

$$x_3 = 3x_1 = 6r \cos\left(\frac{\theta}{2}\right) \quad (4.26)$$

From the above calculation we can write a general formula for rhombus networking. For n number of networking the extremity position will be:

$$x_n = nx_1 = n2r \cos\left(\frac{\theta}{2}\right) \quad (4.27)$$

Differentiation of Eq. (4.27) gives the velocity of the end effector. Velocity of the end effector for repetition of n identical rhombuses will be:

$$v_n = -nr\omega \sin\left(\frac{\theta}{2}\right) \quad (4.28)$$

We can calculate the angular velocity and acceleration for repetition of rhombus configuration. For a linkage with n repetition of rhombuses, the angular velocity will be:

$$\omega = -v \frac{2}{nr} \frac{1}{\sqrt{4 - \frac{\left(\frac{x}{n}\right)^2}{r^2}}} \quad (4.29)$$

Then, we extrapolated the angular acceleration for a linear actuator constructed with n rhombuses:

$$\alpha = 2 \frac{a}{nr} \frac{1}{\sqrt{4 - \frac{x^2}{n^2 r^2}}} - v^2 x n^{-3} r^{-4} \left(1 - \frac{x^2}{4 n^2 r^2}\right)^{-\frac{3}{2}} \quad (4.30)$$

From the position analysis we have seen that the distance coverage will be double for double networking and using the four bar rhombus formula's it is verified that the velocity of the end effector will also be doubled for double rhombus configuration and will be triple for triple rhombus configuration.

From the rhombus kinematics we can calculate the workspace for networking. For generalized case with n rhombus, the maximum position is:

$$x_{min} = n2r \sin\left(2 \arccos\left(\frac{W}{r}\right)\right) \quad (4.31)$$

The maximum position is calculated using:

$$x_{max} = n2rcos(2 \arcsin (\frac{W}{r})) \quad (4.32)$$

The networking of rhombuses is not affecting the encumbrance. Because, each of the bar width is identical.

4.7 Motion Analysis

Figure 4.5 and Figure 4.6 shows the kinematic performance of the single rhombus and triple rhombus network. From those figures we can see for both cases, end effector maintains almost a linear trajectory with respect to the input angle. Linear velocity and acceleration plot shows variation with time when our target acceleration is 10g. For single network considered link length was 0.4 m and 0.1333 m for triple network.

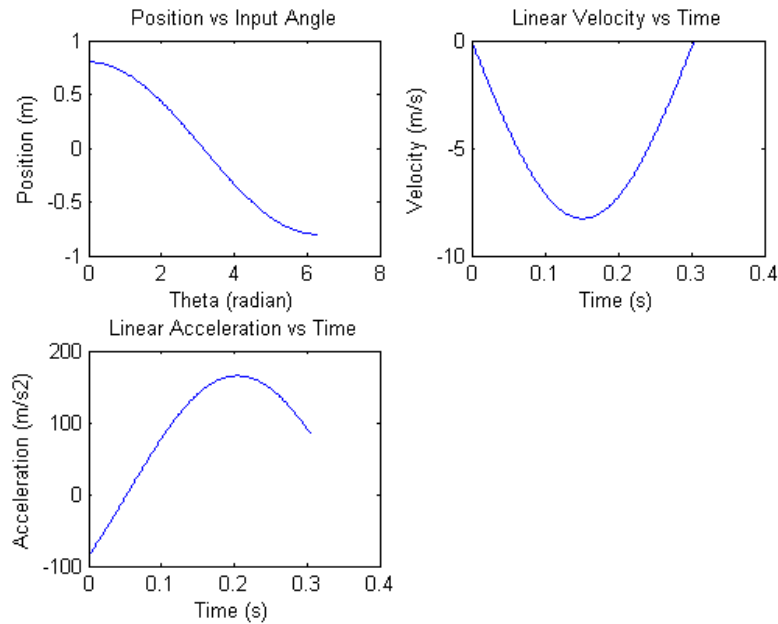


Figure 4.5 Single Network Rhombus Kinematic Performance

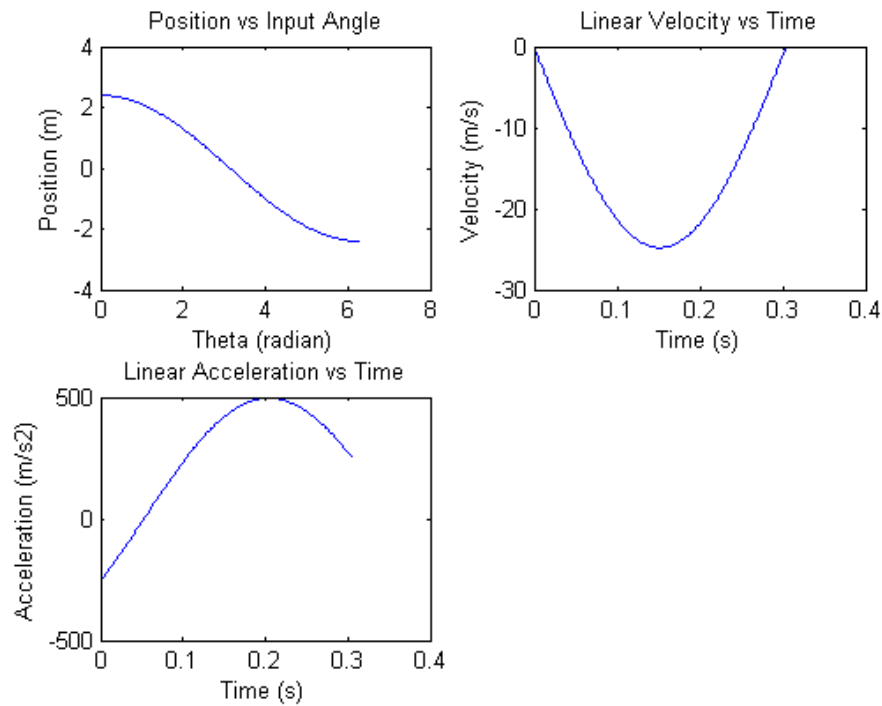


Figure 4.6 Double Network Rhombus Kinematic Performance

4.8 Discussions

From the kinematic formulations and MATLAB simulation we can see that networking of the rhombus configuration increases the velocity and acceleration drastically. Compared to the velocity, there is a more rapid change in the acceleration due to networking. For our newly designed actuator, acceleration is an important criterion. From the kinematic simulation we get a fair idea of how networking improves the performance of the actuator. Here, angular velocity and acceleration of the actuator is derived as a function of the end effector motion. This formulation gives the opportunity to design a controller, where we can command the rotational motion between the links at the revolute end connected to the motor. Commanding such rotary motion can produce good performance, because we can measure it with encoders.

Chapter 5

Lagrangian Dynamic Analysis of the Actuator

5.1 Introduction

This chapter describes the detailed steps in formulating the dynamic equations of the newly designed linear actuator using Lagrangian formulation. Dynamic formulations of the actuator provide the opportunity to use them into the Simulink control model. The Lagrangian dynamic analysis approach is essentially an energy based approach, where we need to know the kinetic and potential energy associated with each link. Here, we used the single and double network rhombus configuration to derive the dynamic equations. There are also discussions on associated complexities as the network number goes higher.

5.2 Lagrangian Formulation for Single Network

This section describes the dynamic analysis of a four bar rhombus configuration. Dynamic analysis is performed by considering the following figure of the four bar rhombus:

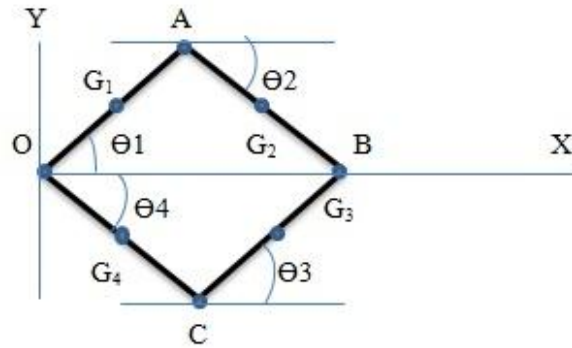


Figure 5.1 Four bar rhombus configuration for dynamic analysis

For detailed analysis of the mechanism, we will consider the following parameters:

$$l_1 = OA = \text{Length of the link 1}$$

$$l_2 = AB = \text{Length of the link 2}$$

$$l_3 = BC = \text{Length of the link 3}$$

$$l_4 = OC = \text{Length of the link 4}$$

$$m_1 = \text{mass of the link 1}$$

$$m_2 = \text{mass of the link 2}$$

$$m_3 = \text{mass of the link 3}$$

$$m_4 = \text{mass of the link 4}$$

$$I_1 = \text{Inertia of link 1 at its center of mass point}$$

$$I_2 = \text{Inertia of link 2 at its center of mass point}$$

I_3 = Inertia of link 3 at its center of mass point

I_4 = Inertia of link 4 at its center of mass point

Angles are considered with respect to a fixed axis at the base extremity. The associated angle for each of the links is mentioned in Figure 4.1.

5.2.1 Lagrangian Function

In Lagrangian formulation, the Lagrangian of the entire system is defined by the total kinetic energy minus the total potential energy of the system [50]. The Lagrangian function of the entire system is given by:

$$L = K - U \quad (5.1)$$

Where,

K = Kinetic Energy

U = Potential Energy

Lagrangian Equation of motion is defined as:

$$Q_i = \frac{d}{dt} \left(\frac{\partial L}{\partial \dot{\theta}_i} \right) - \frac{\partial L}{\partial \theta_i} \quad (5.2)$$

Here,

Q_i = Generalized non conservative force or torque

$i = 1, 2, 3, \dots, n$

The kinetic energy of a typical link can be expressed as:

$$K_i = \left(\frac{1}{2} m_i v_i^2 \right) + \left(\frac{1}{2} I_i \dot{\theta}_i^2 \right) \quad (5.3)$$

Where, v_i is the velocity of the link i and $\dot{\theta}_i$ is the angular velocity of the link, I_i represents the inertia of the link i at its center of mass point.

Potential energy stored in a link is defined as the amount of work required to displace the center of mass of link from the base frame to a certain position. Hence, the potential energy stored in a bar according to Lagrangian formulation is:

$$U_i = -m_i g P_i \quad (5.4)$$

Where P_i is the position vector of the center of mass from the base frame of the link.

5.2.2 Lagrangian Analysis

For the considered mechanism, the Lagrangian function can be written as:

$$L = \left(\frac{1}{2} m_1 v_1^2 + \frac{1}{2} m_2 v_2^2 + \frac{1}{2} m_3 v_3^2 + \frac{1}{2} m_4 v_4^2 \right) + \frac{1}{2} \left(I_1 \dot{\theta}_1^2 + I_2 \dot{\theta}_2^2 + I_3 \dot{\theta}_3^2 + I_4 \dot{\theta}_4^2 \right) - (U_1 + U_2 + U_3 + U_4) \quad (5.5)$$

Velocity of link 1 at G_1 point can be expressed as:

$$v_{G1} = v_O + (\boldsymbol{\omega}_{OA} * \frac{1}{2} \mathbf{r}_{OA}) \quad (5.6)$$

Angular velocity matrix of link 1 is given by:

$$\boldsymbol{\omega}_{OA} = \begin{bmatrix} 0 \\ 0 \\ \dot{\theta}_1 \end{bmatrix} \quad (5.7)$$

Radial position of the center of mass point:

$$\frac{1}{2} \mathbf{r}_{OA} = \begin{bmatrix} \frac{l_1}{2} \cos \theta_1 \\ \frac{l_1}{2} \sin \theta_1 \\ 0 \end{bmatrix} \quad (5.8)$$

Velocity of the bar at point O is zero as this is the fixed point on the base extremity. From the above two equations, we can calculate the velocity of the Link 1 at its center of mass point.

$$v_{G1} = \left(-\frac{1}{2}\dot{\theta}_1 l_1 \sin \theta_1\right) \hat{i} + \left(\frac{1}{2}\dot{\theta}_1 l_1 \cos \theta_1\right) \hat{j} \quad (5.9)$$

From Eq. (5.9) we can write:

$$v_1^2 = v_{G1}^2 = \left(-\frac{1}{2}\dot{\theta}_1 l_1 \sin \theta_1\right)^2 + \left(\frac{1}{2}\dot{\theta}_1 l_1 \cos \theta_1\right)^2 \quad (5.10)$$

$$v_1^2 = v_{G1}^2 = \frac{\dot{\theta}_1^2}{4} l_1^2 \quad (5.11)$$

Velocity at point A can be written as:

$$v_A = (-\dot{\theta}_1 l_1 \sin \theta_1) \hat{i} + (\dot{\theta}_1 l_1 \cos \theta_1) \hat{j} \quad (5.12)$$

Velocity of link 2 at its center of mass:

$$v_2 = v_{G2} = v_A + (\boldsymbol{\omega}_{AB} * \frac{1}{2} \mathbf{r}_{AB}) \quad (5.13)$$

Angular velocity vector for link 2:

$$\boldsymbol{\omega}_{AB} = \begin{bmatrix} 0 \\ 0 \\ \dot{\theta}_2 \end{bmatrix} \quad (5.14)$$

Associated radial vector of the link 2 can be expressed as:

$$\frac{1}{2}\mathbf{r}_{AB} = \begin{bmatrix} \frac{l_2}{2} \cos\theta_2 \\ \frac{l_2}{2} \sin\theta_2 \\ 0 \end{bmatrix} \quad (5.15)$$

Substituting Eq. (5.14) and (5.15) in to Eq. (5.13) we get:

$$v_{G2} = \left(-\dot{\theta}_1 l_1 \sin \theta_1 - \frac{1}{2} \dot{\theta}_2 l_2 \sin \theta_2\right) \hat{i} + \left(\dot{\theta}_1 l_1 \cos \theta_1 + \frac{1}{2} \dot{\theta}_2 l_2 \cos \theta_2\right) \hat{j} \quad (5.16)$$

From Eq. (5.16), we can write:

$$v_2^2 = v_{G2}^2 = \dot{\theta}_1^2 l_1^2 + \frac{\dot{\theta}_2^2}{4} l_2^2 + \dot{\theta}_1 l_1 \dot{\theta}_2 l_2 \cos (\theta_1 - \theta_2) \quad (5.17)$$

For forward movement of the end effector, both link 1 and link 2 will move in the direction of gravity. Potential energy of the link 1:

$$U_1 = -\frac{1}{2} m_1 l_1 g \sin(\theta_1) \quad (5.18)$$

Potential energy stored in the link 2:

$$U_2 = -\frac{1}{2} m_2 l_2 g \sin(\theta_2) \quad (5.19)$$

For backward movement of the end effector, potential energy stored in the link will be opposite of forward movement.

$$U_1 = \frac{1}{2} m_1 l_1 g \sin(\theta_1) \quad (5.20)$$

$$U_2 = \frac{1}{2} m_2 l_2 g \sin(\theta_2) \quad (5.21)$$

Kinematic Energy of each link has rotational and translational components. Rotational kinetic energy of link 1:

$$K_{1R} = \frac{1}{2} I_{G1} \omega_{OA}^2 = \frac{1}{2} \dot{\theta}_1^2 * \frac{m_1 l_1^2}{12} = \dot{\theta}_1^2 * \frac{m_1 l_1^2}{24} \quad (5.22)$$

Translational kinetic energy can be expressed as:

$$K_{1T} = \frac{1}{2} m_1 v_{G1}^2 = \frac{m_1 l_1^2}{8} \dot{\theta}_1^2 \quad (5.23)$$

Total kinetic energy of link 1:

$$K_1 = K_{1T} + K_{1R} = \frac{m_1 l_1^2}{6} \dot{\theta}_1^2 \quad (5.24)$$

In the same way, we can calculate the total kinetic energy of the link 2. Rotational energy:

$$K_{2R} = \frac{m_2 l_2^2}{24} \dot{\theta}_2^2 \quad (5.25)$$

Translational kinetic energy:

$$K_{2T} = \frac{1}{2} m_2 \dot{\theta}_1^2 l_1^2 + \frac{1}{2} \dot{\theta}_1 l_1 \dot{\theta}_2 l_2 m_2 \cos(\theta_1 - \theta_2) + \frac{m_2 l_2^2}{8} \dot{\theta}_2^2 \quad (5.26)$$

Total kinetic energy:

$$K_2 = K_{2T} + K_{2R} = \frac{m_2 l_1^2}{2} \dot{\theta}_1^2 + \frac{m_2 l_2^2}{6} \dot{\theta}_2^2 + \frac{1}{2} \dot{\theta}_1 l_1 \dot{\theta}_2 l_2 m_2 \cos(\theta_1 - \theta_2) \quad (5.27)$$

Lagrangian function for the forward movement:

$$L = \frac{m_1 l_1^2}{6} \dot{\theta}_1^2 + \frac{m_2 l_1^2}{2} \dot{\theta}_1^2 + \frac{m_2 l_2^2}{6} \dot{\theta}_2^2 + \frac{1}{2} \dot{\theta}_1 l_1 \dot{\theta}_2 l_2 m_2 \cos(\theta_1 - \theta_2) \quad (5.28)$$

$$+ \frac{1}{2} m_1 l_1 g \sin(\theta_1) + \frac{1}{2} m_2 l_2 g \sin(\theta_2)$$

Simplifying Eq. (5.28) we get:

$$L = \frac{(m_1 + 3m_2) l_1^2}{6} \dot{\theta}_1^2 + \frac{m_2 l_2^2}{6} \dot{\theta}_2^2 + \frac{1}{2} \dot{\theta}_1 l_1 \dot{\theta}_2 l_2 m_2 \cos(\theta_1 - \theta_2) \quad (5.29)$$

$$+ \frac{1}{2} m_1 l_1 g \sin(\theta_1) + \frac{1}{2} m_2 l_2 g \sin(\theta_2)$$

From Eq. (5.29) we can write:

$$\frac{\partial L}{\partial \dot{\theta}_1} = \frac{(m_1 + 3m_2) l_1^2}{3} \dot{\theta}_1 + \frac{1}{2} l_1 \dot{\theta}_2 l_2 m_2 \cos(\theta_1 - \theta_2) \quad (5.30)$$

For the Lagrangian formulation, we need the derivative of the Eq. (5.30):

$$\frac{d}{dt} \left(\frac{\partial L}{\partial \dot{\theta}_1} \right) = \frac{(m_1 + 3m_2) l_1^2}{3} \ddot{\theta}_1 + \frac{1}{2} l_1 \ddot{\theta}_2 l_2 m_2 \cos(\theta_1 - \theta_2) - \frac{1}{2} l_1 \dot{\theta}_2 l_2 m_2 (\dot{\theta}_1 - \dot{\theta}_2) \sin(\theta_1 - \theta_2) \quad (5.31)$$

Partial derivatives of the Lagrangian function with respect to θ_1 :

$$\frac{\partial L}{\partial \theta_1} = -\frac{1}{2} l_1 \dot{\theta}_1 \dot{\theta}_2 l_2 m_2 \sin(\theta_1 - \theta_2) + \frac{1}{2} m_1 l_1 g \cos(\theta_1) \quad (5.32)$$

For forward directional movement, the total torque of link 1 can be expressed as follows:

$$\begin{aligned} \tau_1 = & \frac{(m_1 + 3m_2)l_1^2}{3}\ddot{\theta}_1 + \frac{1}{2}l_1\ddot{\theta}_2l_2m_2\cos(\theta_1 - \theta_2) - \frac{1}{2}l_1\dot{\theta}_2l_2m_2(\dot{\theta}_1 \\ & - \dot{\theta}_2)\sin(\theta_1 - \theta_2) + \frac{1}{2}l_1\dot{\theta}_1\dot{\theta}_2l_2m_2\sin(\theta_1 - \theta_2) \\ & - \frac{1}{2}m_1l_1g\cos(\theta_1) \end{aligned} \quad (5.33)$$

Lagrangian Equations for link 2 :

$$\frac{\partial L}{\partial \dot{\theta}_2} = \frac{m_2l_2^2}{3}\dot{\theta}_2 + \frac{1}{2}l_1\dot{\theta}_1l_2m_2\cos(\theta_1 - \theta_2) \quad (5.34)$$

$$\begin{aligned} \frac{d}{dt}\left(\frac{\partial L}{\partial \dot{\theta}_2}\right) = & \frac{m_2l_2^2}{3}\ddot{\theta}_2 + \frac{1}{2}l_1\ddot{\theta}_1l_2m_2\cos(\theta_1 - \theta_2) - \frac{1}{2}l_1\dot{\theta}_1l_2m_2(\dot{\theta}_1 \\ & - \dot{\theta}_2)\sin(\theta_1 - \theta_2) \end{aligned} \quad (5.35)$$

$$\frac{\partial L}{\partial \theta_2} = -\frac{1}{2}l_1\dot{\theta}_1\dot{\theta}_2l_2m_2\sin(\theta_2 - \theta_1) + \frac{1}{2}m_2l_2g\cos(\theta_2) \quad (5.36)$$

Required torque for link 2 :

$$\begin{aligned} \tau_2 = & \frac{m_2l_2^2}{3}\ddot{\theta}_2 + \frac{1}{2}l_1\ddot{\theta}_1l_2m_2\cos(\theta_1 - \theta_2) - \frac{1}{2}l_1\dot{\theta}_1l_2m_2(\dot{\theta}_1 - \dot{\theta}_2)\sin(\theta_1 \\ & - \theta_2) + \frac{1}{2}l_1\dot{\theta}_1\dot{\theta}_2l_2m_2\sin(\theta_2 - \theta_1) - \frac{1}{2}m_2l_2g\cos(\theta_2) \end{aligned} \quad (5.37)$$

In the four bar rhombus configuration, link 1 and 2 form symmetry with link 3 and 4. Kinematic energy equations are also the same, and there will be change in the potential energy equations due to the change in the link movement direction. So, we can calculate the torque equations by using Eq. (5.33) and Eq. (5.37). Torque of link 3:

$$\begin{aligned} \tau_3 = & \frac{m_3 l_3^2}{3} \ddot{\theta}_3 + \frac{1}{2} l_3 \ddot{\theta}_4 l_4 m_3 \cos(\theta_4 - \theta_3) - \frac{1}{2} l_3 \dot{\theta}_4 l_4 m_3 (\dot{\theta}_4 - \dot{\theta}_3) \sin(\theta_4 \\ & - \theta_3) + \frac{1}{2} l_3 \dot{\theta}_3 \dot{\theta}_4 l_4 m_3 \sin(\theta_3 - \theta_4) + \frac{1}{2} m_3 l_3 g \cos(\theta_3) \end{aligned} \quad (5.38)$$

Required torque equation for link 4:

$$\begin{aligned} \tau_4 = & \frac{(m_4 + 3m_3) l_4^2}{3} \ddot{\theta}_4 + \frac{1}{2} l_4 \dot{\theta}_3 l_3 m_3 \cos(\theta_4 - \theta_3) - \frac{1}{2} l_4 \dot{\theta}_3 l_3 m_3 (\dot{\theta}_4 \\ & - \dot{\theta}_3) \sin(\theta_4 - \theta_3) + \frac{1}{2} l_4 \dot{\theta}_4 \dot{\theta}_3 l_3 m_3 \sin(\theta_4 - \theta_3) \\ & + \frac{1}{2} m_4 l_4 g \cos(\theta_4) \end{aligned} \quad (5.39)$$

In matrix form, Lagrangian equation of motion is:

$$Q = M\ddot{\theta}_l + N + G \quad (5.40)$$

Where,

M = Mass or Inertia Matrix

N = Nonlinear Matrix

G = Gravity matrix

Q = Torque Matrix

For the four bar rhombus configuration, the Lagrangian equation of motion is:

$$\begin{bmatrix} \tau_1 \\ \tau_2 \\ \tau_3 \\ \tau_4 \end{bmatrix} = \begin{bmatrix} M_{11} & M_{12} & 0 & 0 \\ M_{21} & M_{22} & 0 & 0 \\ 0 & 0 & M_{33} & M_{34} \\ 0 & 0 & M_{41} & M_{42} \end{bmatrix} \begin{bmatrix} \ddot{\theta}_1 \\ \ddot{\theta}_2 \\ \ddot{\theta}_3 \\ \ddot{\theta}_4 \end{bmatrix} + \begin{bmatrix} -\frac{1}{2}l_1\dot{\theta}_2l_2m_2(\dot{\theta}_1 - \dot{\theta}_2)\sin(\theta_1 - \theta_2) + \frac{1}{2}l_1\dot{\theta}_1\dot{\theta}_2l_2m_2\sin(\theta_1 - \theta_2) \\ -\frac{1}{2}l_1\dot{\theta}_1l_2m_2(\dot{\theta}_1 - \dot{\theta}_2)\sin(\theta_1 - \theta_2) + \frac{1}{2}l_1\dot{\theta}_1\dot{\theta}_2l_2m_2\sin(\theta_2 - \theta_1) \\ -\frac{1}{2}l_3\dot{\theta}_4l_4m_3(\dot{\theta}_4 - \dot{\theta}_3)\sin(\theta_4 - \theta_3) + \frac{1}{2}l_3\dot{\theta}_3\dot{\theta}_4l_4m_3\sin(\theta_3 - \theta_4) \\ -\frac{1}{2}l_4\dot{\theta}_3l_3m_3(\dot{\theta}_4 - \dot{\theta}_3)\sin(\theta_4 - \theta_3) + \frac{1}{2}l_4\dot{\theta}_4\dot{\theta}_3l_3m_3\sin(\theta_4 - \theta_3) \end{bmatrix} + \begin{bmatrix} -\frac{1}{2}m_1l_1g\cos(\theta_1) \\ -\frac{1}{2}m_2l_2g\cos(\theta_2) \\ \frac{1}{2}m_3l_3g\cos(\theta_3) \\ \frac{1}{2}m_4l_4g\cos(\theta_4) \end{bmatrix} \quad (5.41)$$

Here,

$$M_{11} = \frac{(m_1 + 3m_2)l_1^2}{3} \text{ and } M_{44} = \frac{(m_4 + 3m_3)l_4^2}{3}$$

$$M_{12} = M_{21} = \frac{1}{2}l_1l_2m_2\cos(\theta_1 - \theta_2)$$

$$M_{33} = \frac{m_3l_3^2}{3} \text{ and } M_{22} = \frac{m_2l_2^2}{3}$$

$$M_{34} = M_{43} = \frac{1}{2}l_4l_3m_3\cos(\theta_4 - \theta_3)$$

For backward motion of the end effector, only the sign of the gravity matrix components will change. The other matrices will remain same. Gravity matrix for backward movement:

$$G = \begin{bmatrix} \frac{1}{2}m_1l_1g\cos(\theta_1) \\ \frac{1}{2}m_2l_2g\cos(\theta_2) \\ -\frac{1}{2}m_3l_3g\cos(\theta_3) \\ -\frac{1}{2}m_4l_4g\cos(\theta_4) \end{bmatrix} \quad (5.42)$$

5.3 Lagrangian Formulation for Double Network

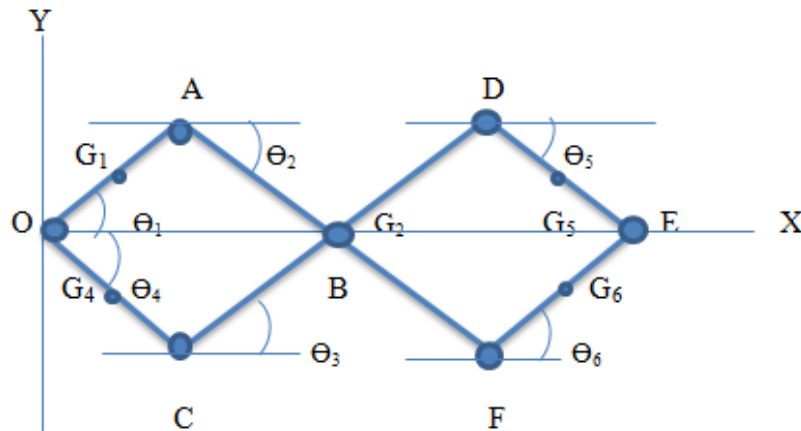


Figure 5.2 Four bar double network rhombus configuration for dynamic analysis

Figure 5.2 shows a double rhombus network. For detailed analysis of the mechanism, we will consider following parameter:

$$l_1 = OA = \text{Length of the link 1}$$

$$l_2 = AF = \text{Length of the link 2}$$

$l_3 = CD =$ Length of the link 3

$l_4 = OC =$ Length of the link 4

$l_5 = DE =$ Length of the link 5

$l_6 = FE =$ Length of the link 6

$m_1 =$ mass of the link 1

$m_2 =$ mass of the link 2

$m_3 =$ mass of the link 3

$m_4 =$ mass of the link 4

$m_5 =$ mass of the link 5

$m_6 =$ mass of the link 6

$I_1 =$ Inertia of link 1 at its center of mass point

$I_2 =$ Inertia of link 2 at its center of mass point

$I_3 =$ Inertia of link 3 at its center of mass point

$I_4 =$ Inertia of link 4 at its center of mass point

$I_5 =$ Inertia of link 5 at its center of mass point

$I_6 =$ Inertia of link 6 at its center of mass point

From single network analysis, we can directly write the velocity equation for link1:

$$v_1^2 = v_{G1}^2 = \frac{\dot{\theta}_1^2}{4} l_1^2 \quad (5.43)$$

Velocity of link 2 at its center of mass point:

$$v_2 = v_{G2} = v_A + (\boldsymbol{\omega}_{AF} * \frac{1}{2} \mathbf{r}_{AF}) \quad (5.44)$$

In the double network for horizontal movement, G₂ point has no vertical displacement along the Y axis. It will only travel along the X axis.

$$v_{G2} = (-\dot{\theta}_1 l_1 \sin \theta_1) \hat{i} + (\dot{\theta}_1 l_1 \cos \theta_1) \hat{j} + \begin{bmatrix} 0 \\ 0 \\ \dot{\theta}_2 \end{bmatrix} * \begin{bmatrix} \frac{l_2}{2} \cos \theta_2 \\ 0 \\ 0 \end{bmatrix} \quad (5.45)$$

After vector multiplication, Eq. (5.45) becomes:

$$v_{G2} = (-\dot{\theta}_1 l_1 \sin \theta_1) \hat{i} + (\dot{\theta}_1 l_1 \cos \theta_1) \hat{j} + \left(\dot{\theta}_2 \frac{l_2}{2} \cos \theta_2 \right) \hat{j} \quad (5.46)$$

$$v_{G2} = (-\dot{\theta}_1 l_1 \sin \theta_1) \hat{i} + \left(\dot{\theta}_1 l_1 \cos \theta_1 + \dot{\theta}_2 \frac{l_2}{2} \cos \theta_2 \right) \hat{j} \quad (5.47)$$

Square of the both side of Eq. (5.47) gives:

$$v_2^2 = v_{G2}^2 = \dot{\theta}_1^2 l_1^2 + \dot{\theta}_1 l_1 \dot{\theta}_2 l_2 \cos \theta_1 \cos \theta_2 + \frac{l_2^2}{4} \dot{\theta}_2^2 \cos^2(\theta_2) \quad (5.48)$$

From previous analysis, velocity of the link 4 is:

$$v_4^2 = v_{G4}^2 = \frac{\dot{\theta}_4^2}{4} l_4^2 \quad (5.49)$$

From Eq. (5.48), we can derive the velocity square equation for link 3:

$$v_3^2 = v_{G3}^2 = \dot{\theta}_4^2 l_4^2 + \dot{\theta}_3 l_3 \dot{\theta}_4 l_4 \cos \theta_3 \cos \theta_4 + \frac{l_3^2}{4} \dot{\theta}_3^2 \cos^2(\theta_3) \quad (5.50)$$

In double network rhombus configuration, link 1, 2 and 6 form one side. The other side contains link 4, 3 and 5. For velocity of link 6, we need to calculate velocity at F point.

Velocity at F point:

$$v_F = v_{G2} + (\boldsymbol{\omega}_{AF} * \frac{1}{2} \mathbf{r}_{BF}) \quad (5.51)$$

Putting the values into the Eq. (5.51) we get:

$$v_F = (-\dot{\theta}_1 l_1 \sin \theta_1) \hat{i} + \left(\dot{\theta}_1 l_1 \cos \theta_1 + \frac{l_2}{2} \dot{\theta}_2 \cos \theta_2 \right) \hat{j} + \begin{bmatrix} 0 \\ 0 \\ \dot{\theta}_2 \end{bmatrix} * \begin{bmatrix} \frac{l_2}{2} \cos \theta_2 \\ \frac{l_2}{2} \sin \theta_2 \\ 0 \end{bmatrix} \quad (5.52)$$

From Eq. (5.52), we can write:

$$v_F = \left(-\dot{\theta}_1 l_1 \sin \theta_1 - \dot{\theta}_2 \frac{l_2}{2} \sin \theta_2 \right) \hat{i} + \left(\dot{\theta}_1 l_1 \cos \theta_1 + \dot{\theta}_2 l_2 \cos \theta_2 \right) \hat{j} \quad (5.53)$$

Velocity of link 6 at its center of mass point:

$$v_{G6} = v_F + (\boldsymbol{\omega}_{FE} * \frac{1}{2} \mathbf{r}_{EF}) \quad (5.54)$$

We already know the velocity at the F point. By substituting the values of v_F from Eq. (5.53) and the vector matrices we get:

$$v_{G6} = \left(-\dot{\theta}_1 l_1 \sin \theta_1 - \dot{\theta}_2 \frac{l_2}{2} \sin \theta_2 \right) \hat{i} + \left(\dot{\theta}_1 l_1 \cos \theta_1 + \dot{\theta}_2 l_2 \cos \theta_2 \right) \hat{j} + \begin{bmatrix} 0 \\ 0 \\ \dot{\theta}_6 \end{bmatrix} * \begin{bmatrix} \frac{l_6}{2} \cos \theta_6 \\ \frac{l_6}{2} \sin \theta_6 \\ 0 \end{bmatrix} \quad (5.55)$$

Resultant velocity after vector multiplication:

$$v_{G6} = \left(-\dot{\theta}_1 l_1 \sin \theta_1 - \dot{\theta}_2 \frac{l_2}{2} \sin \theta_2 - \dot{\theta}_6 \frac{l_6}{2} \sin \theta_6 \right) \hat{i} + \left(\dot{\theta}_1 l_1 \cos \theta_1 + \dot{\theta}_2 l_2 \cos \theta_2 + \dot{\theta}_6 \frac{l_6}{2} \cos \theta_6 \right) \hat{j} \quad (5.56)$$

From Eq. (5.56) we can write:

$$v_6^2 = v_{G6}^2 = \left(-\dot{\theta}_1 l_1 \sin \theta_1 - \dot{\theta}_2 \frac{l_2}{2} \sin \theta_2 - \dot{\theta}_6 \frac{l_6}{2} \sin \theta_6 \right)^2 + \left(\dot{\theta}_1 l_1 \cos \theta_1 + \dot{\theta}_2 l_2 \cos \theta_2 + \dot{\theta}_6 \frac{l_6}{2} \cos \theta_6 \right)^2 \quad (5.57)$$

By solving Eq. (5.57) we get:

$$v_6^2 = v_{G6}^2 = \dot{\theta}_1^2 l_1^2 + \frac{\dot{\theta}_6^2}{4} l_6^2 + \dot{\theta}_1 l_1 \dot{\theta}_6 l_6 \cos(\theta_1 - \theta_6) + \frac{l_2^2}{4} \dot{\theta}_2^2 \sin^2(\theta_2) + \dot{\theta}_2^2 l_2^2 \cos^2(\theta_2) + \dot{\theta}_1 l_1 \dot{\theta}_2 l_2 \sin \theta_1 \sin \theta_2 + 2 \dot{\theta}_1 l_1 \dot{\theta}_2 l_2 \cos \theta_1 \cos \theta_2 + \dot{\theta}_2 l_2 \dot{\theta}_6 \frac{l_6}{2} \sin \theta_2 \sin \theta_6 + \dot{\theta}_2 l_2 \dot{\theta}_6 l_6 \cos \theta_2 \cos \theta_6 \quad (5.58)$$

Potential energy of link 1 due to forward movement:

$$U_1 = -\frac{1}{2} m l g \sin(\theta_1) \quad (5.59)$$

In Figure 5.2, link 2 and link 3 are connected in their center of mass pint G_2 . At this point, there is no vertical deflection and the bars are opposing each other's gravity effect. So, there will be no gravity effect for link 2 and link 3.

$$U_2 = 0 \quad (5.60)$$

Potential energy stored at center of mass point of link 6:

$$U_6 = -\frac{1}{2} m l g \sin(\theta_6) \quad (5.61)$$

For backward movement potential energy will remain same only their sign will be opposite of forward moment.

Rotational kinematic energy of the each link 1:

$$K_{1R} = \frac{1}{2} \dot{\theta}_1^2 * \frac{m_1 l_1^2}{12} = \dot{\theta}_1^2 * \frac{m_1 l_1^2}{24} \quad (5.62)$$

Translational kinetic energy:

$$K_{1T} = \frac{1}{2} m_1 v_{G1}^2 = \frac{m_1 l_1^2}{8} \dot{\theta}_1^2 \quad (5.63)$$

Total kinetic energy:

$$K_1 = K_{1T} + K_{1R} = \frac{m_1 l_1^2}{6} \dot{\theta}_1^2 \quad (5.63)$$

Rotational component of kinetic energy for link 2:

$$K_{2R} = \frac{m_2 l_2^2}{24} \dot{\theta}_2^2 \quad (5.64)$$

Translational component:

$$K_{2T} = \frac{1}{2} m_2 \dot{\theta}_1^2 l_1^2 + \frac{1}{2} \dot{\theta}_1 l_1 \dot{\theta}_2 l_2 m_2 \cos \theta_1 \cos \theta_2 + \frac{m_2 l_2^2}{8} \dot{\theta}_2^2 \cos^2(\theta_2) \quad (5.65)$$

Energy equations for link 6:

$$K_{6R} = \frac{m_6 l_6^2}{24} \dot{\theta}_6^2 \quad (5.66)$$

$$\begin{aligned} K_{6T} = & \frac{1}{2} m_6 \dot{\theta}_1^2 l_1^2 + \frac{1}{8} m_6 \dot{\theta}_6^2 l_6^2 + \frac{1}{2} \dot{\theta}_1 l_1 \dot{\theta}_6 l_6 m_6 \cos(\theta_1 - \theta_6) \quad (5.67) \\ & + \frac{m_6 l_2^2}{8} \dot{\theta}_2^2 \sin^2(\theta_2) + \frac{1}{2} \dot{\theta}_1 l_1 \dot{\theta}_2 l_2 m_6 \sin \theta_1 \sin \theta_2 \\ & + \dot{\theta}_1 l_1 \dot{\theta}_2 l_2 m_6 \cos \theta_1 \cos \theta_2 + \frac{1}{4} \dot{\theta}_2 l_2 \dot{\theta}_6 l_6 m_6 \sin \theta_2 \sin \theta_6 \\ & + \frac{1}{2} \dot{\theta}_2 l_2 \dot{\theta}_6 l_6 m_6 \cos \theta_2 \cos \theta_6 + \frac{m_6 l_2^2}{2} \dot{\theta}_2^2 \cos^2(\theta_2) \end{aligned}$$

Total kinetic energy for forward movement (link 1, 2 and 6):

$$\begin{aligned} K_{1+2+6} = & \frac{m_1 l_1^2}{6} \dot{\theta}_1^2 + \frac{m_2 l_2^2}{24} \dot{\theta}_2^2 + \frac{1}{2} m_2 \dot{\theta}_1^2 l_1^2 + \frac{1}{2} \dot{\theta}_1 l_1 \dot{\theta}_2 l_2 m_2 \cos \theta_1 \cos \theta_2 \quad (5.68) \\ & + \frac{m_2 l_2^2}{8} \dot{\theta}_2^2 \cos^2(\theta_2) + \frac{m_6 l_6^2}{24} \dot{\theta}_6^2 + \frac{1}{2} m_6 \dot{\theta}_1^2 l_1^2 + \frac{1}{8} m_6 \dot{\theta}_6^2 l_6^2 \\ & + \frac{1}{2} \dot{\theta}_1 l_1 \dot{\theta}_6 l_6 m_6 \cos(\theta_1 - \theta_6) + \frac{m_6 l_2^2}{8} \dot{\theta}_2^2 \sin^2(\theta_2) \\ & + \frac{1}{2} \dot{\theta}_1 l_1 \dot{\theta}_2 l_2 m_6 \sin \theta_1 \sin \theta_2 + \dot{\theta}_1 l_1 \dot{\theta}_2 l_2 m_6 \cos \theta_1 \cos \theta_2 \\ & + \frac{1}{4} \dot{\theta}_2 l_2 \dot{\theta}_6 l_6 m_6 \sin \theta_2 \sin \theta_6 + \frac{1}{2} \dot{\theta}_2 l_2 \dot{\theta}_6 l_6 m_6 \cos \theta_2 \cos \theta_6 \\ & + \frac{m_6 l_2^2}{2} \dot{\theta}_2^2 \cos^2(\theta_2) \end{aligned}$$

For the rhombus network, we consider the mass and length of the short links identical, which means $m_1 = m_4 = m_5 = m_6 = m$, and $l_1 = l_4 = l_5 = l_6 = l$. Long links mass and lengths are twice that of short links. For long links $m_2 = m_3 = 2m$ and $l_2 = l_3 = 2l$.

$$\begin{aligned}
K_{1+2+6} = & \frac{5ml^2}{3} \dot{\theta}_1^2 + \frac{ml^2}{3} \dot{\theta}_2^2 + 3ml^2 \dot{\theta}_2^2 \cos^2(\theta_2) + \frac{ml^2}{6} \dot{\theta}_6^2 \\
& + 4ml^2 \dot{\theta}_1 \dot{\theta}_2 \cos \theta_1 \cos \theta_2 + \frac{1}{2} \dot{\theta}_1 \dot{\theta}_6 ml^2 \cos(\theta_1 - \theta_6) \\
& + \frac{ml^2}{2} \dot{\theta}_2^2 \sin^2(\theta_2) + ml^2 \dot{\theta}_1 \dot{\theta}_2 \sin \theta_1 \sin \theta_2 \\
& + \frac{1}{2} ml^2 \dot{\theta}_2 \dot{\theta}_6 \sin \theta_2 \sin \theta_6 + ml^2 \dot{\theta}_2 \dot{\theta}_6 \cos \theta_2 \cos \theta_6
\end{aligned} \tag{5.69}$$

Lagrangian function for double network :

$$\begin{aligned}
L = & \frac{5ml^2}{3} \dot{\theta}_1^2 + \frac{ml^2}{3} \dot{\theta}_2^2 + 3ml^2 \dot{\theta}_2^2 \cos^2(\theta_2) + \frac{ml^2}{6} \dot{\theta}_6^2 \\
& + 4ml^2 \dot{\theta}_1 \dot{\theta}_2 \cos \theta_1 \cos \theta_2 + \frac{1}{2} \dot{\theta}_1 \dot{\theta}_6 ml^2 \cos(\theta_1 - \theta_6) \\
& + \frac{ml^2}{2} \dot{\theta}_2^2 \sin^2(\theta_2) + ml^2 \dot{\theta}_1 \dot{\theta}_2 \sin \theta_1 \sin \theta_2 \\
& + \frac{1}{2} ml^2 \dot{\theta}_2 \dot{\theta}_6 \sin \theta_2 \sin \theta_6 + ml^2 \dot{\theta}_2 \dot{\theta}_6 \cos \theta_2 \cos \theta_6 \\
& + \frac{1}{2} mlg \sin \theta_1 - \frac{1}{2} mlg \sin \theta_6
\end{aligned} \tag{5.70}$$

We need to calculate the necessary equations to formulate the Lagrangian dynamic equation. As in the single network analysis, we can follow the same steps to construct the equations.

$$\begin{aligned} \frac{\partial L}{\partial \dot{\theta}_1} = & \frac{10 ml^2}{3} \dot{\theta}_1 + 4ml^2 \dot{\theta}_2 \cos \theta_1 \cos \theta_2 + \frac{1}{2} \dot{\theta}_6 ml^2 \cos (\theta_1 - \theta_6) \\ & + ml^2 \dot{\theta}_2 \sin \theta_1 \sin \theta_2 \end{aligned} \quad (5.71)$$

Derivative of Eq. (5.71) gives:

$$\begin{aligned} \frac{d}{dt} \left(\frac{\partial L}{\partial \dot{\theta}_1} \right) = & \frac{10 ml^2}{3} \ddot{\theta}_1 + 4ml^2 \ddot{\theta}_2 \cos \theta_1 \cos \theta_2 - 4m\dot{\theta}_1 l^2 \dot{\theta}_2 \sin \theta_1 \cos \theta_2 \\ & - 4ml^2 \dot{\theta}_2^2 \cos \theta_1 \sin \theta_2 + \frac{1}{2} \ddot{\theta}_6 ml^2 \cos (\theta_1 - \theta_6) - \frac{1}{2} \dot{\theta}_6 ml^2 (\dot{\theta}_1 \\ & - \dot{\theta}_6) \sin (\theta_1 - \theta_6) + ml^2 \ddot{\theta}_2 \sin \theta_1 \sin \theta_2 \\ & + m\dot{\theta}_1 l^2 \dot{\theta}_2 \cos \theta_1 \sin \theta_2 + ml^2 \dot{\theta}_2^2 \sin \theta_1 \cos \theta_2 \end{aligned} \quad (5.72)$$

$$\begin{aligned} \left(\frac{\partial L}{\partial \theta_1} \right) = & -4m\dot{\theta}_1 l^2 \dot{\theta}_2 \sin \theta_1 \cos \theta_2 - \frac{1}{2} \dot{\theta}_6 \dot{\theta}_1 ml^2 \sin (\theta_1 - \theta_6) \\ & + m\dot{\theta}_1 l^2 \dot{\theta}_2 \cos \theta_1 \sin \theta_2 + \frac{1}{2} mlg \cos \theta_1 \end{aligned} \quad (5.73)$$

Total required torque for link 1:

$$\begin{aligned}
 \tau_1 = & \frac{10 ml^2}{3} \ddot{\theta}_1 + 4ml^2 \ddot{\theta}_2 \cos \theta_1 \cos \theta_2 - 4m\dot{\theta}_1 l^2 \dot{\theta}_2 \sin \theta_1 \cos \theta_2 \\
 & - 4ml^2 \dot{\theta}_2^2 \cos \theta_1 \sin \theta_2 + \frac{1}{2} \ddot{\theta}_6 ml^2 \cos (\theta_1 - \theta_6) - \frac{1}{2} \dot{\theta}_6 ml^2 (\dot{\theta}_1 \\
 & - \dot{\theta}_6) \sin (\theta_1 - \theta_6) + ml^2 \ddot{\theta}_2 \sin \theta_1 \sin \theta_2 \\
 & + m\dot{\theta}_1 l^2 \dot{\theta}_2 \cos \theta_1 \sin \theta_2 + ml^2 \dot{\theta}_2^2 \sin \theta_1 \cos \theta_2 \\
 & + 4m\dot{\theta}_1 l^2 \dot{\theta}_2 \sin \theta_1 \cos \theta_2 + \frac{1}{2} \dot{\theta}_6 \dot{\theta}_1 ml^2 \sin (\theta_1 - \theta_6) \\
 & - m\dot{\theta}_1 l^2 \dot{\theta}_2 \cos \theta_1 \sin \theta_2 - \frac{1}{2} mlg \cos \theta_1
 \end{aligned} \tag{5.74}$$

In the same way, we can write the equations for link 2:

$$\begin{aligned}
 \frac{\partial L}{\partial \dot{\theta}_2} = & \frac{2 ml^2}{3} \dot{\theta}_2 + 6ml^2 \dot{\theta}_2 \cos^2 (\theta_2) + 4ml^2 \dot{\theta}_1 \cos \theta_1 \cos \theta_2 + ml^2 \dot{\theta}_2 \sin^2 (\theta_2) \\
 & + ml^2 \dot{\theta}_1 \sin \theta_1 \sin \theta_2 + \frac{1}{2} ml^2 \dot{\theta}_6 \sin \theta_2 \sin \theta_6 \\
 & + ml^2 \dot{\theta}_6 \cos \theta_2 \cos \theta_6
 \end{aligned} \tag{5.74}$$

From Eq. (5.74) we can write:

$$\begin{aligned}
\frac{d}{dt} \left(\frac{\partial L}{\partial \dot{\theta}_2} \right) &= \frac{2ml^2}{3} \ddot{\theta}_2 + 6ml^2 \ddot{\theta}_2 \cos^2(\theta_2) - 12ml^2 \dot{\theta}_2 \cos \theta_2 \sin \theta_2 \\
&+ 4ml^2 \ddot{\theta}_1 \cos \theta_1 \cos \theta_2 - 4ml^2 \dot{\theta}_1^2 \cos \theta_2 \sin \theta_1 \\
&- 4m\dot{\theta}_1 l^2 \dot{\theta}_2 \cos \theta_1 \sin \theta_2 + ml^2 \ddot{\theta}_2 \sin^2(\theta_2) \\
&+ 2ml^2 \dot{\theta}_2 \sin \theta_2 \cos \theta_2 + ml^2 \ddot{\theta}_1 \sin \theta_1 \sin \theta_2 \\
&+ ml^2 \dot{\theta}_1^2 \cos \theta_1 \sin \theta_2 + m\dot{\theta}_1 l^2 \dot{\theta}_2 \sin \theta_1 \cos \theta_2 \\
&+ \frac{1}{2} ml^2 \ddot{\theta}_6 \sin \theta_2 \sin \theta_6 + \frac{1}{2} m\dot{\theta}_2 l^2 \dot{\theta}_6 \sin \theta_6 \cos \theta_2 \\
&+ \frac{1}{2} ml^2 \dot{\theta}_6^2 \cos \theta_6 \sin \theta_2 + ml^2 \ddot{\theta}_6 \cos \theta_2 \cos \theta_6 \\
&- m\dot{\theta}_2 l^2 \dot{\theta}_6 \sin \theta_2 \cos \theta_6 - ml^2 \dot{\theta}_6^2 \cos \theta_2 \sin \theta_6
\end{aligned} \tag{5.75}$$

Partial derivative of Lagrangian function with respect to θ_2 gives:

$$\begin{aligned}
\frac{\partial L}{\partial \theta_2} &= -5ml^2 \dot{\theta}_2^2 \cos \theta_2 \sin \theta_2 - 4m\dot{\theta}_1 l^2 \dot{\theta}_2 \cos \theta_1 \sin \theta_2 \\
&+ m\dot{\theta}_1 l^2 \dot{\theta}_2 \cos \theta_2 \sin \theta_1 + \frac{1}{2} m\dot{\theta}_2 l^2 \dot{\theta}_6 \sin \theta_6 \cos \theta_2 \\
&- m\dot{\theta}_2 l^2 \dot{\theta}_6 \sin \theta_2 \cos \theta_6
\end{aligned} \tag{5.76}$$

Required torque for link 2:

$$\begin{aligned}
 \tau_2 = & \frac{2ml^2}{3}\ddot{\theta}_2 + ml^2\ddot{\theta}_2(6\cos^2(\theta_2) + \sin^2(\theta_2)) - 10ml^2\dot{\theta}_2\cos\theta_2\sin\theta_2 \\
 & + ml^2\ddot{\theta}_1(4\cos\theta_1\cos\theta_2 + \sin\theta_1\sin\theta_2) \\
 & + ml^2\dot{\theta}_1^2(\cos\theta_1\sin\theta_2 - 4\cos\theta_2\sin\theta_1) \\
 & + ml^2\ddot{\theta}_6\left(\frac{1}{2}\sin\theta_2\sin\theta_6 + \cos\theta_2\cos\theta_6\right) \\
 & + ml^2\dot{\theta}_6^2\left(\frac{1}{2}\cos\theta_6\sin\theta_2 - \sin\theta_6\cos\theta_2\right) \\
 & - m\dot{\theta}_2l^2\dot{\theta}_6\sin\theta_2\cos\theta_6 - 5ml^2\dot{\theta}_2^2\cos\theta_2\sin\theta_2
 \end{aligned} \tag{5.77}$$

For link 6:

$$\begin{aligned}
 \frac{\partial L}{\partial \dot{\theta}_6} = & \frac{ml^2}{3}\dot{\theta}_6 + ml^2\dot{\theta}_2\cos\theta_2\cos\theta_6 + \frac{1}{2}\dot{\theta}_1ml^2\cos(\theta_1 - \theta_6) \\
 & + \frac{1}{2}ml^2\dot{\theta}_2\sin\theta_2\sin\theta_6
 \end{aligned} \tag{5.78}$$

From Eq. (5.78) we get:

$$\begin{aligned}
 \frac{d}{dt}\left(\frac{\partial L}{\partial \dot{\theta}_6}\right) = & \frac{ml^2}{3}\ddot{\theta}_6 + \frac{1}{2}\ddot{\theta}_1ml^2\cos(\theta_1 - \theta_6) - \frac{1}{2}\dot{\theta}_1ml^2(\dot{\theta}_1 - \dot{\theta}_6)\sin(\theta_1 \\
 & - \theta_6) + ml^2\ddot{\theta}_2\left(\frac{1}{2}\sin\theta_2\sin\theta_6 + \cos\theta_2\cos\theta_6\right) \\
 & - \frac{1}{2}\dot{\theta}_2ml^2\sin(\theta_2 + \theta_6)
 \end{aligned} \tag{5.79}$$

$$\begin{aligned} \frac{\partial L}{\partial \theta_6} = & -\frac{1}{2} m \dot{\theta}_1 l^2 \dot{\theta}_6 \sin (\theta_6 - \theta_1) + \frac{1}{2} m \dot{\theta}_2 l^2 \dot{\theta}_6 \sin \theta_2 \cos \theta_6 \\ & - m \dot{\theta}_2 l^2 \dot{\theta}_6 \sin \theta_6 \cos \theta_2 - \frac{1}{2} m l g \cos \theta_6 \end{aligned} \quad (5.80)$$

Associated torque of link 6:

$$\begin{aligned} \tau_6 = & \frac{m l^2}{3} \ddot{\theta}_6 + \frac{1}{2} \ddot{\theta}_1 m l^2 \cos (\theta_1 - \theta_6) - \frac{1}{2} \dot{\theta}_1 m l^2 (\dot{\theta}_1 - \dot{\theta}_6) \sin (\theta_1 - \theta_6) \\ & + m l^2 \ddot{\theta}_2 \left(\frac{1}{2} \sin \theta_2 \sin \theta_6 + \cos \theta_2 \cos \theta_6 \right) - \frac{1}{2} \dot{\theta}_2 m l^2 \sin (\theta_2 \\ & + \theta_6) + \frac{1}{2} m \dot{\theta}_1 l^2 \dot{\theta}_6 \sin (\theta_6 - \theta_1) - \frac{1}{2} m \dot{\theta}_2 l^2 \dot{\theta}_6 \sin \theta_2 \cos \theta_6 \\ & + m \dot{\theta}_2 l^2 \dot{\theta}_6 \sin \theta_6 \cos \theta_2 + \frac{1}{2} m l g \cos \theta_6 \end{aligned} \quad (5.81)$$

Torque equation of link 4 is similar to link 1. From Eq. (5.74)

$$\begin{aligned} \tau_4 = & \frac{10 m l^2}{3} \ddot{\theta}_4 + 4 m l^2 \ddot{\theta}_3 \cos \theta_4 \cos \theta_3 - 4 m \dot{\theta}_3 l^2 \dot{\theta}_4 \sin \theta_4 \cos \theta_3 \\ & - 4 m l^2 \dot{\theta}_3^2 \cos \theta_4 \sin \theta_3 + \frac{1}{2} \ddot{\theta}_5 m l^2 \cos (\theta_4 - \theta_5) - \frac{1}{2} \dot{\theta}_5 m l^2 (\dot{\theta}_4 \\ & - \dot{\theta}_5) \sin (\theta_4 - \theta_5) + m l^2 \ddot{\theta}_3 \sin \theta_4 \sin \theta_3 \\ & + m \dot{\theta}_3 l^2 \dot{\theta}_4 \cos \theta_4 \sin \theta_3 + m l^2 \dot{\theta}_3^2 \sin \theta_4 \cos \theta_3 \\ & + 4 m \dot{\theta}_4 l^2 \dot{\theta}_3 \sin \theta_4 \cos \theta_3 + \frac{1}{2} \dot{\theta}_4 \dot{\theta}_5 m l^2 \sin (\theta_4 - \theta_5) \\ & - m \dot{\theta}_4 l^2 \dot{\theta}_3 \cos \theta_4 \sin \theta_3 + \frac{1}{2} m l g \cos \theta_4 \end{aligned} \quad (5.82)$$

Torque equation of link 3:

$$\begin{aligned}
\tau_3 = & \frac{2ml^2}{3}\ddot{\theta}_3 + ml^2\ddot{\theta}_3(6\cos^2(\theta_3) + \sin^2(\theta_3)) - 10ml^2\dot{\theta}_3\cos\theta_3\sin\theta_3 \\
& + ml^2\ddot{\theta}_4(4\cos\theta_4\cos\theta_3 + \sin\theta_4\sin\theta_3) \\
& + ml^2\dot{\theta}_4^2(\cos\theta_4\sin\theta_3 - 4\cos\theta_3\sin\theta_4) \\
& + ml^2\ddot{\theta}_5\left(\frac{1}{2}\sin\theta_3\sin\theta_5 + \cos\theta_3\cos\theta_5\right) \\
& + ml^2\dot{\theta}_5^2\left(\frac{1}{2}\cos\theta_5\sin\theta_3 - \sin\theta_5\cos\theta_3\right) \\
& - m\dot{\theta}_3l^2\dot{\theta}_5\sin\theta_3\cos\theta_5 - 5ml^2\dot{\theta}_3^2\cos\theta_3\sin\theta_3
\end{aligned} \tag{5.83}$$

$$\begin{aligned}
\tau_5 = & \frac{ml^2}{3}\ddot{\theta}_5 + \frac{1}{2}\ddot{\theta}_4ml^2\cos(\theta_4 - \theta_5) - \frac{1}{2}\dot{\theta}_4ml^2(\dot{\theta}_4 - \dot{\theta}_5)\sin(\theta_4 - \theta_5) \\
& + ml^2\ddot{\theta}_3\left(\frac{1}{2}\sin\theta_3\sin\theta_5 + \cos\theta_3\cos\theta_5\right) - \frac{1}{2}\dot{\theta}_3ml^2\sin(\theta_3 \\
& + \theta_5) + \frac{1}{2}m\dot{\theta}_4l^2\dot{\theta}_5\sin(\theta_5 - \theta_4) - \frac{1}{2}m\dot{\theta}_3l^2\dot{\theta}_5\sin\theta_3\cos\theta_5 \\
& + m\dot{\theta}_3l^2\dot{\theta}_5\sin\theta_5\cos\theta_3 - \frac{1}{2}mlg\cos\theta_5
\end{aligned} \tag{5.84}$$

For the four bar rhombus configuration, the Lagrangian equation of motion is:

$$\begin{bmatrix} \tau_1 \\ \tau_2 \\ \tau_3 \\ \tau_4 \\ \tau_5 \\ \tau_6 \end{bmatrix} = \begin{bmatrix} M_{11} & M_{12} & 0 & 0 & 0 & M_{16} \\ M_{21} & M_{22} & 0 & 0 & 0 & M_{26} \\ 0 & 0 & M_{33} & M_{34} & M_{35} & 0 \\ 0 & 0 & M_{43} & M_{44} & M_{45} & 0 \\ 0 & 0 & M_{53} & M_{54} & M_{55} & 0 \\ M_{61} & M_{62} & 0 & 0 & 0 & M_{66} \end{bmatrix} \begin{bmatrix} \ddot{\theta}_1 \\ \ddot{\theta}_2 \\ \ddot{\theta}_3 \\ \ddot{\theta}_4 \\ \ddot{\theta}_5 \\ \ddot{\theta}_6 \end{bmatrix} + \begin{bmatrix} N_{11} \\ N_{21} \\ N_{31} \\ N_{41} \\ N_{51} \\ N_{61} \end{bmatrix} + \begin{bmatrix} -\frac{1}{2}mlg\cos(\theta_1) \\ 0 \\ 0 \\ \frac{1}{2}mlg\cos(\theta_4) \\ -\frac{1}{2}mlg\cos(\theta_5) \\ -\frac{1}{2}mlg\cos(\theta_6) \end{bmatrix} \quad (5.85)$$

Here, mass matrix components are:

$$M_{11} = M_{44} = \frac{10 ml^2}{3} \text{ and } M_{55} = M_{66} = \frac{ml^2}{3}$$

$$M_{12} = M_{21} = ml^2(4 \cos \theta_1 \cos \theta_2 + \sin \theta_1 \sin \theta_2)$$

$$M_{16} = M_{61} = \frac{1}{2}ml^2 \cos (\theta_1 - \theta_6)$$

$$M_{22} = ml^2(6\cos^2 (\theta_2) + \sin^2 (\theta_2) + \frac{2}{3})$$

$$M_{26} = M_{62} = ml^2(\frac{1}{2} \sin \theta_2 \sin \theta_6 + \cos \theta_2 \cos \theta_6)$$

$$M_{33} = ml^2(6\cos^2 (\theta_3) + \sin^2 (\theta_3) + \frac{2}{3})$$

$$M_{34} = M_{43} = ml^2(4 \cos \theta_4 \cos \theta_3 + \sin \theta_4 \sin \theta_3)$$

$$M_{35} = M_{53} = ml^2\left(\frac{1}{2} \sin \theta_3 \sin \theta_5 + \cos \theta_3 \cos \theta_5\right)$$

$$M_{45} = M_{54} = \frac{1}{2} ml^2 \cos (\theta_4 - \theta_5)$$

Nonlinear matrix terms are:

$$\begin{aligned} N_{11} = & -4ml^2\dot{\theta}_2^2 \cos \theta_1 \sin \theta_2 - \frac{1}{2}\dot{\theta}_6 ml^2(\dot{\theta}_1 - \dot{\theta}_6) \sin (\theta_1 - \theta_6) \\ & + ml^2\dot{\theta}_2^2 \sin \theta_1 \cos \theta_2 + \frac{1}{2}\dot{\theta}_6 \dot{\theta}_1 ml^2 \sin (\theta_1 - \theta_6) \end{aligned}$$

$$\begin{aligned} N_{21} = & -10ml^2\dot{\theta}_2 \cos \theta_2 \sin \theta_2 + ml^2\dot{\theta}_1^2 (\cos \theta_1 \sin \theta_2 - 4 \cos \theta_2 \sin \theta_1) \\ & + ml^2\dot{\theta}_6^2 \left(\frac{1}{2} \cos \theta_6 \sin \theta_2 - \sin \theta_6 \cos \theta_2\right) - m\dot{\theta}_2 l^2 \dot{\theta}_6 \sin \theta_2 \cos \theta_6 \\ & - 5ml^2\dot{\theta}_2^2 \cos \theta_2 \sin \theta_2 \end{aligned}$$

$$\begin{aligned} N_{31} = & -10ml^2\dot{\theta}_3 \cos \theta_3 \sin \theta_3 + ml^2\dot{\theta}_4^2 (\cos \theta_4 \sin \theta_3 - 4 \cos \theta_3 \sin \theta_4) \\ & + ml^2\dot{\theta}_5^2 \left(\frac{1}{2} \cos \theta_5 \sin \theta_3 - \sin \theta_5 \cos \theta_3\right) - m\dot{\theta}_3 l^2 \dot{\theta}_5 \sin \theta_3 \cos \theta_5 \\ & - 5ml^2\dot{\theta}_3^2 \cos \theta_3 \sin \theta_3 \end{aligned}$$

$$\begin{aligned} N_{41} = & -4ml^2\dot{\theta}_3^2 \cos \theta_4 \sin \theta_3 - \frac{1}{2}\dot{\theta}_5 ml^2(\dot{\theta}_4 - \dot{\theta}_5) \sin (\theta_4 - \theta_5) \\ & + ml^2\dot{\theta}_3^2 \sin \theta_4 \cos \theta_3 + \frac{1}{2}\dot{\theta}_4 \dot{\theta}_5 ml^2 \sin (\theta_4 - \theta_5) \end{aligned}$$

$$\begin{aligned} N_{51} = & -\frac{1}{2}\dot{\theta}_4 ml^2(\dot{\theta}_4 - \dot{\theta}_5) \sin (\theta_4 - \theta_5) - \frac{1}{2}\dot{\theta}_3 ml^2 \sin (\theta_3 + \theta_5) \\ & + \frac{1}{2} m\dot{\theta}_4 l^2 \dot{\theta}_5 \sin (\theta_5 - \theta_4) - \frac{1}{2} m\dot{\theta}_3 l^2 \dot{\theta}_5 \sin \theta_3 \cos \theta_5 \\ & + m\dot{\theta}_3 l^2 \dot{\theta}_5 \sin \theta_5 \cos \theta_3 \end{aligned}$$

$$\begin{aligned}
N_{61} = & -\frac{1}{2}\dot{\theta}_1 ml^2(\dot{\theta}_1 - \dot{\theta}_6)\sin(\theta_1 - \theta_6) - \frac{1}{2}\dot{\theta}_2 ml^2\sin(\theta_2 + \theta_6) \\
& + \frac{1}{2} m\dot{\theta}_1 l^2 \dot{\theta}_6 \sin(\theta_6 - \theta_1) - \frac{1}{2} m\dot{\theta}_2 l^2 \dot{\theta}_6 \sin \theta_2 \cos \theta_6 \\
& + m\dot{\theta}_2 l^2 \dot{\theta}_6 \sin \theta_6 \cos \theta_2
\end{aligned}$$

For backward motion of the end effector, only the gravity matrix will change. The others will remain the same. Gravity matrix for backward movement:

$$G = \begin{bmatrix} \frac{1}{2} mlg\cos(\theta_1) \\ 0 \\ 0 \\ -\frac{1}{2} mlg\cos(\theta_4) \\ \frac{1}{2} mlg\cos(\theta_5) \\ \frac{1}{2} mlg\cos(\theta_6) \end{bmatrix} \quad (5.86)$$

5.4 Discussions

Following the same step, we can formulate the Lagrangian dynamic equations for a large number of networks. But, from the detailed analysis, we can see that as the rhombus network increases, the conventional Lagrangian approach becomes much more difficult and without computer simulation it is very hard to handle such computational complexity. That is why bond graph has been used to create dynamic analysis for more than two networks.

Chapter 6

Bond Graph Dynamic Analysis of the Actuator

6.1 Introduction

This chapter provides the detailed dynamic simulation of the newly designed actuator for different network combinations, using the bond graph analysis. Bond graph provides great flexibility for dynamic modeling with the inclusion of control. Simulation has been done for horizontal and vertical movement of the end effector, to identify the effect of gravity on the actuator performance. Simulation graphs gives a clear idea about dynamic behaviour (position, velocity, acceleration etc.) and motor torque requirement of the actuator for different networks.

6.2 Bond Graph Modeling

Bond graph provides a graphical representation of a physical dynamic system. For bond graph modeling of a dynamic system, first we need to identify the components of the model and then need to develop their individual model. Proper connection between the components will give us the dynamic model of the system. There are several components in the newly designed linear actuator model:

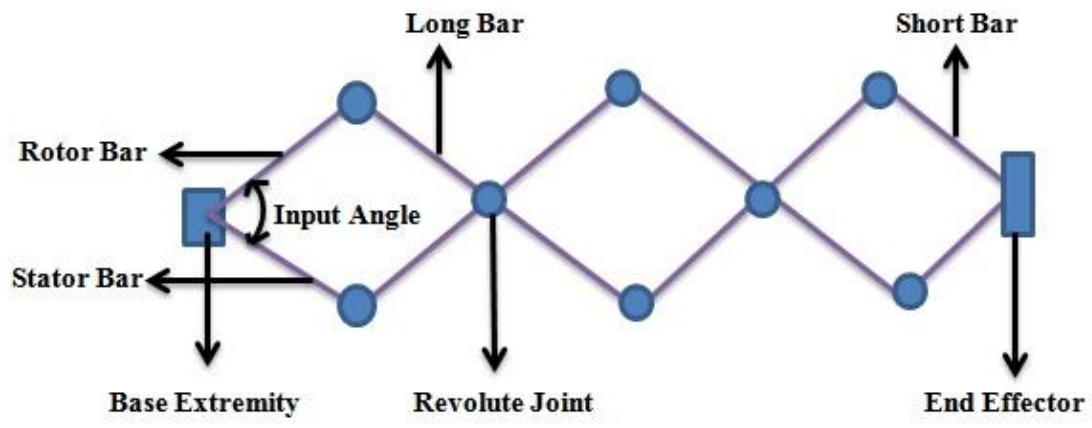
1. Links
2. Joints
3. Motor model
4. Motor gear modeling
5. Control mechanism
6. Torque transmission system
7. End effector modeling

Among these, detailed modeling procedures for the links, joints, and motor with gear box have already been described in the scissor lift chapter (Chapter 3).

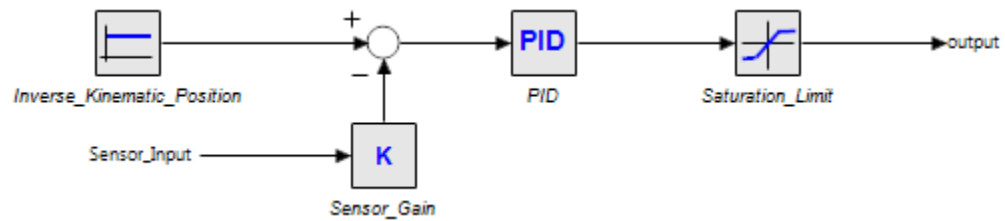
6.2.1 Control Mechanism

One PID controller is used to control the mechanism motor but not the mechanism end effector. Here, we are controlling the input angle of the mechanism (Figure 6.1 (a)). For a desired position of the end effector, input angle can be calculated from the kinematic relationship (inverse kinematic model). This angle is the desired angle for the actuator. Angle between the motor rotor and stator link gives the present angle.

Difference between the two angles will give the error term and it will be fed into the PID controller input. Then controller drives the mechanism to its required position based on the command input. Limit block is there to protect the motor from overlimit voltage command. Figure 6.1 (b) shows the bond graph control schematic for the actuator.



(a)



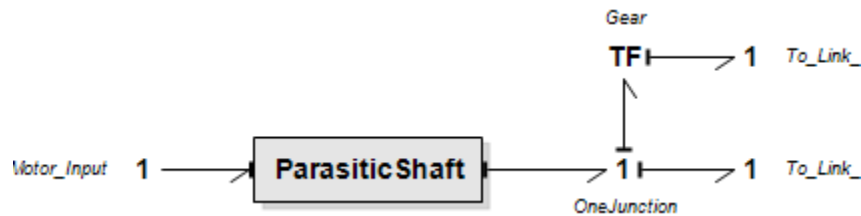
(b)

Figure 6.1 (a) Input angle of the actuator (Network # 3) (b) Bond Graph Control

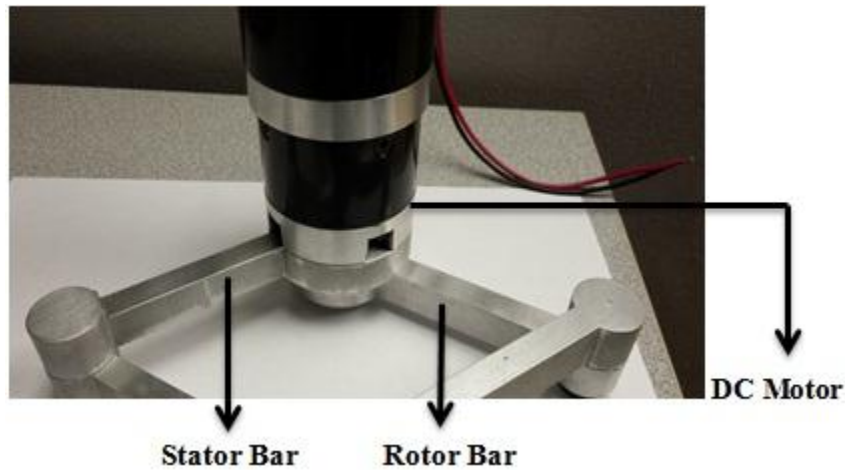
Schematic

6.2.2 Torque Transmission System

In the physical system, the motor stator is connected to a bar and the rotor shaft is connected to the other bar on the base extremity. When the rotor shaft rotates the rotor bar, due to reaction force the stator bar will move in the opposite direction from the application of the third law of Newton (action-reaction). To model this phenomena, a gear is used. In the model, motor torque directly goes to the rotor bar and the stator bar is connected through a transformer with a gear ratio of 1.



(a)



(b)

Figure 6.2 Torque transmission system schematic: (a) Bond Graph (b) Physical Model

6.3 End Effector Loading

To model the end effector loading, an inertia (I) element is used. It is connected with the system through parasitic stiffness and damping. Figure 6.3 shows the end effector load simulation.

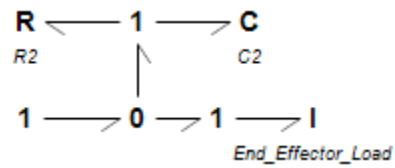


Figure 6.3 End Effector Load Simulation

6.4 Simulation

Simulation has been done for horizontal and vertical movement of the end effector. For horizontal movement, end effector load (I parameter) was connected in the X axis direction and for vertical movement it was in the Y axis direction.

6.4.1 Simulation Properties

Initial height was 0.17 m and the desired height was 0.77m. So, the desired end effector movement is 0.6m. Mass properties of the links are calculated using Solidworks. Aluminium alloy (Al 7075) has been used as the material. Maxon motor (Model # 167131) is chosen with maxon gearhead (model # 110408). Motor specifications are already mentioned in the scissor lift chapter. End effector loading was 0.05 kg. Initial position is calculated using the maximum input angle from kinematics. Similarly, minimum input angle gives the maximum movement position of the end effector. To calculate the maximum and minimum input angle, link dimensions (e.g. width, length etc.) and network numbers are the most important. There is an inverse relationship between the end effector position and input angle of the actuator. Increase in the input angle results in a decrease of the end effector position. So, in the controller gain parameter proportional gain is negative. PID controller tuning was performed through trial and error method, since the goal of the work is to provide for a proof-of-concept leaving the PID optimization to the users. Table 6.1 shows the PID controller gain for simulation. Link length varies with the network number, but the cross sectional areas of the links remain the same.

6.4.2 Simulation Parameters

Simulation was performed for five network combinations ($n = 1,2,3,4,5$). Each of the case position, velocity and acceleration of the end effector was simulated. To show the simulation outcome for each of the case, the system schematic is presented first, followed by the 3D schematic and dynamic behavior of the system.

Table 6.1 Simulation Properties

Position of the End Effector	Vertical Movement	Horizontal Movement
Initial Position = 0.17 m	Proportional gain $k_p = -1.0 \{ \}$;	Proportional gain $k_p = -1.3 \{ \}$;
Desired Position = 0.77 m	Derivative time constant $\tau_D = 0.5 \{s\}$;	Derivative time constant $\tau_D = 0.5 \{s\}$;
End Effector Loading = 0.05 Kg	Tameness constant $\beta = 0.09 \{ \}$;	Tameness constant $\beta = 0.09 \{ \}$;
	Integral time constant $\tau_I = 1.0 \{s\}$;	Integral time constant $\tau_I = 1.0 \{s\}$;

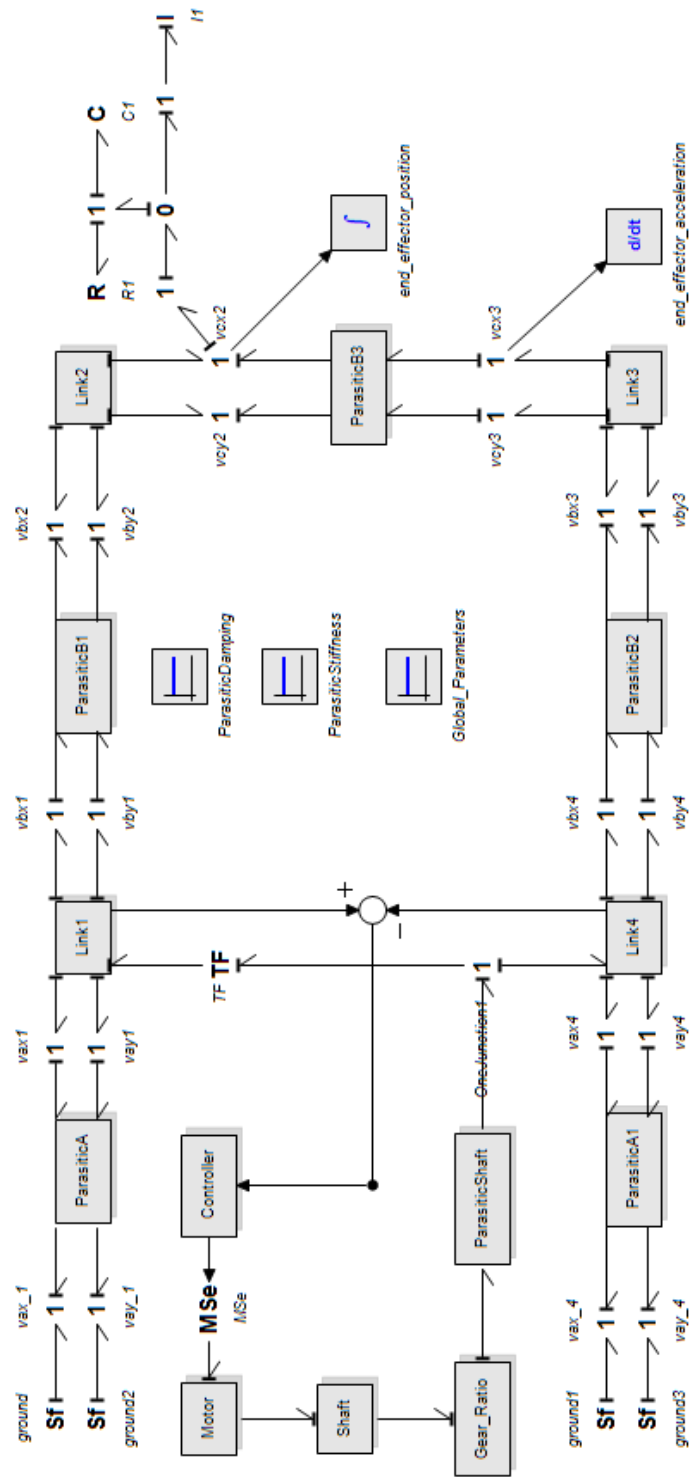
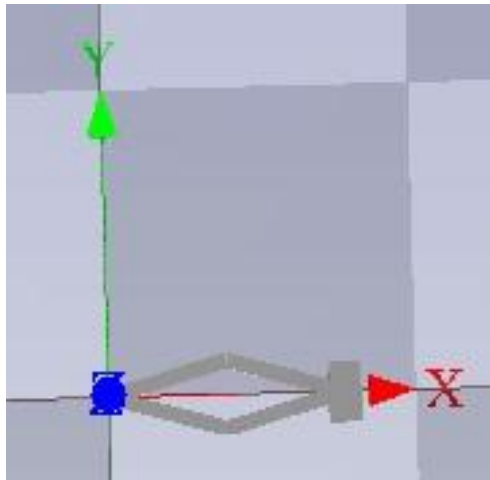
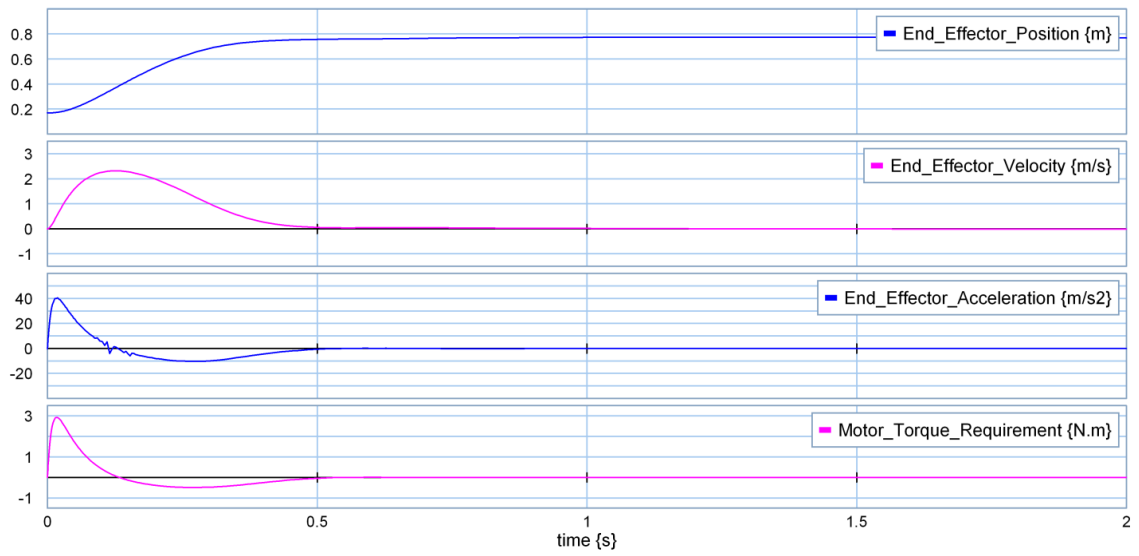


Figure 6.4 Bond Graph Schematic of the system (Network # 1: Horizontal)



(a)



(b)

Figure 6.5 Simulation graphs of the system (Network # 1: Horizontal) (a) 3D Schematic

(b) Dynamic Behavior

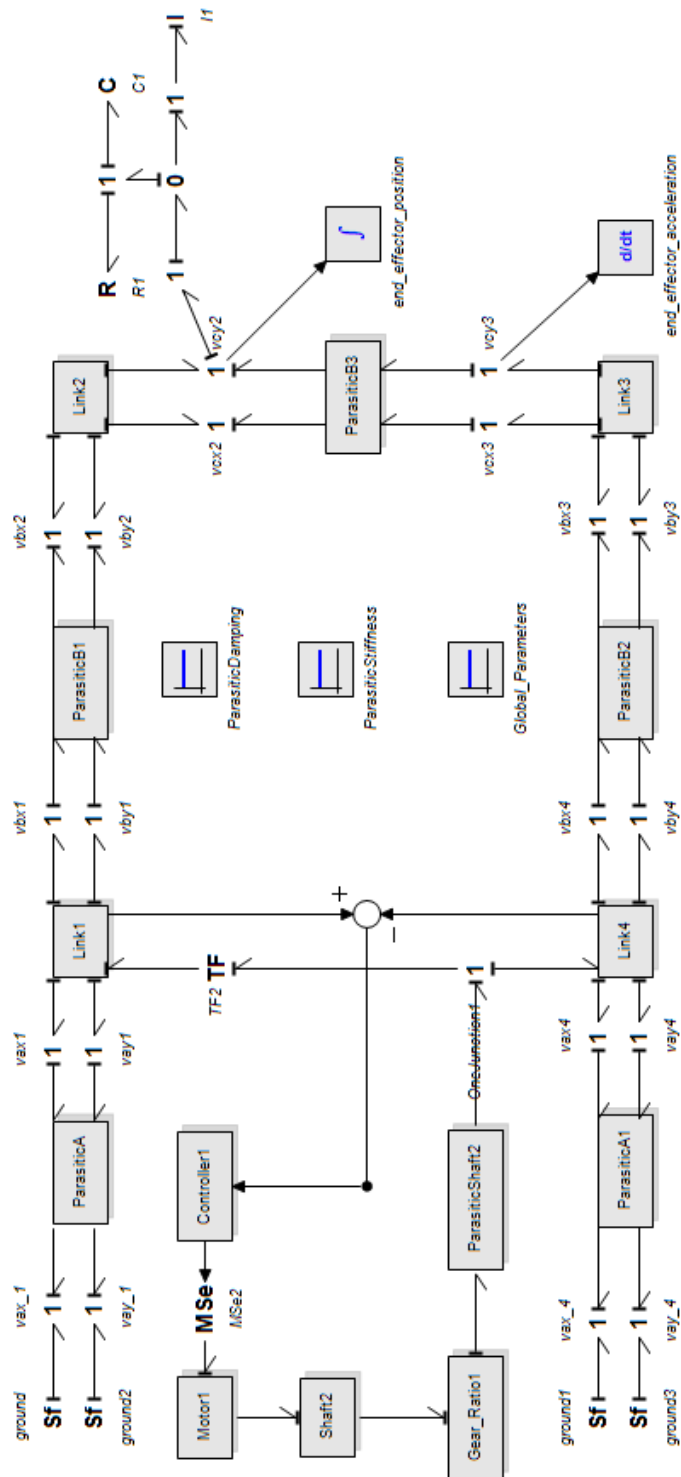
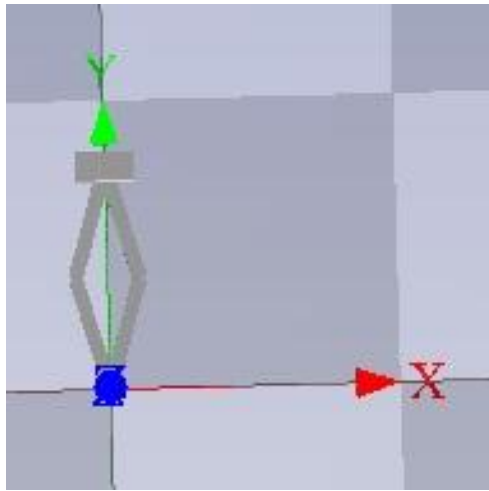
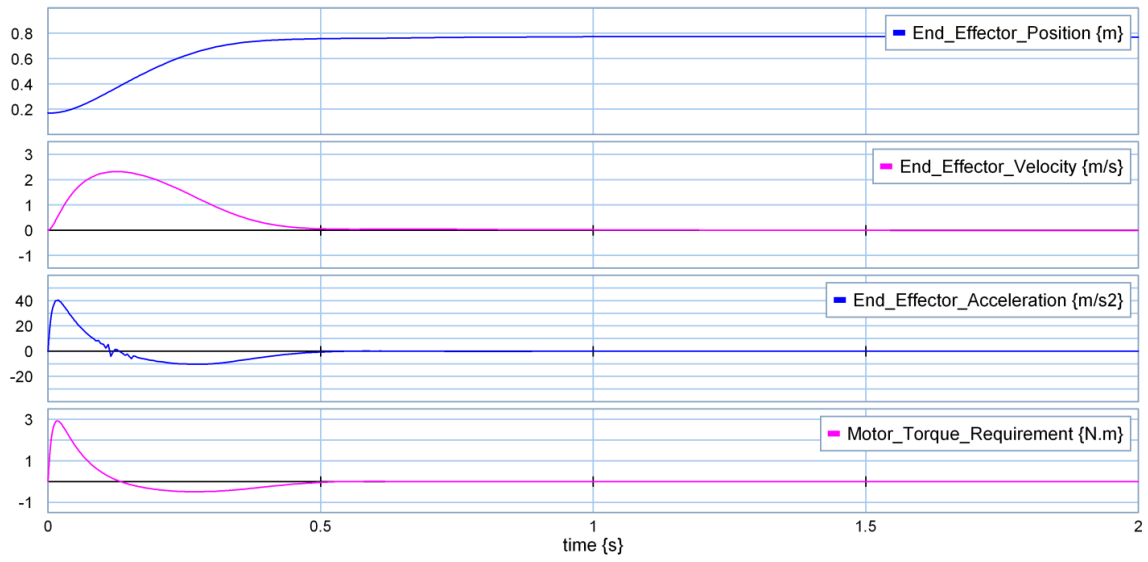


Figure 6.6 Bond Graph Schematic of the system (Network # 1: Vertical)



(a)



(b)

Figure 6.7 Simulation graphs of the system (Network # 1: Vertical) (a) 3D Schematic (b) Dynamic Behavior

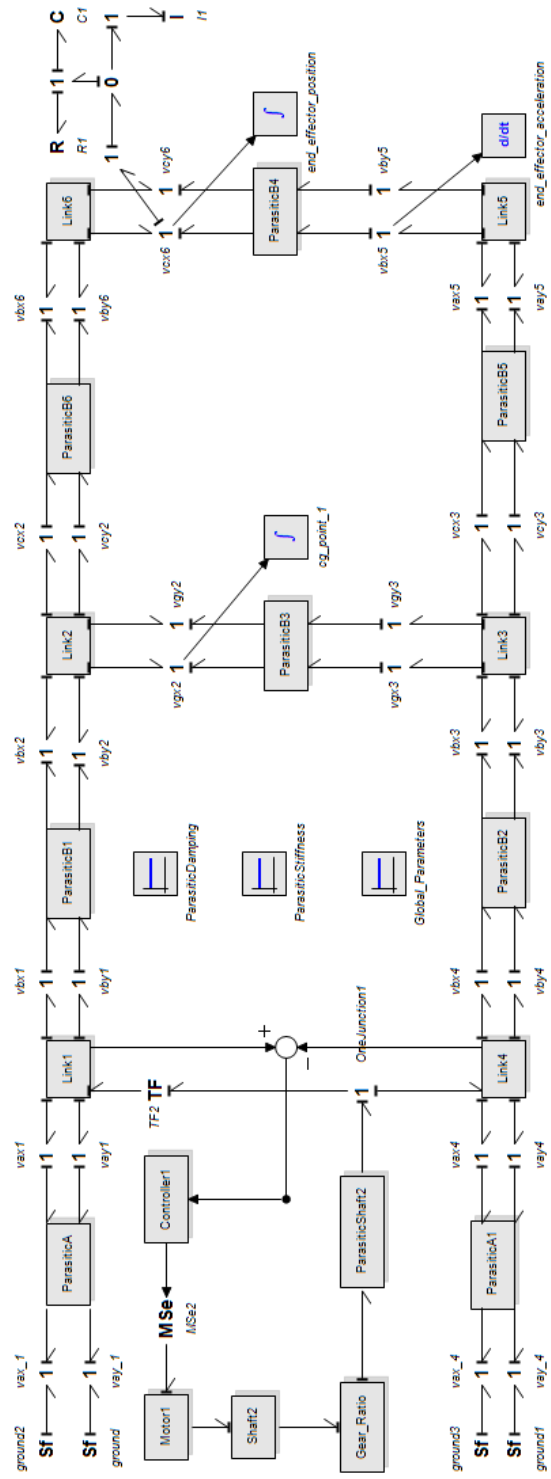
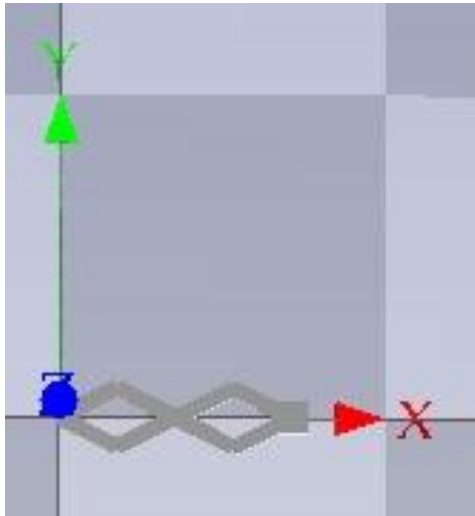
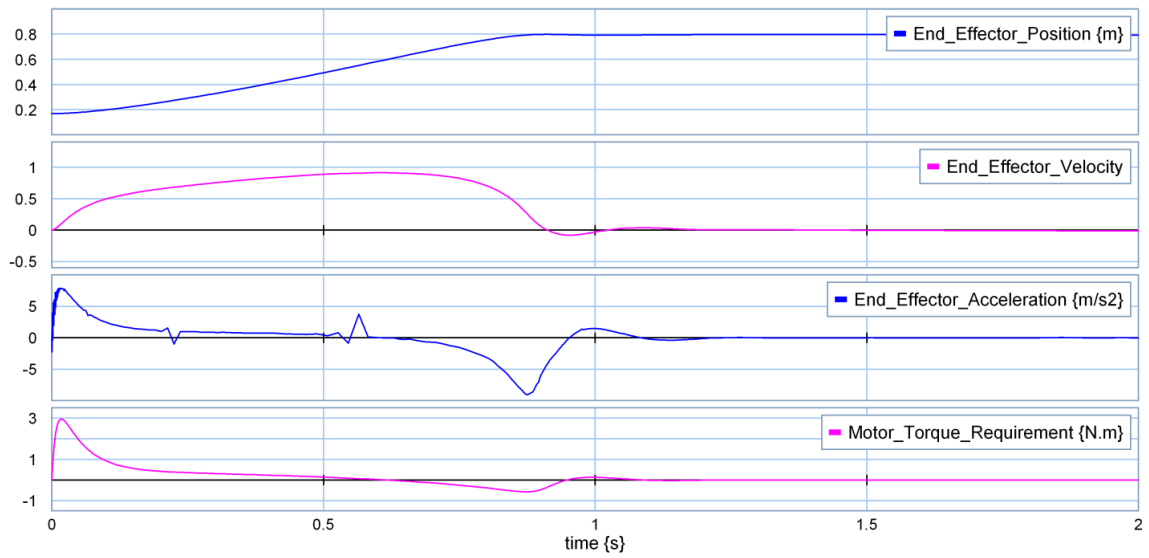


Figure 6.8 Bond Graph Schematic of the system (Network # 2: Horizontal)



(a)



(b)

Figure 6.9 Simulation graphs of the system (Network # 2: Horizontal) (a) 3D Schematic
(b) Dynamic Behavior

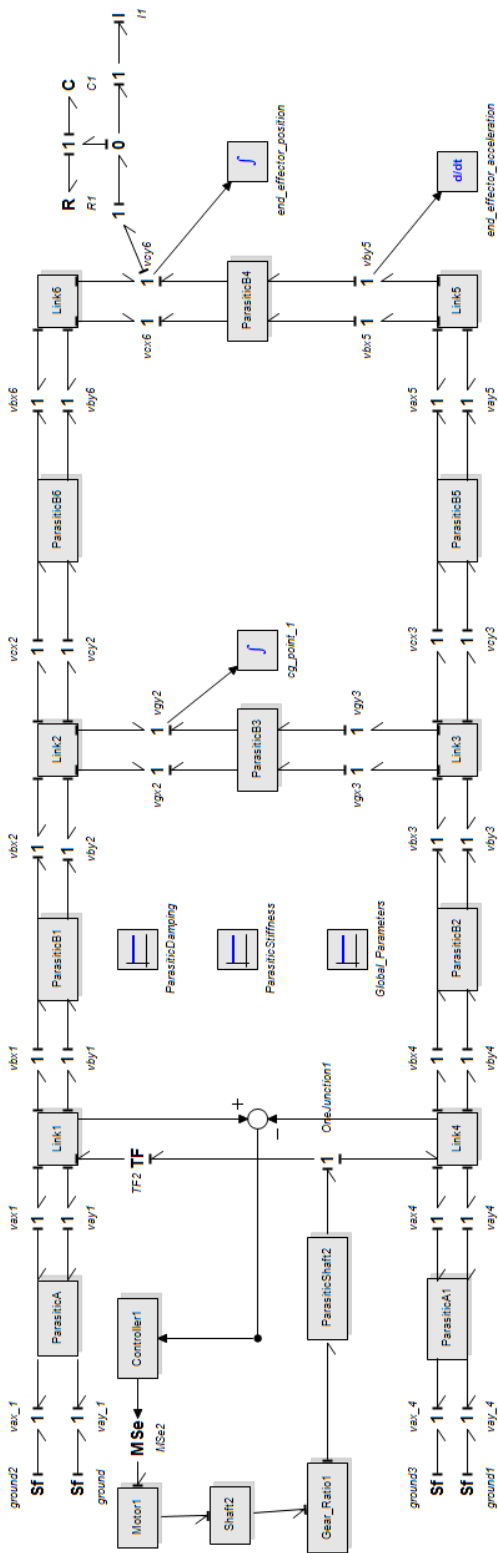
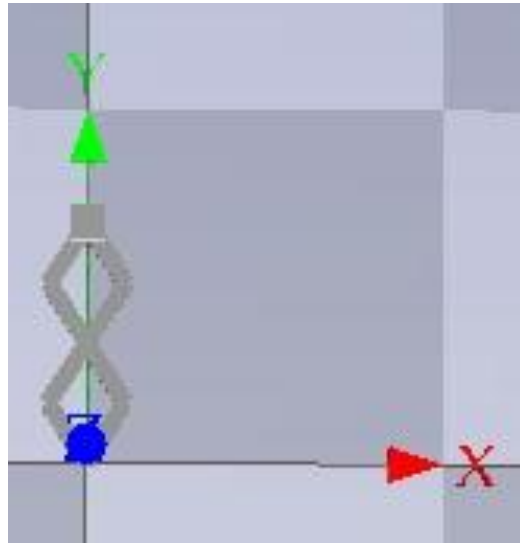
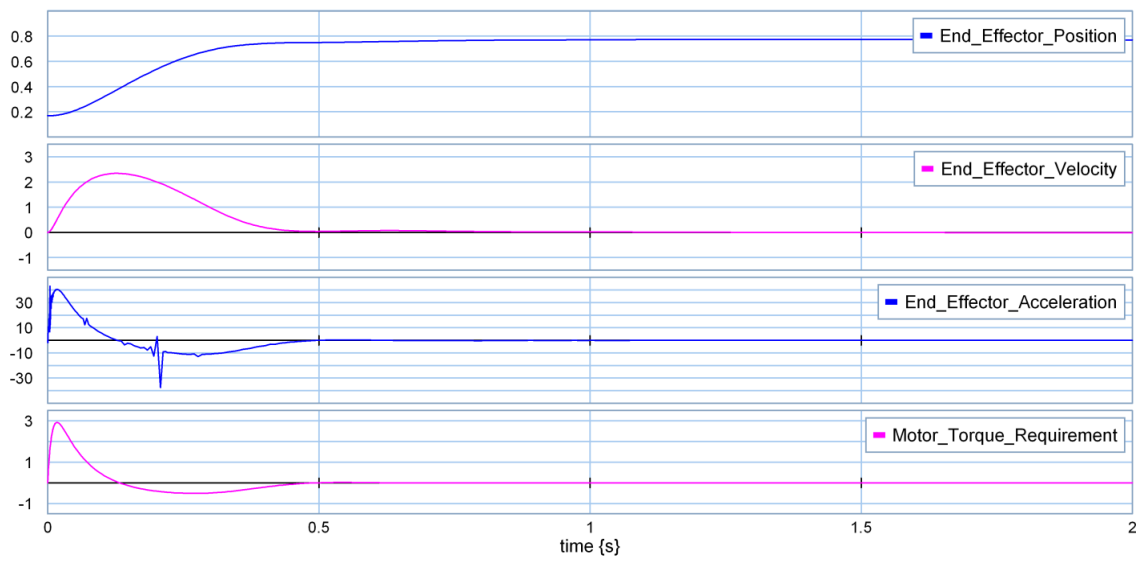


Figure 6.10 Bond Graph Schematic of the system (Network # 2: Vertical)



(a)



(b)

Figure 6.11 Simulation graphs of the system (Network # 2: Vertical) (a) 3D Schematic

(b) Dynamic Behavior

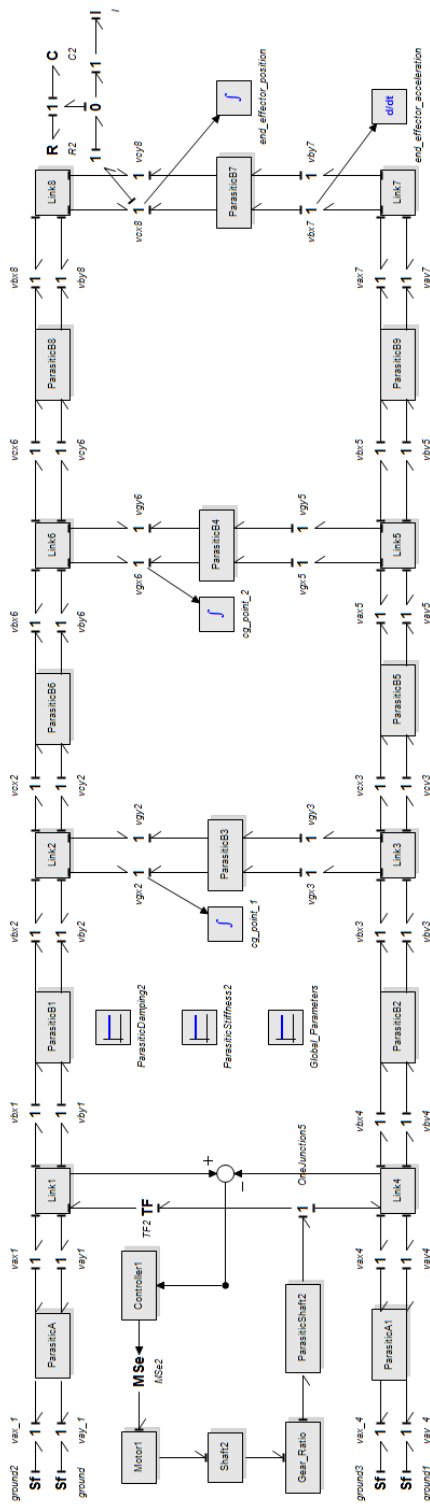
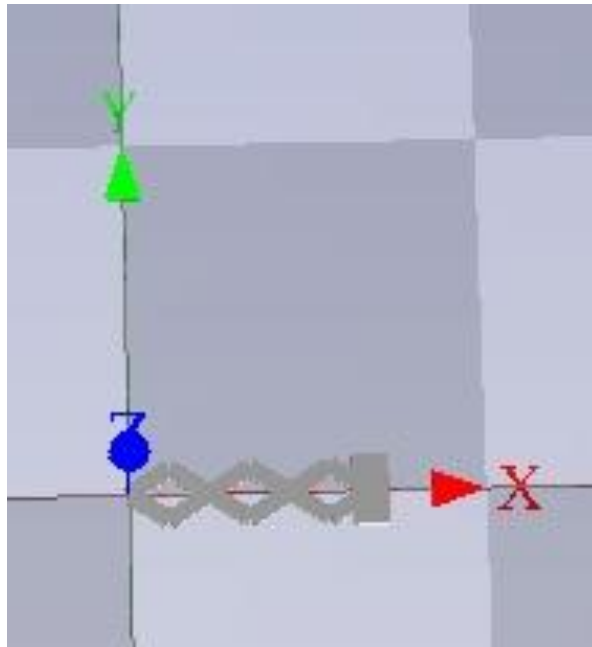
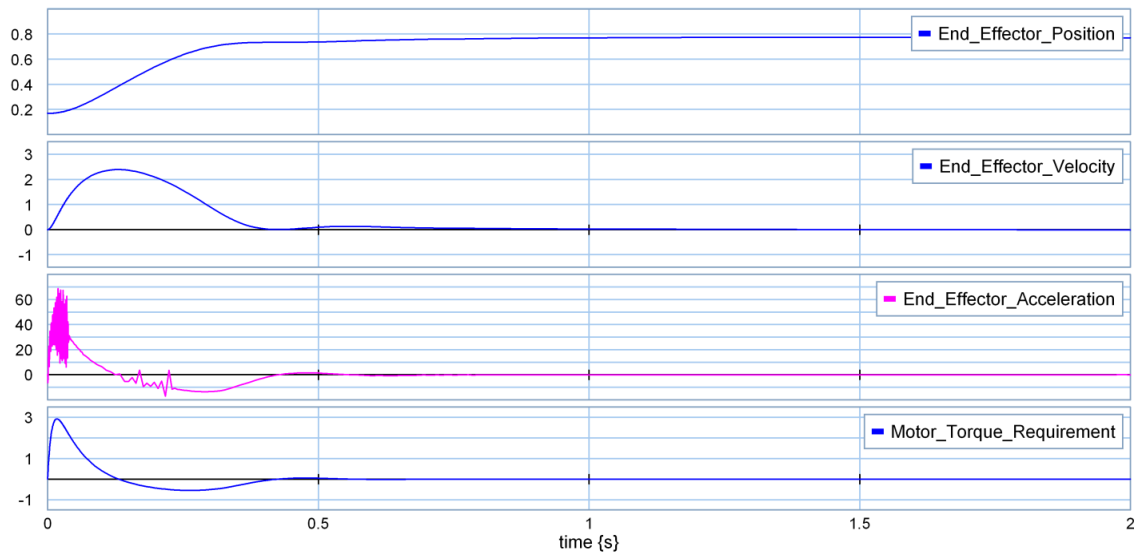


Figure 6.12 Bond Graph Schematic of the system (Network # 3: Horizontal)



(a)



(b)

Figure 6.13 Simulation graphs of the system (Network # 3: Horizontal) (a) 3D Schematic

(b) Dynamic Behavior

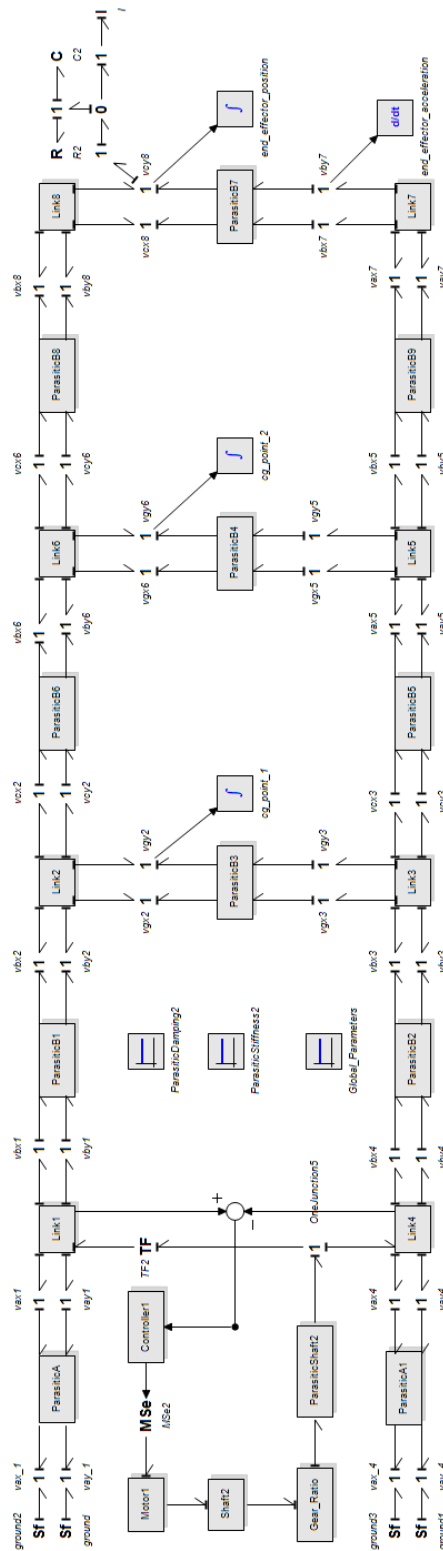
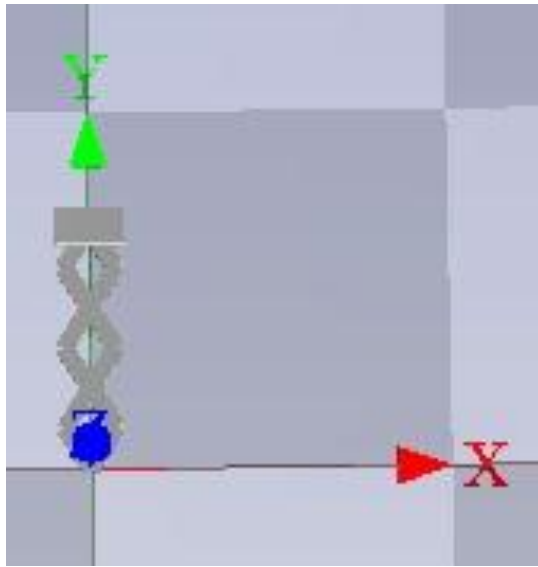
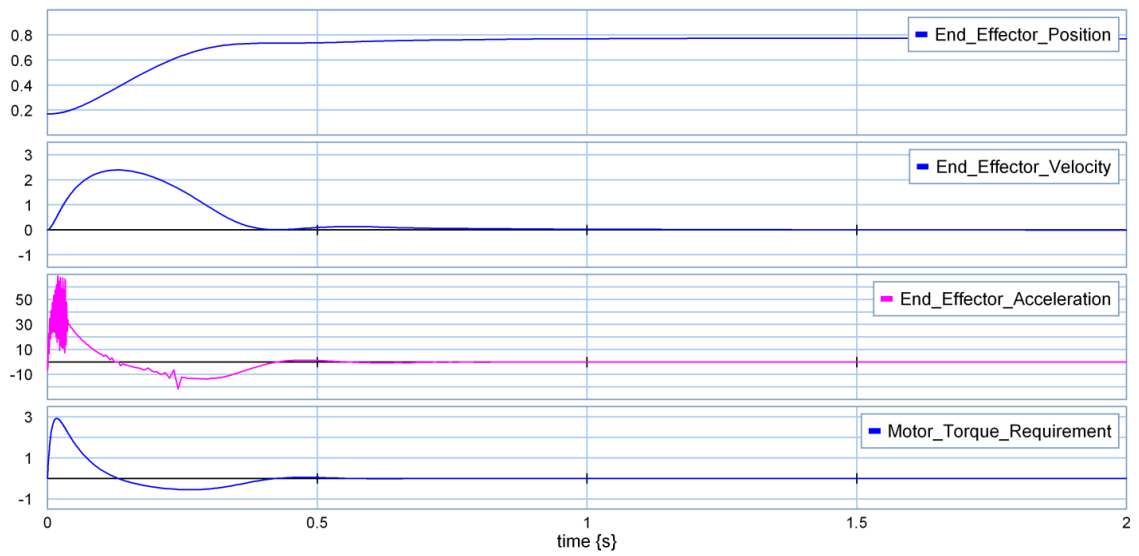


Figure 6.14 Bond Graph Schematic of the system (Network # 3: Vertical)



(a)



(b)

Figure 6.15 Simulation graphs of the system (Network # 3: Vertical) (a) 3D Schematic

(b) Dynamic Behavior

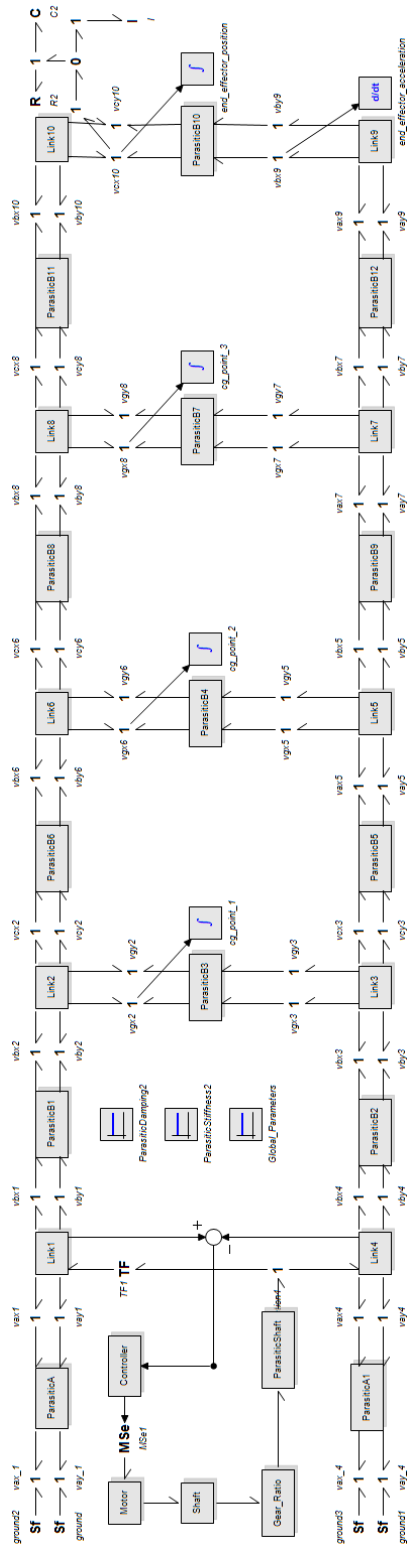
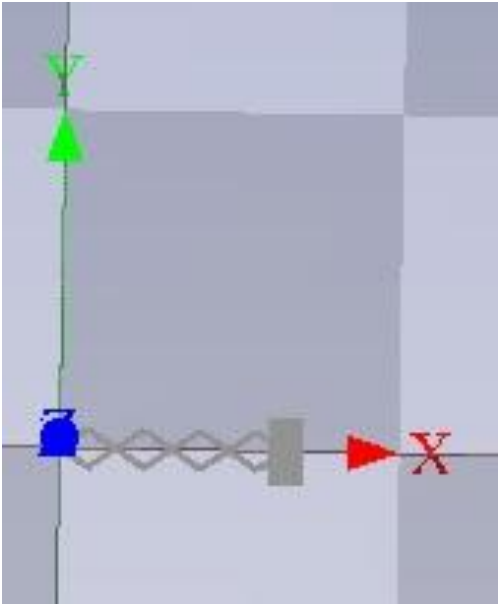
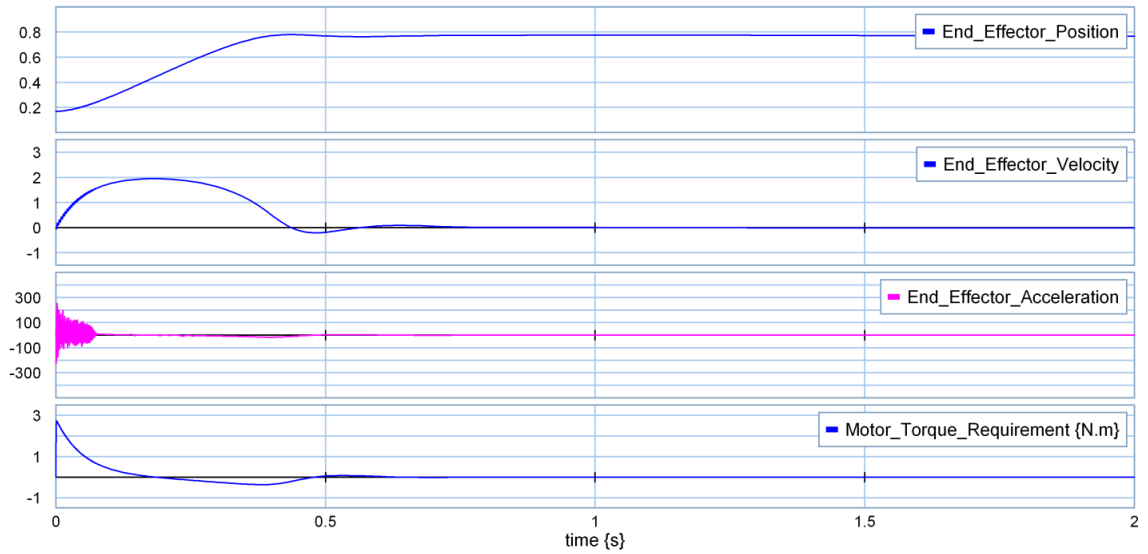


Figure 6.16 Bond Graph Schematic of the system (Network # 4: Horizontal)



(a)



(b)

Figure 6.17 Simulation graphs of the system (Network # 4: Horizontal) (a) 3D Schematic
(b) Dynamic Behavior

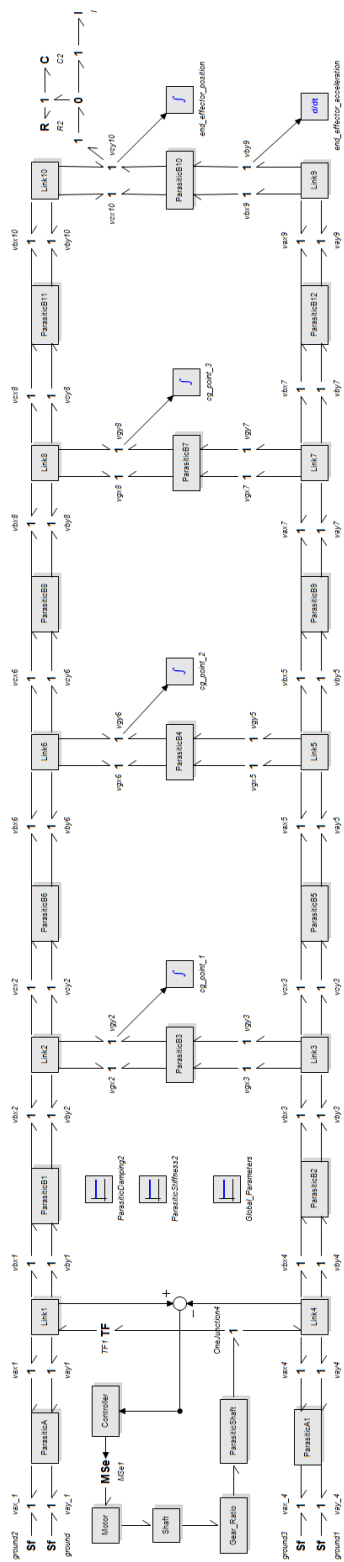
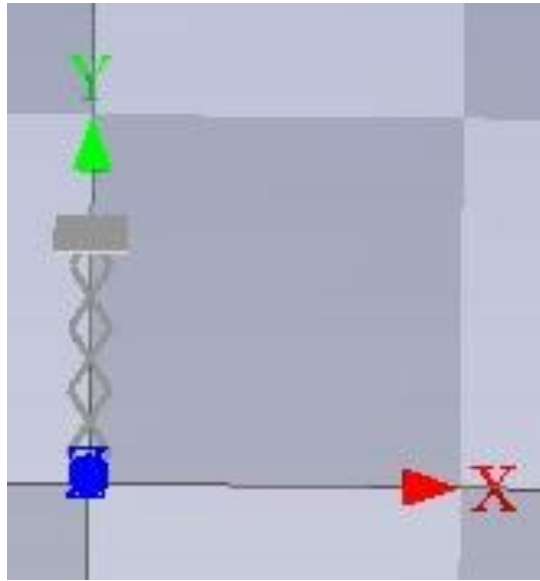
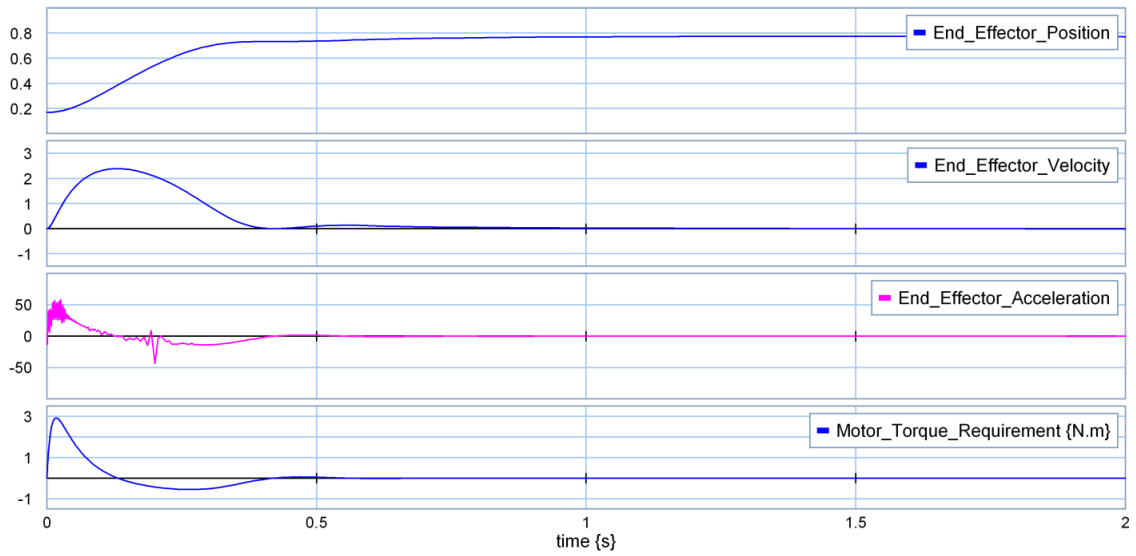


Figure 6.18 Bond Graph Schematic of the system (Network # 4: Vertical)



(a)



(b)

Figure 6.19 Simulation graphs of the system (Network # 4: Vertical) (a) 3D Schematic

(b) Dynamic Behavior

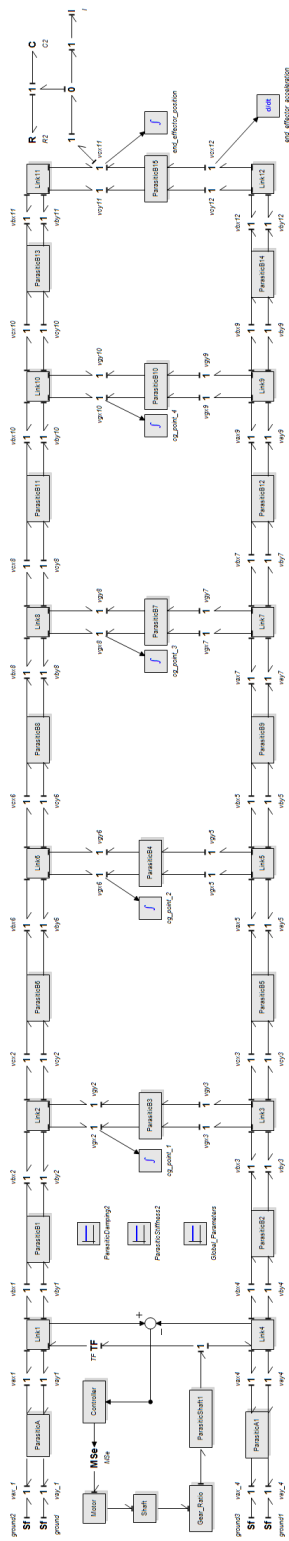
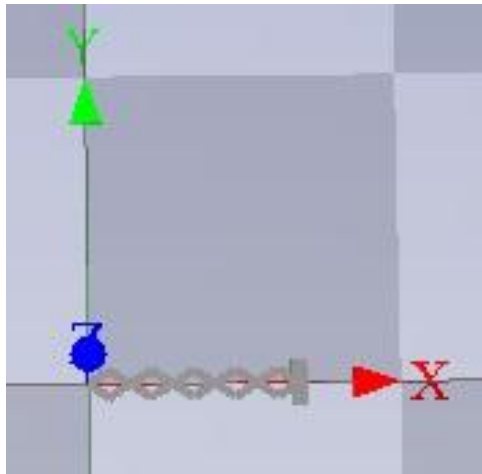
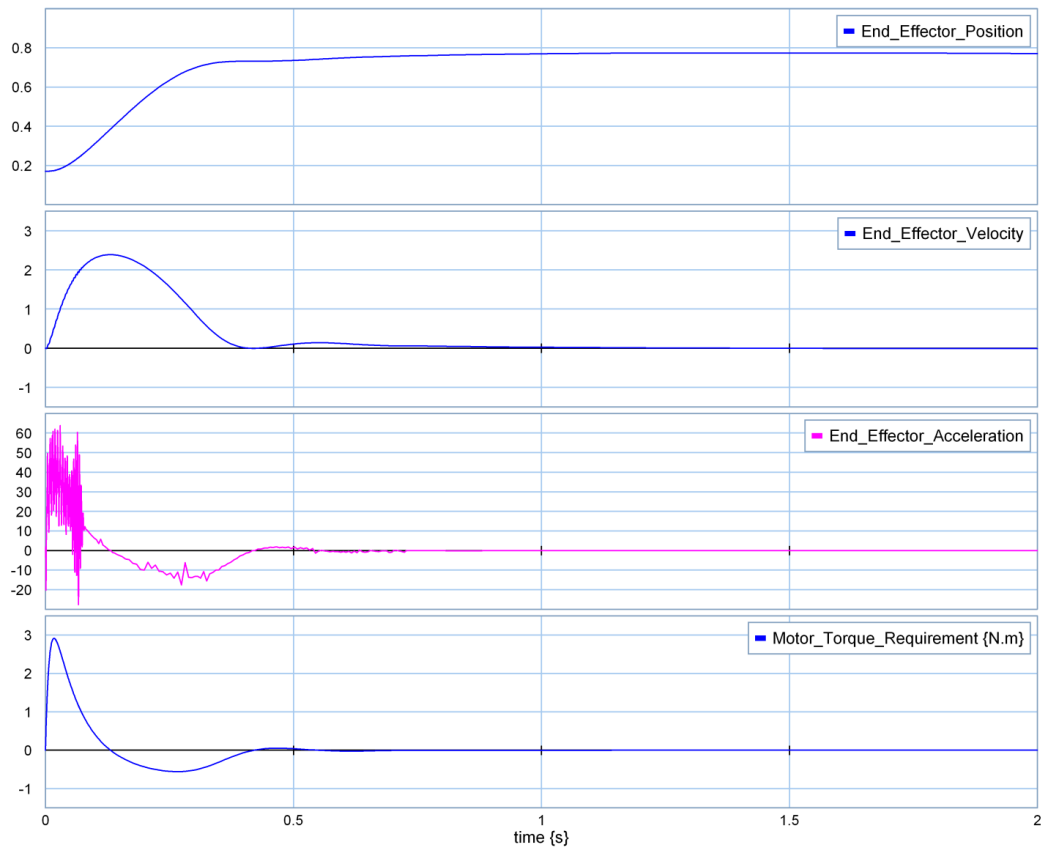


Figure 6.20 Bond Graph Schematic of the system (Network # 5: Horizontal)



(a)



(b)

Figure 6.21 Simulation graphs of the system (Network # 5: Horizontal) (a) 3D Schematic

(b) Dynamic Behavior

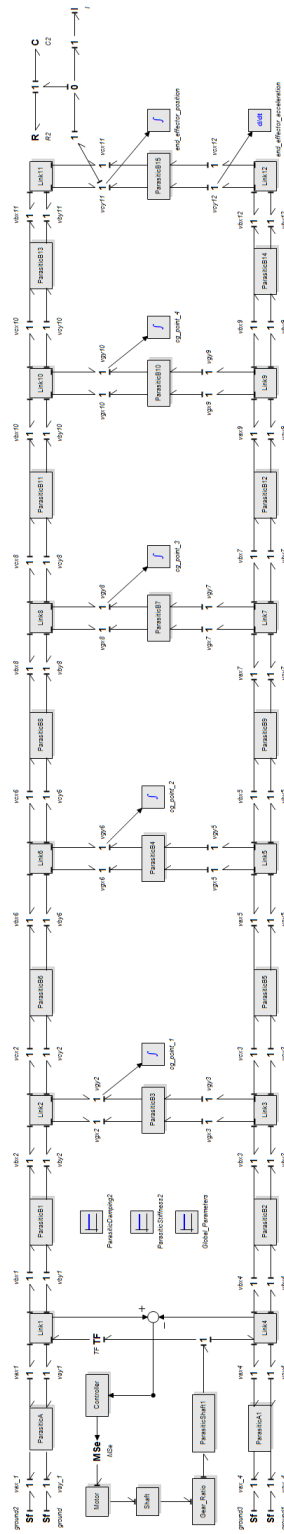
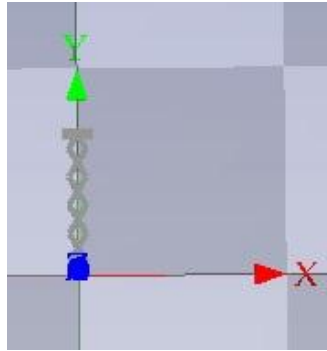
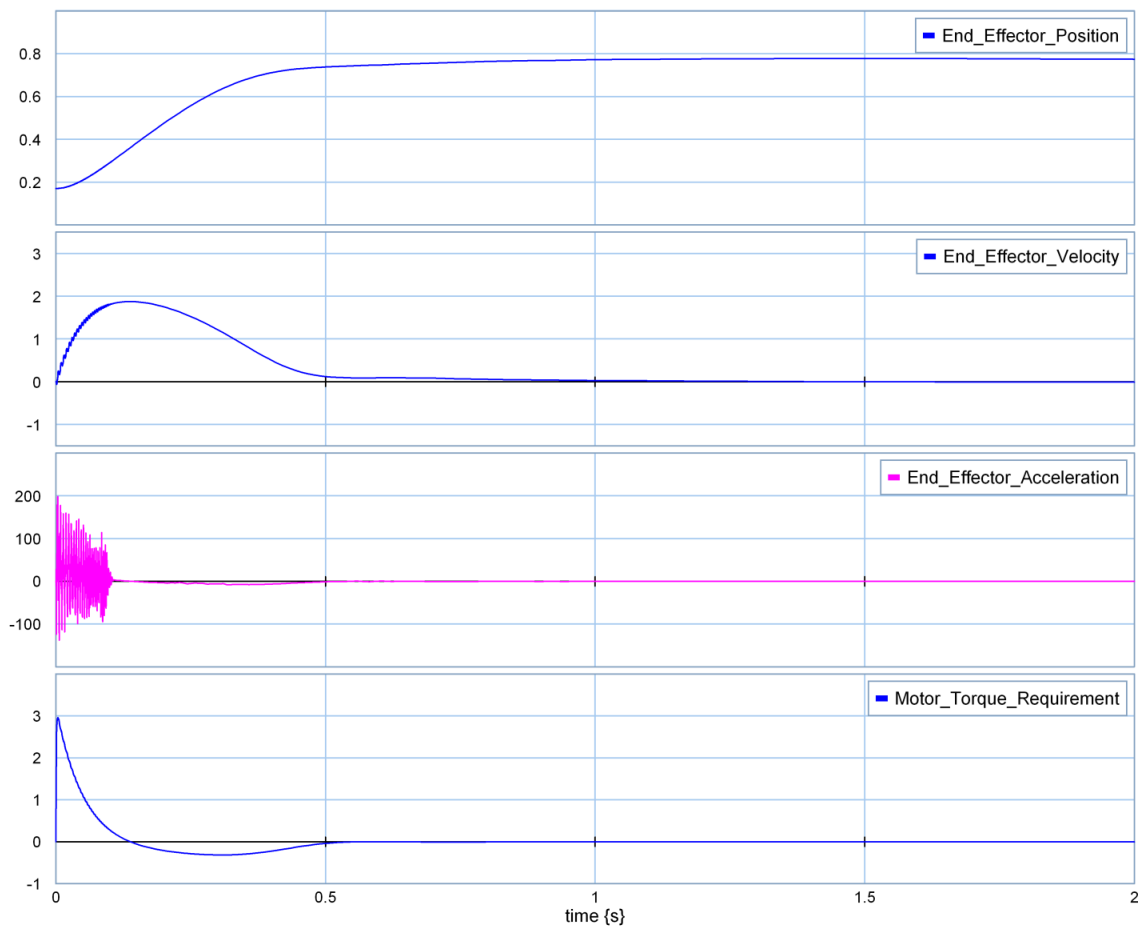


Figure 6.22 Bond Graph Schematic of the system (Network # 5: Vertical)



(a)



(b)

Figure 6.23 Simulation graphs of the system (Network # 5: Vertical) (a) 3D Schematic

(b) Dynamic Behavior

From the simulation data we can construct a table for the maximum values of the simulation parameters.

Table 6.2 Simulation Summary (Horizontal Simulation)

Simulation	Network 1	Network 2	Network 3	Network 4	Network 5
Short Link Length (m)	0.4	0.2	0.1333	0.1	0.08
Long Link Length (m)	-	0.4	0.2666	0.2	0.16
Maximum Velocity (m/s)	2.32	0.85	2.4	1.95	2.4
Maximum Acceleration (m/s ²)	40	8	70	240	65
Maximum Torque Requirement (Nm)	2.92	2.92	2.92	2.73	2.9
Torque Requirement Duration (S)	0.14	0.83	0.13	0.19	0.13

Table 6.3 Simulation Summary (Vertical Simulation)

Simulation	Network 1	Network 2	Network 3	Network 4	Network 5
Short Link Length (m)	0.4	0.2	0.1333	0.1	0.08
Long Link Length (m)	-	0.4	0.2666	0.2	0.16
Maximum Velocity (m/s)	2.32	2.34	2.4	2.4	1.87
Maximum Acceleration (m/s ²)	40	45	65	60	200
Maximum Torque Requirement (Nm)	2.92	2.92	2.9	2.92	2.93
Torque Requirement Duration (S)	0.13	0.14	0.13	0.13	0.14

6.5 Result Interpretation

Position, velocity and acceleration of the end effector are recorded for different network combinations. By keeping the maximum travel distance of the end effector equal, different network simulation shows different acceleration value with the same motor. From the simulation, we get a clear idea about the motor torque requirements. Torque varies from 2.7 Nm to 3 Nm.

6.6 Discussions

Dynamic simulation gives a clear idea about the performance of the different network combinations. During vertical simulation actuator needs to encounter the gravity force. So, the torque requirement is higher compared to the horizontal simulation. Though torque requirement doesn't varies that much, but the duration of torque supply from motor varies with different network. From the simulation, we can see that the network 4 configuration gives the maximum acceleration under horizontal operating condition for a certain linear distance while comparing with the other possible combinations. For practical design, we choose this operating condition for the actuator.

Chapter 7

Practical Design and Calculations

7.1 Introduction

A physical model of the newly designed actuator was built to validate the proof of concept. This chapter describes the SOLIDWORKS designs and associated calculations related to the production process. The actuator assembly consists of two major components: actuator part and base assembly. In the actuator part, there are motor stator bar, motor rotor bar, and bars with end effector connector. Between the motor and the end effector, the body of the actuator consists of long bars connected as a X by the shaft screws and bearings.

7.2 Bar Length Calculation

There are long and short bars in the actuator assembly. Length of the bar depends on the networking number of the rhombus and desired stroke length. It is very important to calculate the proper bar length for a particular number of network, to get adequate functionality of the actuator. For all the bars, the cross sectional area will remain equal. If the end effector stroke length is H and the number of network is n , then the short link length would be:

$$L_S = \frac{H}{2n} \quad (7.1)$$

For the rhombus configuration, length of a long bar is equal to the interjoint distance between two consecutive central moving joints. So, length between the joint center is:

$$L_l = 2 * L_S \quad (7.2)$$

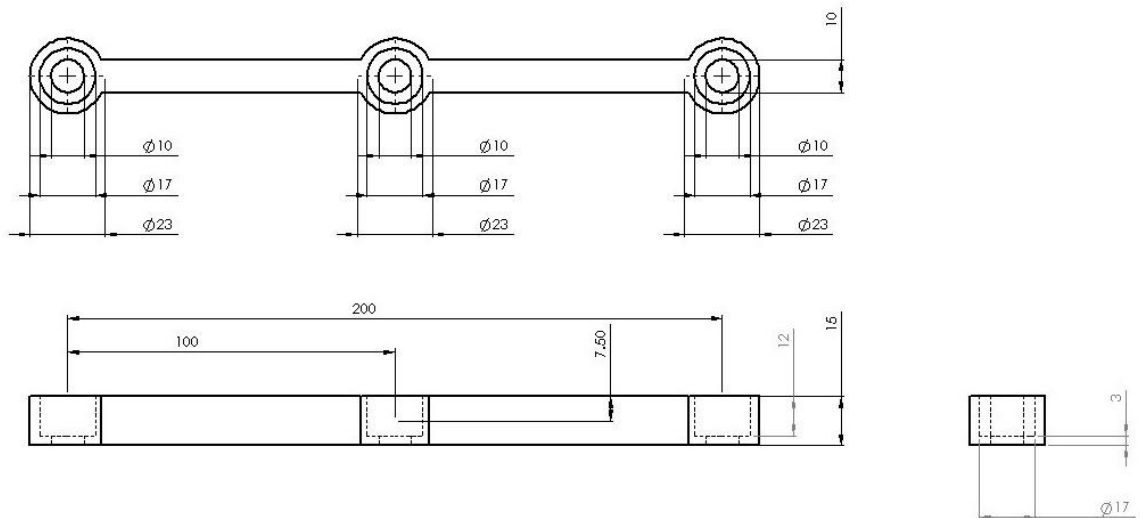


Figure 7.1 Long Bar with Dimensions (cm)

From the Bond Graph dynamic simulation, we have seen that network number four gives the best performance in horizontal operating condition. For the practical design, the 4 rhombus network model was chosen with a maximum end effector movement of 0.8m. Using Eq. (7.1), calculated short link length is 0.1 m. and long bar length is 0.2 m. Figure 7.1 shows a long bar for our designed actuator, where all the dimensions are measured in centimeter (cm).

7.3 Workspace and Encumbrance Calculation

From kinematic formulation (Chapter 4), we can calculate the workspace and encumbrance for the network 4 rhombus configuration based linear actuator. For a bar width of 0.01 m, the minimum position of the end effector would be:

$$x_{min} = 4 * 2 * 0.1 \sin \left(2 \arccos \left(\frac{0.01}{0.1} \right) \right) = 0.16 \text{ m} \quad (7.3)$$

Maximum position of the end effector:

$$x_{max} = 4 * 2 * 0.1 \cos \left(2 \arcsin \left(\frac{0.01}{0.1} \right) \right) = 0.784 \text{ m} \quad (7.4)$$

Maximum encumbrance of the actuator for the chosen configuration:

$$E_{max} = 0.01 + 2\sqrt{0.1^2 - 0.01^2} = 0.21 \text{ m} \quad (7.5)$$

7.4 Required Speed Calculation

From the workspace calculation, stroke length of the actuator is around 0.6 m. Our design goal is to achieve a acceleration of 10g, where the actuator will accelerate constantly upto the half way point, and then decelerate to reach the final point.

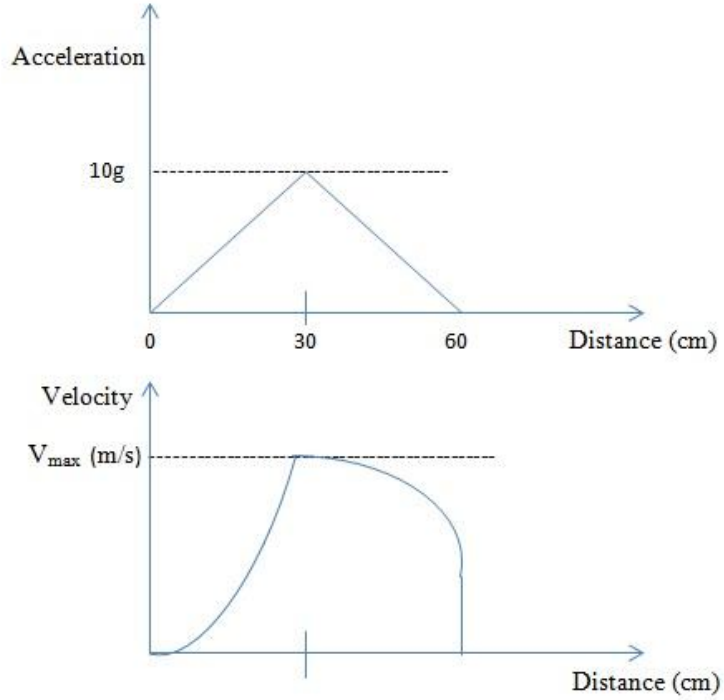


Figure 7.2 Maximum velocity and acceleration curve

For 10g acceleration, linear velocity of the actuator can be calculated from Newton's laws of motion equations and the value was 7.67 m/s. From kinematics, we can calculate the required angular velocity for the motor. Angular velocity for 10 g acceleration with a short link length of 0.1m is:

$$\omega = -7.67 * \frac{2}{4 * 0.1} \frac{1}{\sqrt{4 - \frac{(0.3)^2}{0.1^2}}} = 20.68 \frac{rad}{s} = 197.52 \text{ rpm} \quad (7.6)$$

From the dynamic simulation, we observed that the motor torque is around 3 Nm. Minimum required speed of the motor is 198 rpm. Based on the torque and angular velocity, Phidgets motor (Model # 3271_1) has been chosen for the practical prototype. Motor Specifications are presented in Chapter 8 (Section 8.5).

7.5 Deflection calculation

One end of the actuator will be connected on the base and the end effector will move freely. So, the actuator resembles a one end loaded cantiliver beam [51]. Vertical deflection of the end effector is calculated using the following formula:

$$\delta y = \frac{FL^3}{3EI} \quad (7.7)$$

In the above equation, F is the force acting on the tip of the beam, L is the length of the beam, E is modulus of elasticity and I stands for the area moment of inertia. Al 7079 alloy has been used as the material and from its properties the calculated deflection of the end effector is 0.0000714 cm.

7.6 Solidworks model

Based on the required design criteria and dimensions, a SolidWorks model was developed for the machining of the actuator. Shaft screws are used to connect the bars along with the bearings, to maintain a smooth rotation of the bar. Figure 7.3 shows the stator bar. Motor will be screwed with this bar at the base extremity. There will be a bearing inside the hole of the stator bar. Motor rotor shaft will go through that bearing and end up in the rotor bar. Figure 7.4 shows the rotor shaft bar. There will be a key way in the rotor bar to lock the rotor shaft with the bar. A set screw is used in the 90 degree direction to make the rotor shaft tight enough so that it can not move out during rotation. Below the rotor bar, there are holes for the screws to connect the actuator with robot or any other applications where it will be useful.

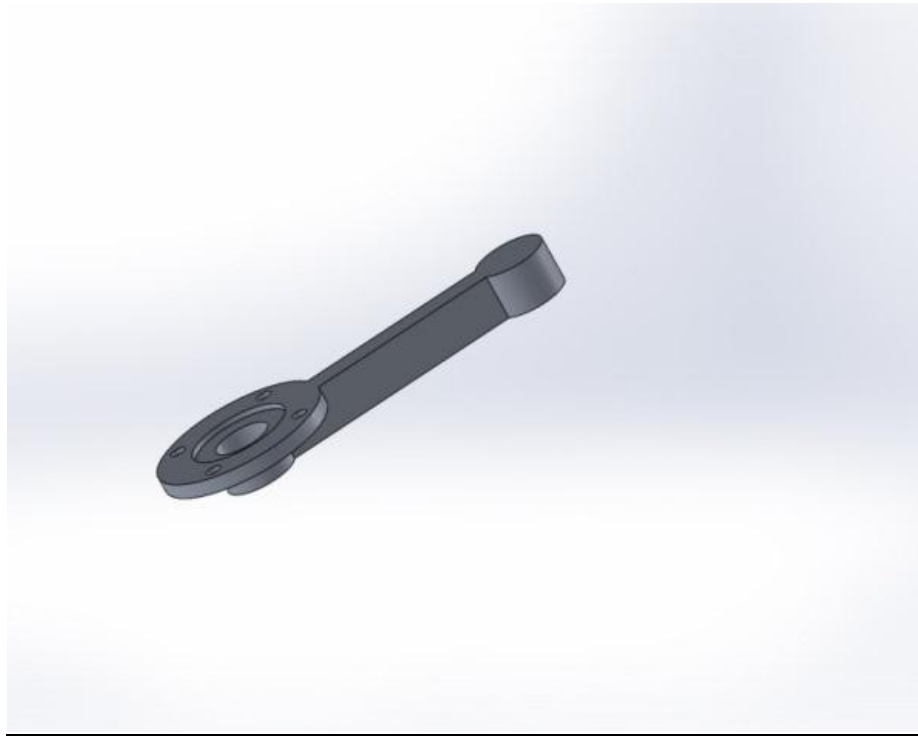


Figure 7.3 Motor stator bar

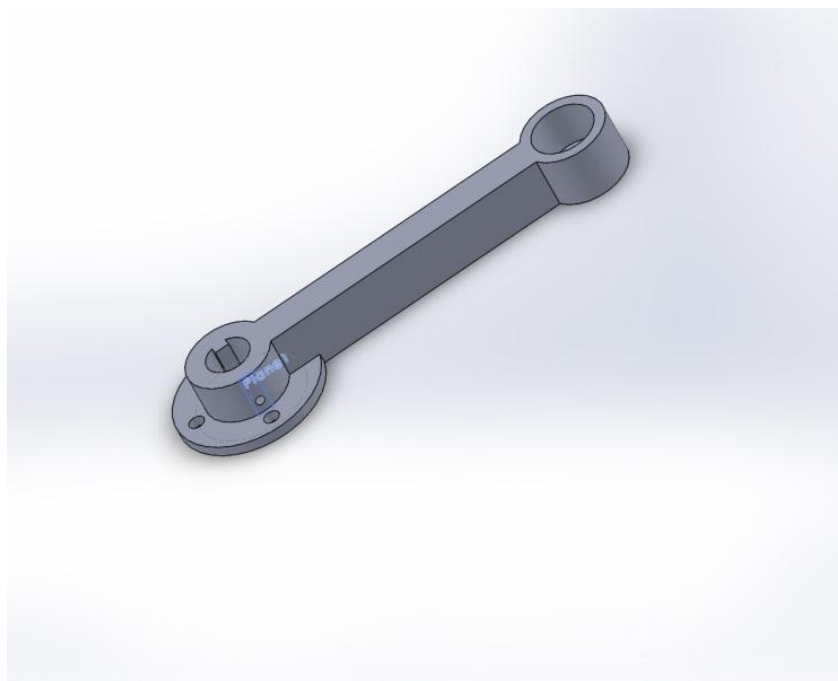


Figure 7.4 Rotor shaft bar

In the Figure 7.5, the holes in the upper bars create a housing for the shaft screws and the lower bars (Figure 7.6) consist of a bearing in each of the joint.

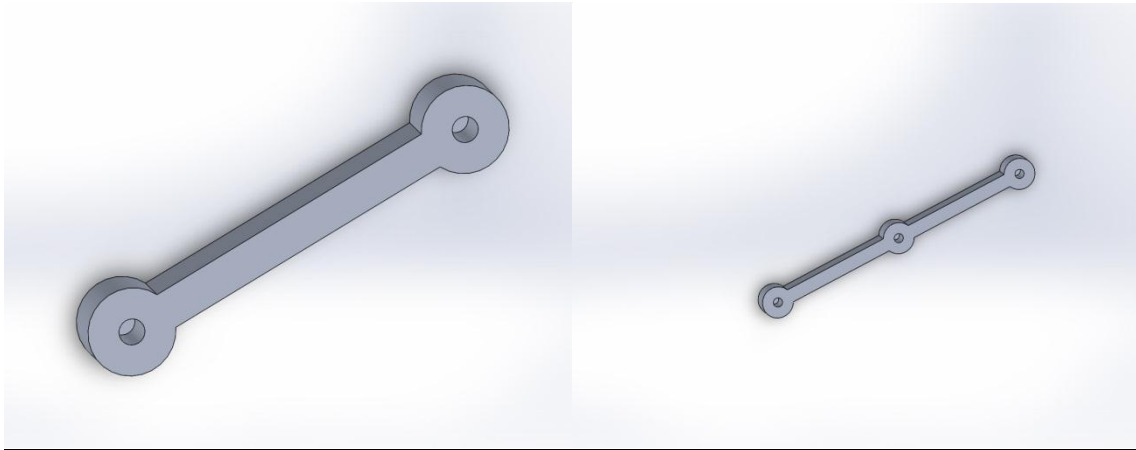


Figure 7.5 Upper bars (short and long)

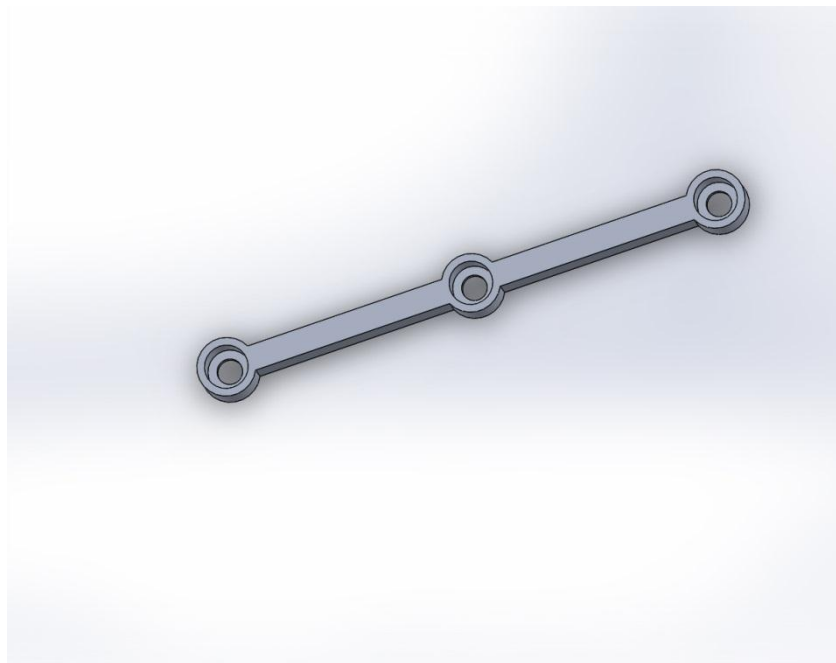


Figure 7.6 Lower bar

Figure 7.7 shows the bearing and shoulder screw assembly inside the actuator. Figure 7.8 shows the complete actuator assembly. In the end effector plate, there are holes to connect the screws for the load.

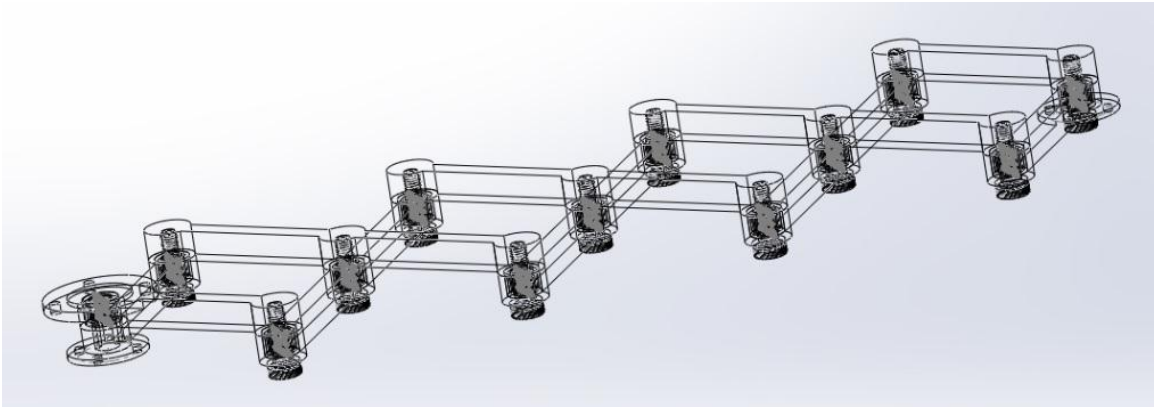


Figure 7.7 Bearing and Shoulder Screw Assembly



Figure 7.8 Actuator assembly

The base assembly consists of a fixed plate, flange and connector. The rotor shaft bar is screwed to the connector to demonstrate the reactive force movement of the motor.

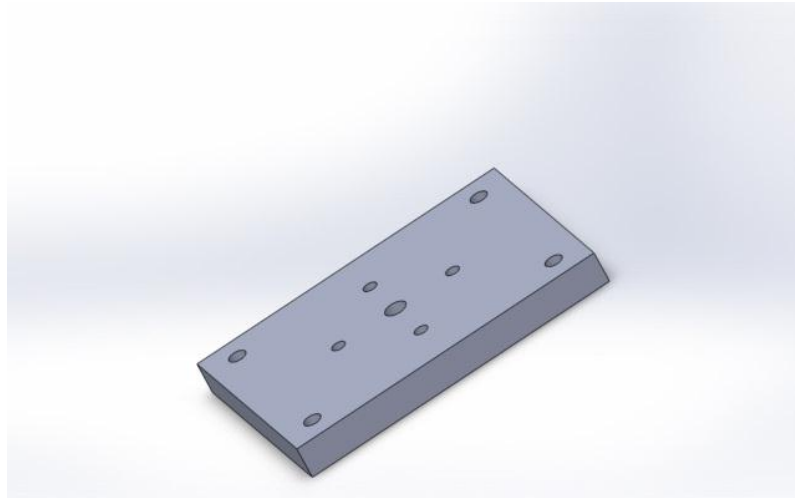


Figure 7.9 Fixed base

Between the flange and connector, a bearing is used to ensure smooth movement of the actuator.

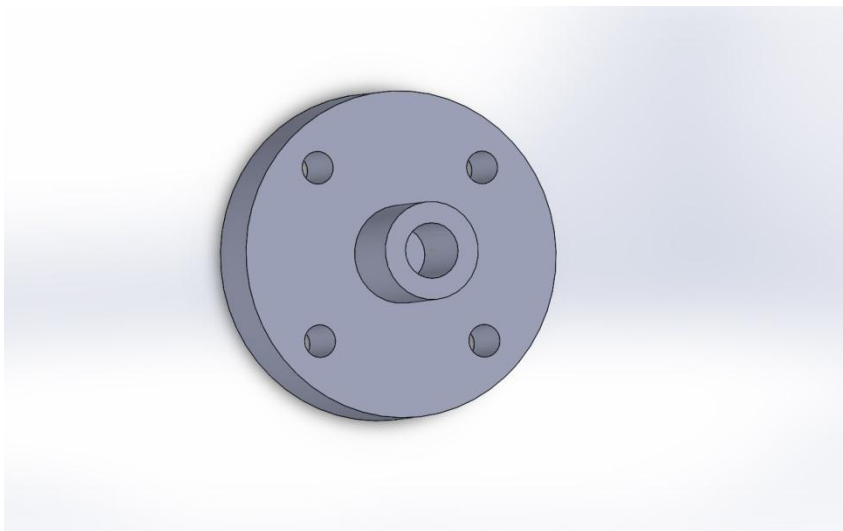


Figure 7.10 Base flange

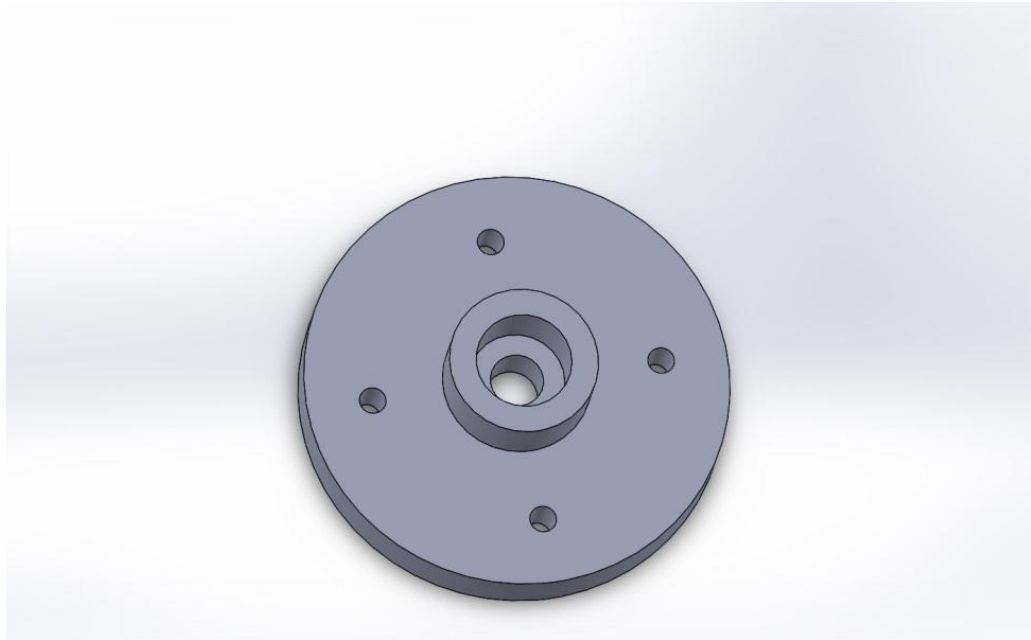


Figure 7.11 Base connector

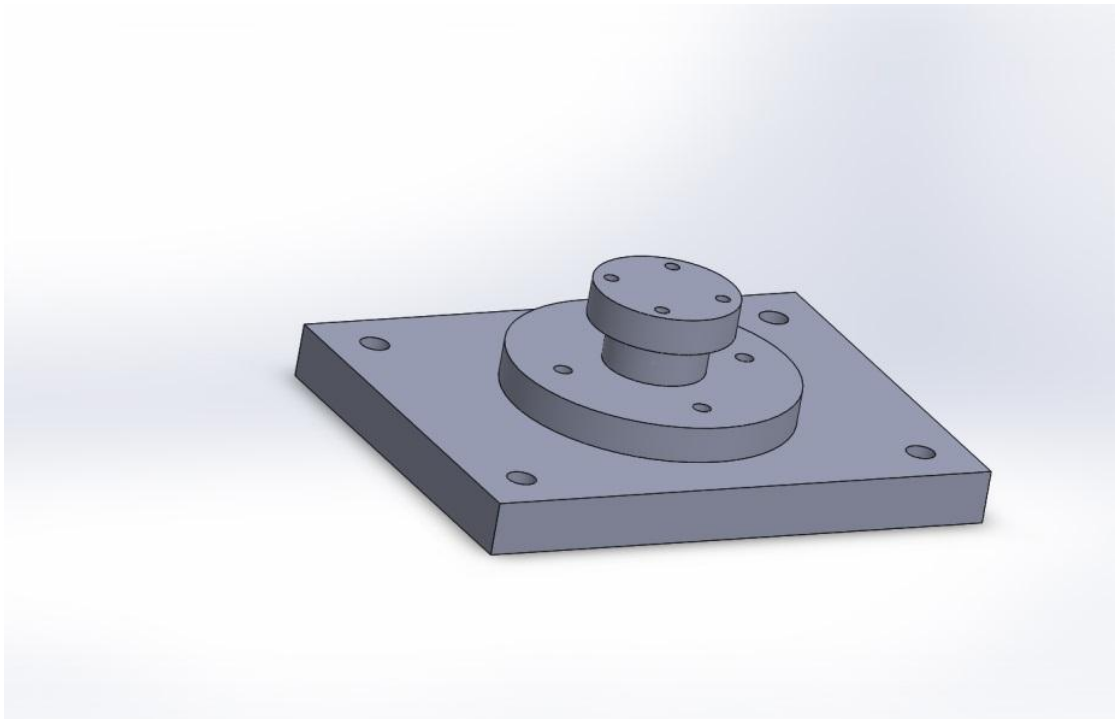


Figure 7.12 Base assembly



Figure 7.13 Actuator and base assembly

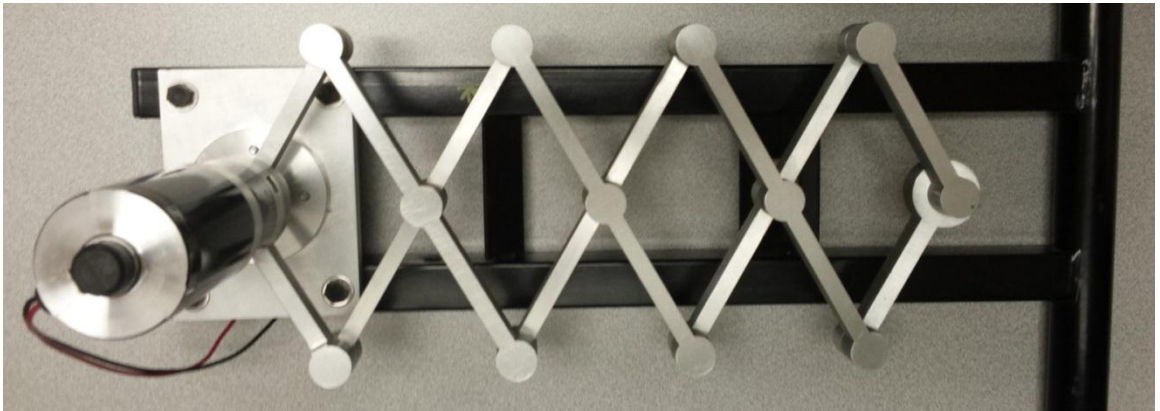


Figure 7.14 Actuator Prototype

7.7 High Performance Actuator with 3RPR robot

The newly designed actuator can be used in a standalone condition or in different robots. In our lab, after the standalone experimentation we want to use the actuator for the 3RPR parallel robot. Figure 7.15 shows a typical 3 RPR parallel robot. In a 3RPR robot, there are three prismatic actuators. As prismatic actuators are very slow in acceleration, we want to replace them by our high performance actuator. Another masters thesis is being done on the integration of the high performance actuator with 3RPR parallel robot and their performance evaluation with a parallel robot.

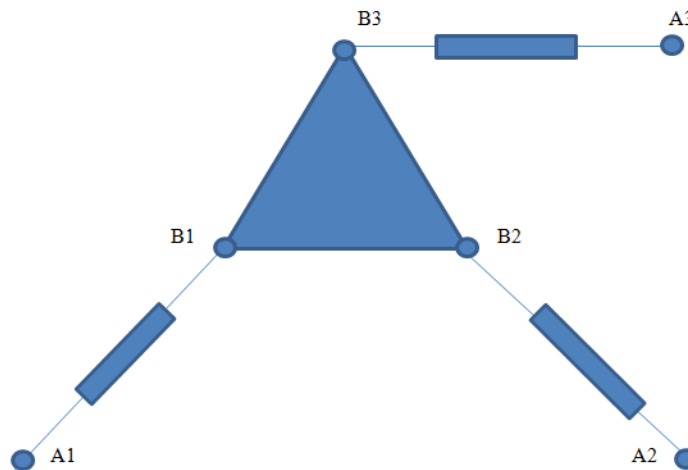


Figure 7.15 Schematic of a 3RPR Parallel Robot

7.9 Design Recommendations

The actuator prototype is to provide for a proof of concept. For precise movement of the end effector position, we need a motor with minimal backlash to reduce position error. From the actuator design, we can see that a small variation in the input angle will create a significant error in the linear position. This will increase as the number of network also

increases. The mechanism provides motion amplification, which is very well suited for high acceleration, but would require careful encoder choice in high precision applications. We used aluminum as the material. Any high strength material with low mass density (e.g. carbon fiber) will increase the performance of the actuator even more. Based on the requirements bar length, width and thickness can be reduced. It will reduce the overall mass and subsequently increase acceleration for the same amount of torque.

Chapter 8

Control of the Actuator

8.1 Introduction

This chapter provides the detailed control analysis of the newly designed actuator. For simulation and hardware implementation of control, conventional PID controller has been used. Controller provides control of the input angle of the actuator, but doesn't directly control the end effector (length of the linkage). As the designed actuator system is highly dynamic and nonlinear in nature, the PID controller is heavily impacted by the mathematical modeling of the system. For practical implementation Phidgets motor controller has been used [52].

8.2 General Control Schematic:

In a closed loop control system, there is a provision of feedback for precise control of the desired output. Figure 8.1 shows the general schematic of the closed loop control system for the actuator. For feedback, we are using the encoder and it is attached to the motor. Inside the controller block there are several components. Figure 8.2 shows the general controller schematic.

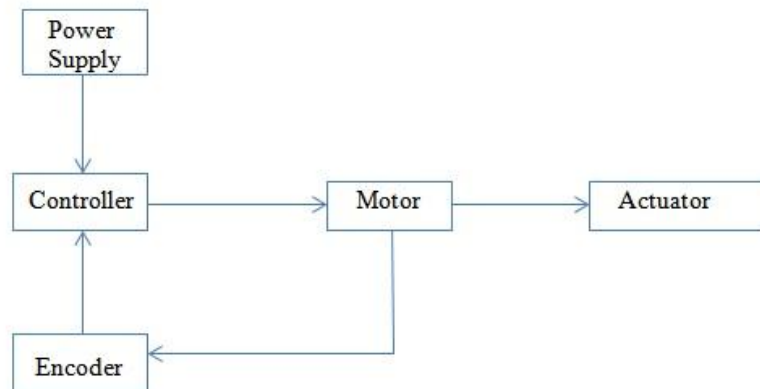


Figure 8.1 Block Diagram of Actuator Control

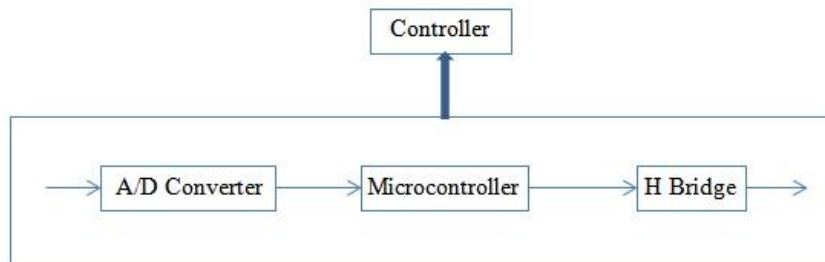


Figure 8.2 Controller Block Diagram

Closed loop control system contains a sensor, a motor, a controller, and a driver. Generally, the driver is an H bridge. Most common way is to let the controller turn the driver ON and OFF at very high rates, changing the ratio between ON and OFF time to control the speed of the motor. This technique is well known as PWM (pulse-width-modulation). In general, the H bridge contains four switching elements with the load at the center. Switching elements are usually BJT (Bipolar Junction Transistor), FET (Field Effect Transistor) or IGBT's (Insulated Gate Bipolar Junction Transistor). By controlling the ON-OFF sequence of the FET or IGBT we can reverse the current direction and hence can control the motor in clockwise and counterclockwise direction.

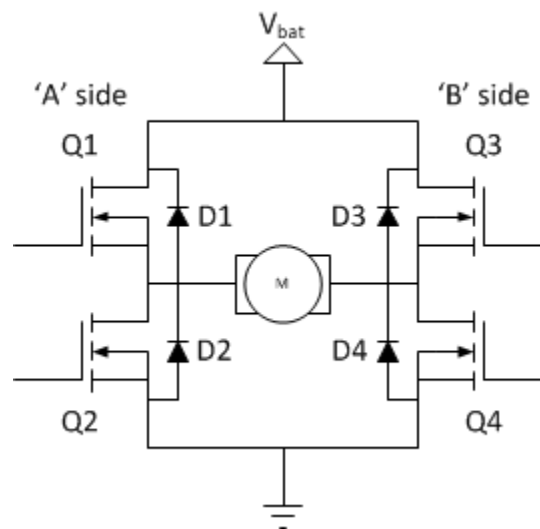


Figure 8.3 Schematic of H-Bridge Driver

While working with a DC motor, a shaft encoder is the most common and accurate way of providing feedback to the controller. Shaft encoders are rotary encoders. A shaft encoder provides the microcontroller internal counter with a sequence of pulses during a

period of time, which corresponds to the rotation of the motor. Microcontroller recalculates the actual angle of the shaft or the revolution. Then it controls the speed of the motor by comparing number of pulses with a fixed number, which is referred as the “required pulses”. Required pulses are calculated based on the program saved in the memory of the microcontroller chip. Figure 8.4 shows a general flow chart for encoder signal to the microcontroller to control the speed of motor.

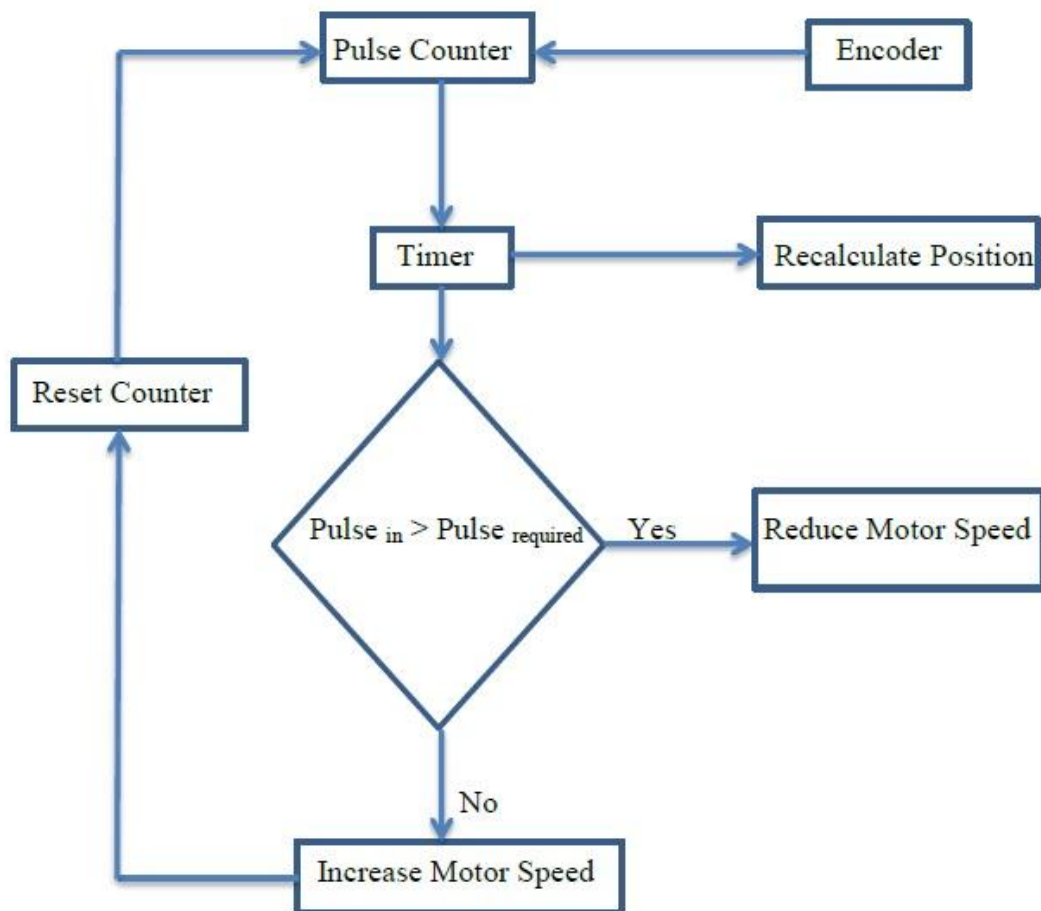


Figure 8.4 Microcontroller-Encoder Flow Diagram

8.3 Control Scheme and Algorithm

An electrical system model of a voice coil actuator for controlling a parallel orientation manipulator is presented in [52]. In our newly designed actuator, a DC motor provides the required input forces. In their causal structure, it needs to overcome the frictional force to move the end effector. Figure 8.5 shows an electrical model of the actuator with the friction model incorporated in it. Here, actuator velocity is the causal input and actuator force is the causal output. Motor transfer function can be achieved through the general control theory for simple DC motor circuit (armature with series connected inductance and resistance).

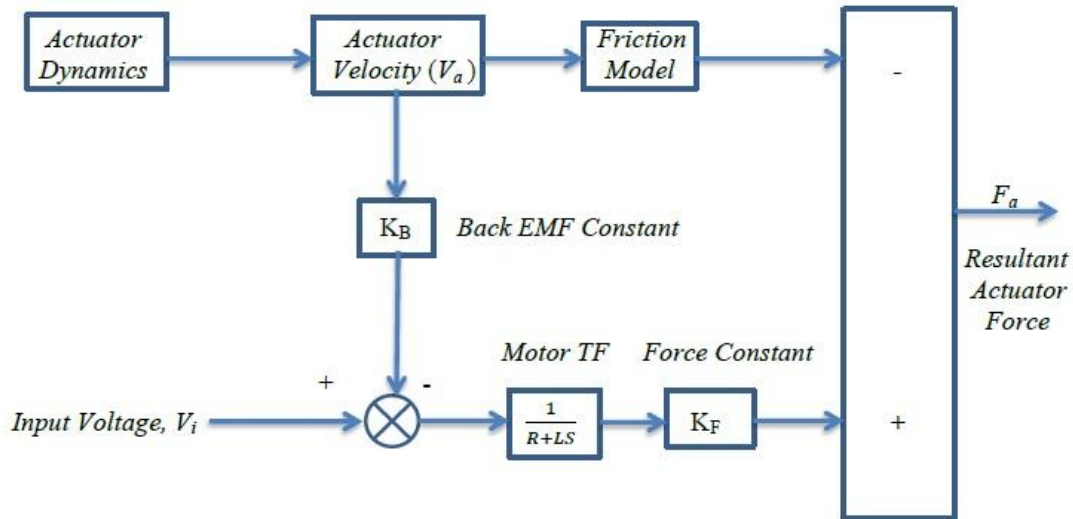


Figure 8.5 Electrical Model of the Actuator

As the actuator system is highly nonlinear, we cannot derive the transfer function until we build up a linearized model. This process is difficult for any parallel mechanism, since

there are computational complexities associated with it. That is why direct PID control is an effective way to implement the actuator control system. For PID control, performance of the system is determined by three parameters (Proportional, Integral and Derivative). Essentially, a PID controller looks like this:

$$o(t) = K_p e(t) + K_i \int_0^t e(\tau) d\tau + K_d \frac{d}{dt} e(t) \quad (8.1)$$

Where, K_p = Proportional gain, K_i = Integral gain, K_d = Derivative Gain, e = error and t = time or instantaneous time. Figure 8.6 shows the general block diagram of the direct PID control system. Here, input is the desired position of the end effector. We are controlling the input angle (denoted as θ) between the stator and rotor bar at the base extremity. Actuator body contains several four bar rhombus configuration. From kinematic relationship we can calculate the link length based on the number of rhombus network. For a known link length, IKM (Inverse Kinematics Model) will produce the desired angle. From the present θ value between the stator and rotor bar, approximation of the end effector position can be calculated using the FKM (Forward Kinematics Model). From the initial position to the desired position actuator follows a trajectory. For a linear actuator it should be one straight line. End effector of the actuator travels the path and its actual trajectory can be calculated from the FKM. Here, controller only manages the angular position of the motor and the actuator linear position is derived by kinematics calculation. One PID controller is dedicated to one linear actuator. When this actuator is implemented in one robot or any machine, the external loop is closed at the robot

controller level. That means all the actuator controller will be connected with another main controller. The main controller will control the robot base as well as the actuator.

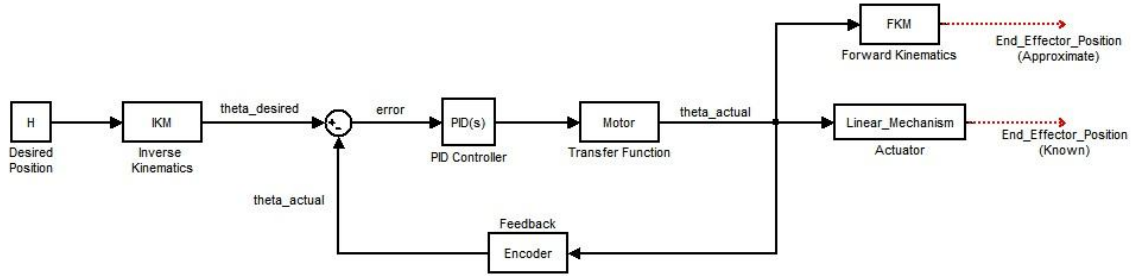


Figure 8.6 General Block Diagram of Actuator Control

Figure 8.7 shows the Simulink model of direct PID control. Actuator dynamics is used to get the actual θ value. For actuator dynamics, we can use any conventional dynamic formulation method. Here, Lagrangian formulation is used to get the actual θ of the system while moving from the initial position to the desired position. From Lagrangian formulation we know:

$$Q = M\ddot{\theta} + N + G \quad (8.2)$$

Solving Eq. (8.2) we can calculate the angular acceleration ($\ddot{\theta}$) of the system.

$$\ddot{\theta} = M^{-1}(Q - N - G) \quad (8.3)$$

Integration of $\ddot{\theta}$ gives the angular velocity and subsequently the present angle.

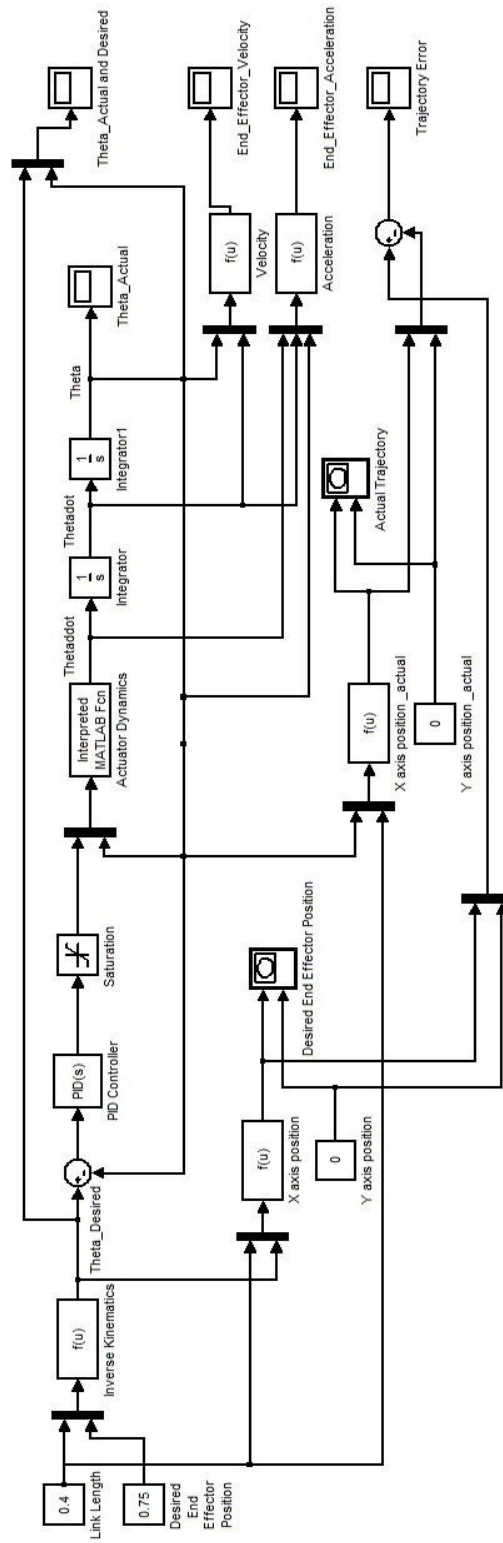


Figure 8.7 Simulink Diagram of Direct PID Control

8.4 Simulation and Result Interpretation

This section shows the simulation figures of the direct PID control through the simulink block diagram. For simulation we considered the single rhombus network configuration of the actuator. Input link length is 0.4m and desired position of the end effector is 0.75m. Figure 8.8 shows the desired point and actual trajectory to reach that point for the end effector. Desired position is a single point on the graph. For the end effector trajectory, the angle control starts from zero. For zero degree the maximum position is 0.8m. From that point it starts moving towards the desired position. End effector moved beyond the 0.75 m as there are some overshoot in the system. Figure 8.9 shows the desired and actual angle values of the system. In the figure, we can see the actual input angle curve perfectly reached to the desired value after some overshoot. From the simulink model, we can get the velocity and acceleration of the end effector.

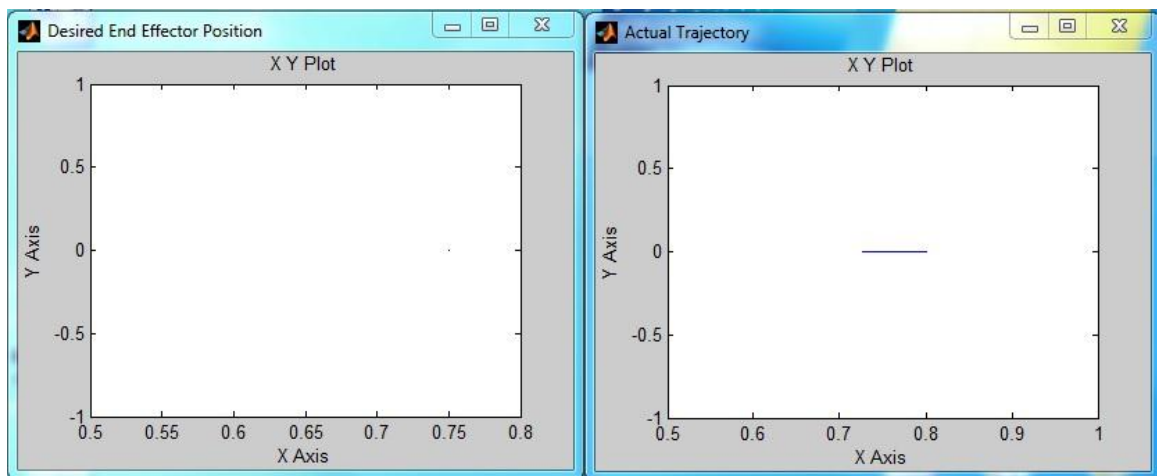


Figure 8.8 Desired Position and Actual Trajectory

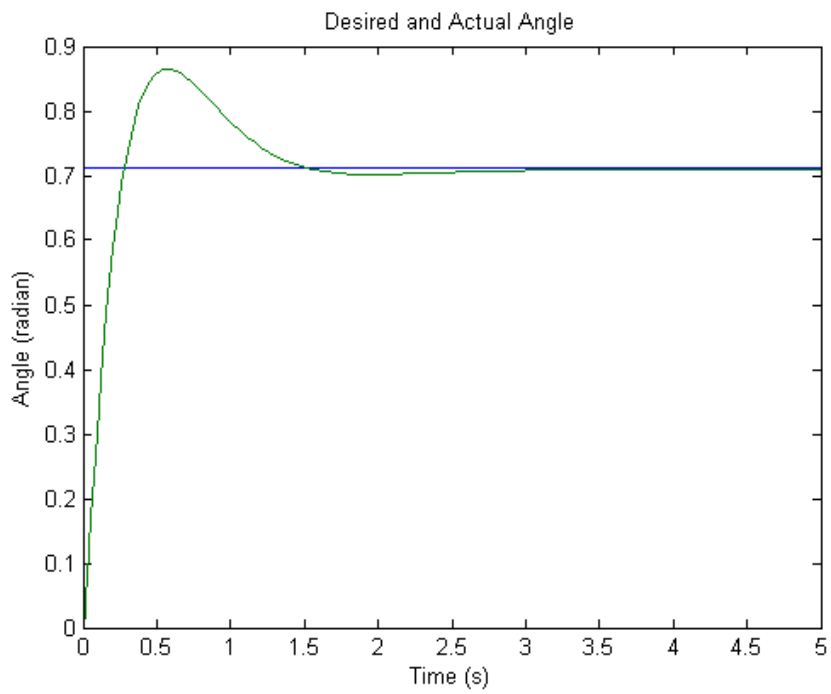


Figure 8.9 Desired angle and Actual Angle

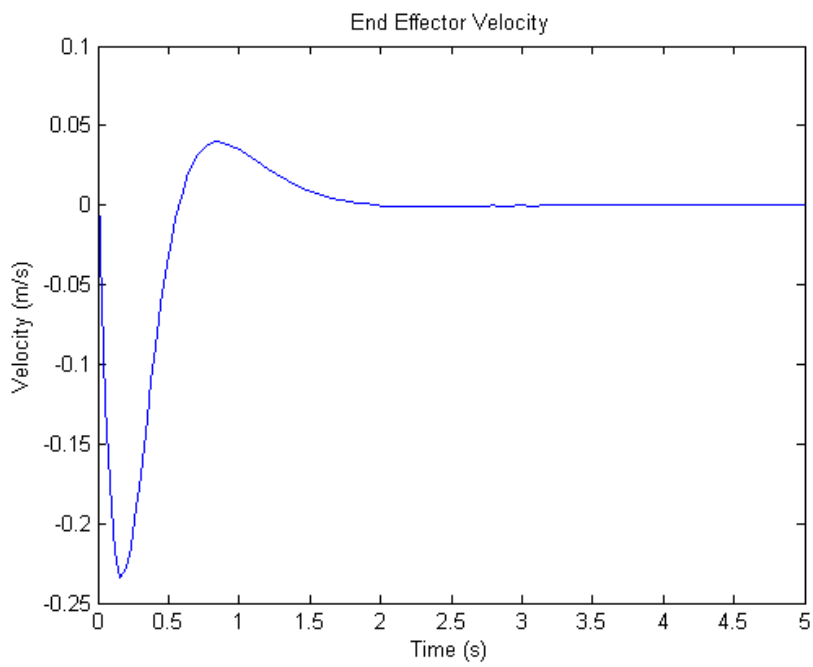


Figure 8.10 End effector velocity

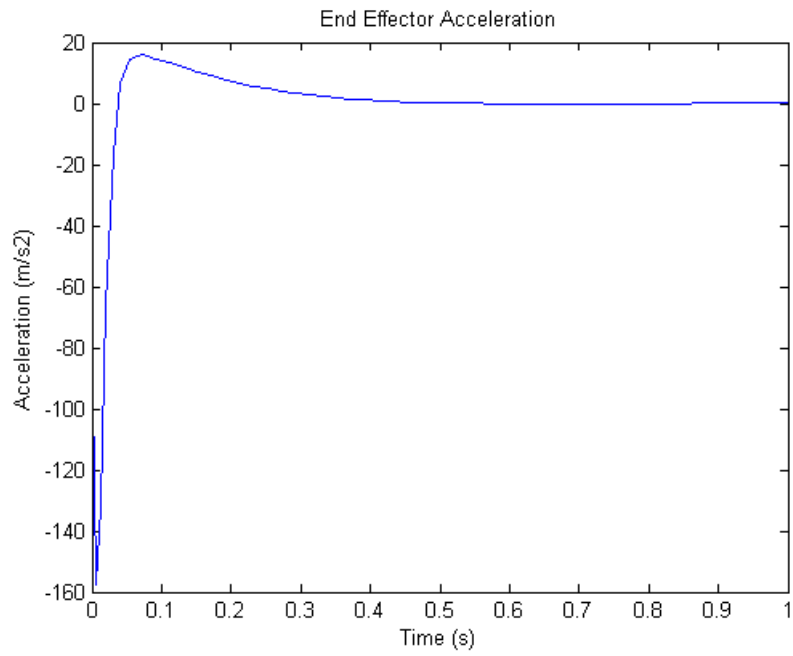


Figure 8.11 End Effector Acceleration

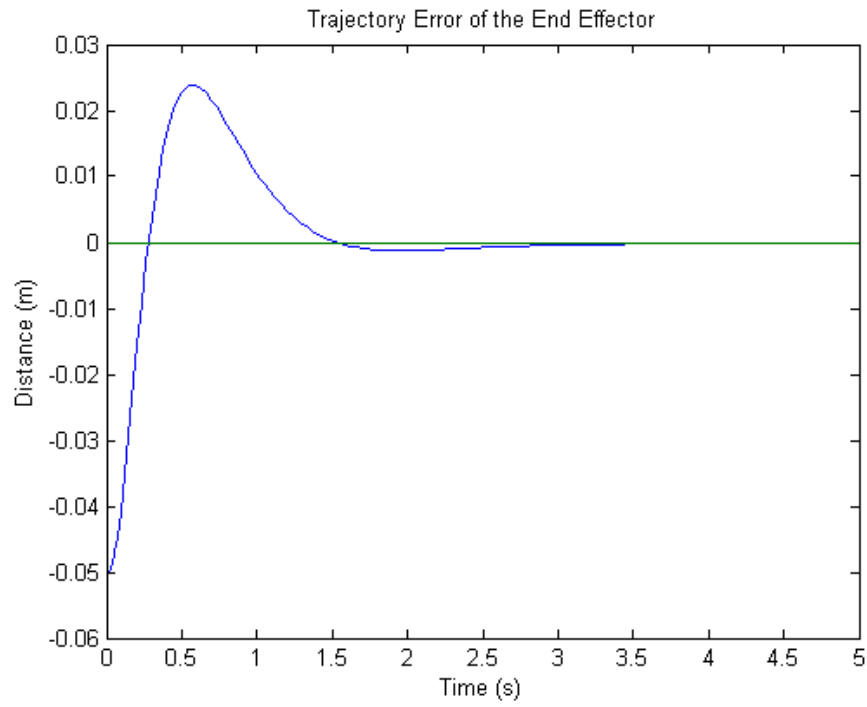


Figure 8.12 Trajectory Error

Figure 8.11 shows the acceleration of the end effector. Acceleration is very high at the initial stage of the simulation as would be the expected result from a typical PID loop. It reaches very quickly to the stable point. Figure 8.12 shows the trajectory error between the desired and actual trajectory of the end effector. Trajectory steady-state error is minimum for the system being close to zero means that the PID parameters are a good compromise. However, the position overshoot is relatively large indicates the need for parameter tuning. Here, lagrangian formulation has been used to simulate the actuator dynamic behavior. Due to the parameter tuning error, this approach took more time to reach the target values compared to the bond graph dynamic simulation.

8.5 Practical Controller Implementation

For practical demonstration of the actuator, we used Phidgets DC Gear motor (model # 3271_E) with built in rotary encoder. Motor and encoder properties are given in Table 8.1 and Table 8.2.

Table 8.1 Motor Specifications

Motor Properties	
Motor Type	DC Motor with Encoder
Output Power (Mechanical)	30 W
Maximum Speed at Rated Voltage	139 RPM
Rated Torque	20.4 kg·cm
Stall Torque	132 kg·cm

Electrical Properties	
Rated Voltage	24 V DC
Rated Current	2.2 A
Stall Current	10.8 A

Physical Properties	
Shaft Diameter	12 mm
Wire Length	300 mm
Weight	1.5 kg

Gearbox Properties	
Gearbox Type	Planetary
Gear Ratio	18 ¹ / ₁₆ : 1
Number of Gear Trains	2
Maximum Strength of Gears	153 kg·cm
Shaft Maximum Axial Load	200 N
Shaft Maximum Radial Load	100 N
Backlash Error	3°

Table 8.2 Encoder Specifications

Encoder Resolution	360 CPR
Connector Type	E4P
Current Consumption Min	27 mA
Supply Voltage Min	4.5 V DC
Supply Voltage Max	5.5 V DC

Phidget 1065 motor controller has been used. The 1065 controller control the direction, velocity and acceleration of one DC Motor. The motor is powered by an external power supply (9 to 28VDC). By applying a voltage, or pulsing a voltage rapidly, at the terminals of the motor, current flows through the motor and it will begin rotating. Depending on the direction of the current, the motor will rotate clockwise or counterclockwise. The 1065 changes the effective voltage by changing the percentage of time the full supply voltage is applied to the motor. By switching the voltage very quickly (a technique called PWM), the controller is made smaller, more efficient, and cheaper. Control of actual motor speed can be achieved automatically in software by using the Back EMF property, or current sensing [49]. Precise position control of DC motors is achieved by using encoders.

Control loops implemented through software by using the data provided by the on-board digital inputs, analog inputs and encoder input. There is an event that triggers every 16 ms and returns the back-EMF value for the attached motor, which is used for PID control. Figure 8.13 shows the schematic of the controller. Figure 8.14 shows the linear actuator with controller connected in it. This controller also provides built in over voltage and over current protection. Detailed controller properties are given in Appendix C.



Figure 8.13 Phidget Controller

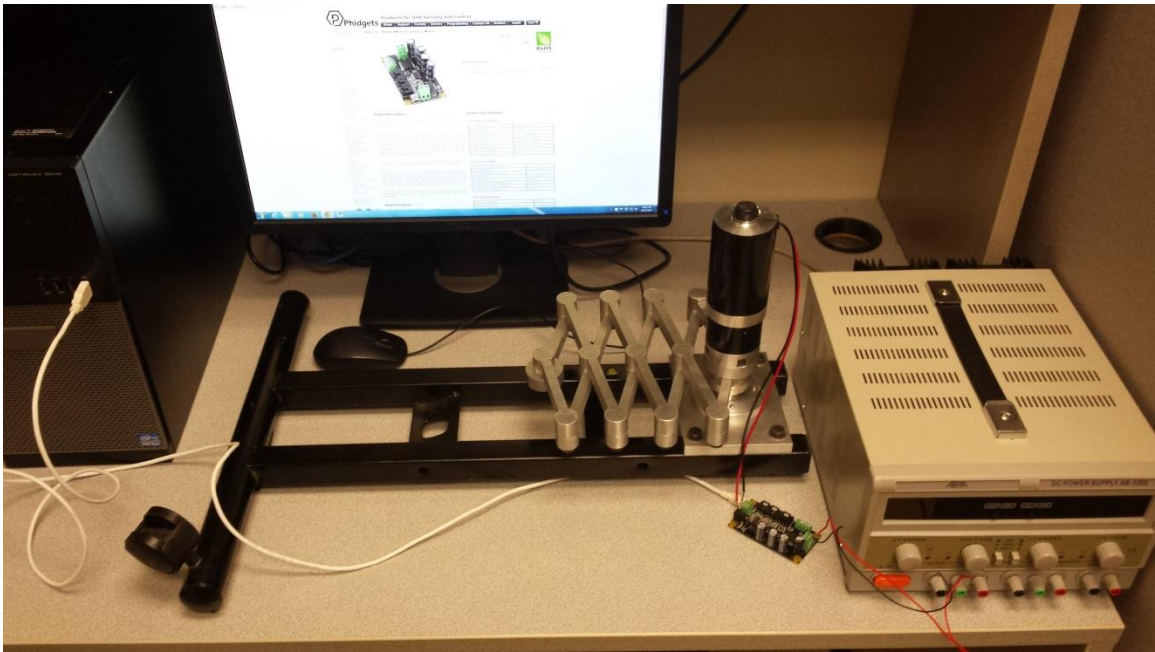


Figure 8.14 Linear Actuator with Controller

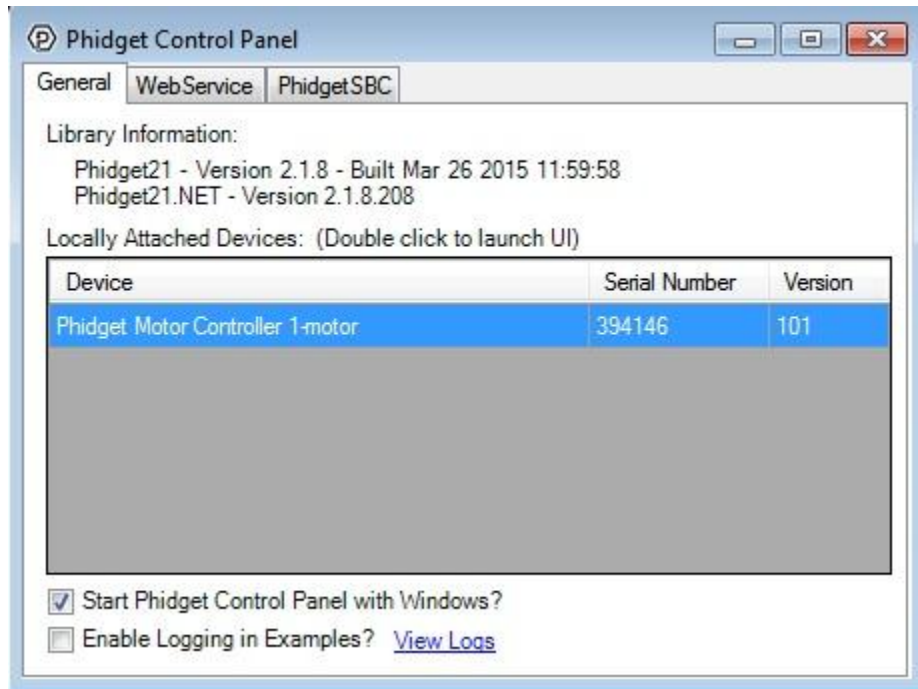


Figure 8.15 Controller Connection Window

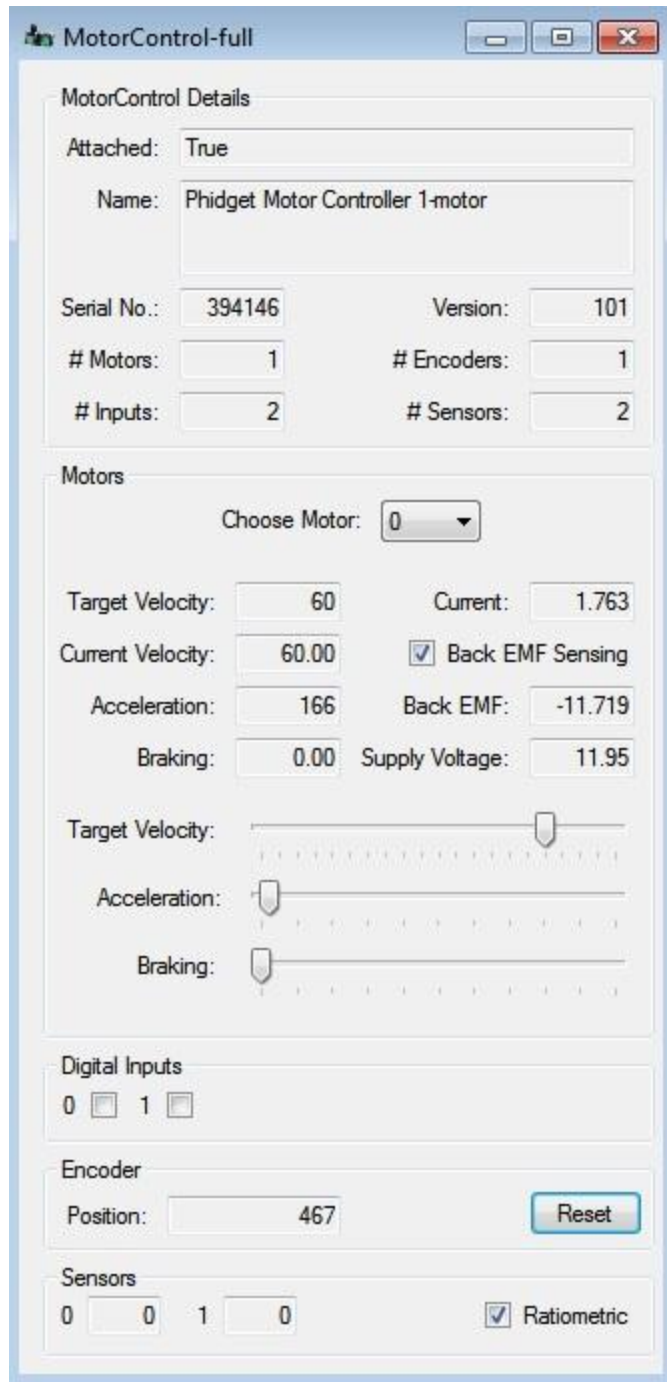


Figure 8.16 Controller Performance Window

Table 8.3 Control Performance Summary

Supply Voltage	11.95 V
Current	1.763 A
Maximum Velocity	60 m/s
Maximum Acceleration	166 m/s ²

Figure 8.15 shows the Phidgets motor control connection window. When a device is connected with the controller board, it shows the device ID. In our experimental set up, the Phidget DC motor (serial # 394146) is connected as we are controlling the input angle from encoder reading. Figure 8.16 shows the motor control panel. From the figure one can observe the motor run data. Its showing that 1 motor and 1 encoder is connected. With the slider one can vary the target velocity. For this typical case supply voltage was 12V and current was 1.763 Amps. Actuator target velocity was set to 60 m/s and acceleration is around 17g. From the data, we can see that the current velocity and acceleration resembles the target velocity and acceleration.

Chapter 9

DOE Data Analysis and Design Optimization

9.1 Introduction

Using the Bond Graph dynamic model and kinematic formulation of the newly designed actuator, acceleration of the end effector is simulated for different parametric combinations. For the practical design, to achieve the high performance (acceleration) is the main concern. This chapter describes the detailed procedures to determine the ideal parametric combinations for the actuator, so that it gives the best performance. Statistical data analysis is a great addition for this type of parallel mechanism. Brief description of DOE is presented in Appendix B.

9.2 Experimental Factors and Response

We considered five parameters as input factors and the output response is the acceleration of the end effector for different loading condition.

- Network (A): Network means how many identical rhombus structures are in the actuator body. Networking of rhombus has significant effect on the acceleration of end effector. Because, each network linearly increases the velocity of the end effector and subsequently acceleration.
- Link Length (B): Considered link length is the length of the short bar. Link length varies with the number of network. As the network number goes higher, it goes smaller. Motor stator and rotor shaft both are connected with one but distinct short bar. So this factor is very important.
- Torque Requirement Duration (C): From dynamic simulation, we have seen that the peak torque requirement for different networks combination remains constant but the torque requirement duration varies.
- End Effector Loading (D): End effector loading has a negative impact on the acceleration. So, this is a very crucial parameter for design calculation. Data collected for three different loading conditions (0.5 Kg, 1Kg and 1.5Kg).
- Movement Direction (E): The newly designed actuator can be used both in horizontal and vertical direction. For vertical movement there will be extra torque required to overcome the gravity force.

Response is the acceleration of the end effector. The main goal of this design is to achieve high acceleration while using them in robots or in standalone condition.

9.3 Optimal (custom) Design of the Experiment

Response surface methodology (Appendix B) has been used to analyze the collected data. Computer based optimal (custom) design is chosen to build up the model. For 5 factors (4 numeric and 1 categorical), it requires total 30 runs. Design Expert software (version 9) by Stat-Ease has been used to develop the optimal design. For network and link length there are 5 different levels. Torque requirement duration (motor run time) is different for each of the simulation run. For directional movement, level 2 considered as vertical direction and level 1 considered as horizontal direction.

Select	Run	Factor 1 A:Network	Factor 2 B:Link Length m	Factor 3 C:Torque Requirement Duration S	Factor 4 D:End Effector Loading Kg	Factor 5 E:Movement Direction	Response 1 Maximum Acceleration m/s ²
	1	5	0.08	0.93	0.5	Level 2 of E	57.35
	2	5	0.08	1.15	1	Level 2 of E	32.47
	3	5	0.08	1.24	1.5	Level 2 of E	27.74
	4	5	0.08	0.83	0.5	Level 1 of E	22.4
	5	5	0.08	1	1	Level 1 of E	14
	6	5	0.08	1.175	1.5	Level 1 of E	9.3
	7	4	0.1	0.81	0.5	Level 2 of E	19.27
	8	4	0.1	0.99	1	Level 2 of E	11.12
	9	4	0.1	1.3	1.5	Level 2 of E	8.13
	10	4	0.1	1.06	0.5	Level 1 of E	72
	11	4	0.1	1.3	1	Level 1 of E	44.1
	12	4	0.1	1.52	1.5	Level 1 of E	40.86
	13	3	0.1333	0.92	0.5	Level 2 of E	20
	14	3	0.1333	1.14	1	Level 2 of E	11.5
	15	3	0.1333	1.28	1.5	Level 2 of E	8.17
	16	3	0.1333	0.8	0.5	Level 1 of E	19.7
	17	3	0.1333	1.15	1	Level 1 of E	11.34
	18	3	0.1333	1.28	1.5	Level 1 of E	8.21
	19	2	0.2	0.88	0.5	Level 2 of E	16.04
	20	2	0.2	1.2	1	Level 2 of E	9.58
	21	2	0.2	1.35	1.5	Level 2 of E	9.26
	22	2	0.2	1.9	0.5	Level 1 of E	11.41
	23	2	0.1	2.35	1	Level 1 of E	4.96
	24	2	0.2	2.5	1.5	Level 1 of E	3.56
	25	1	0.4	0.92	0.5	Level 2 of E	7.5
	26	1	0.4	1.1	1	Level 2 of E	10.17
	27	1	0.4	1.36	1.5	Level 2 of E	7.52
	28	1	0.4	0.93	0.5	Level 1 of E	7.4
	29	1	0.4	1.1	1	Level 1 of E	10.77
	30	1	0.4	1.37	1.5	Level 1 of E	7.8

Figure 9.1 Run Data

9.4 ANOVA Analysis and Regression Model

ANOVA table summarizes the statistical significance of the proposed DOE model. From the F-value and probability value comparison of the effects, the software determines the significance.

Table 9.1 ANOVA Analysis

Response 1		Maximum Acceleration				
ANOVA for Response Surface 2FI model						
Analysis of variance table [Partial sum of squares - Type III]						
Source	Sum of Squares	df	Mean Square	F Value	p-value Prob > F	
Model	6583.49	15	438.90	5.82	0.0010	significant
<i>A-Network</i>	29.24	1	29.24	0.39	0.5434	
<i>B-Link Length</i>	11.23	1	11.23	0.15	0.7052	
<i>C-Torque Re</i>	0.13	1	0.13	1.668E-003	0.9680	
<i>D-End Effect</i>	10.35	1	10.35	0.14	0.7165	
<i>E-Movement</i>	5.145E-003	1	5.145E-003	6.827E-005	0.9935	
AB	11.76	1	11.76	0.16	0.6988	
AC	52.20	1	52.20	0.69	0.4192	
AD	23.96	1	23.96	0.32	0.5818	
AE	3.12	1	3.12	0.041	0.8416	
BC	14.38	1	14.38	0.19	0.6689	
BD	32.64	1	32.64	0.43	0.5212	
BE	3.55	1	3.55	0.047	0.8312	
CD	27.67	1	27.67	0.37	0.5543	
CE	9.61	1	9.61	0.13	0.7263	
DE	23.49	1	23.49	0.31	0.5854	
Residual	1055.08	14	75.36			
Cor Total	7638.58	29				

Std. Dev.	8.68	R-Squared	0.8619
Mean	18.12	Adj R-Squared	0.7139
C.V. %	47.91	Pred R-Squared	N/A
PRESS	N/A	Adeq Precision	8.256

In summary, the standard deviation shows the deviation of the error term. R^2 presents the percentage of total variability explained by the model. Addition of effect will increase the R value. That is why we should look at the adjusted R value produced by the model. The difference between the two R^2 should be very small. Precision should be greater than 4 for an adequate model. Table 9.1 shows the ANOVA table and the ANOVA summary for the 2FI backward elimination model. The backward method is considered the most robust choice for algorithmic model reduction because all model terms will be given a chance to be included in the model and categorical terms removed hierarchically. For our analysis, the R^2 values are not very close but precision is much greater than 4 which signify the adequacy of the model. But there may be a possibility of model transformation.

9.5 Residual Analysis

Residual analysis checks whether the assumptions of the ANOVA are correct or not. We made the following assumptions:

1. Random Samples from their respective population.
2. All samples are independent.
3. Departures from group mean are normally distributed for all data groups.
4. All data groups have equal variance.

We have seen from the ANOVA table that there are some differences in the R^2 values. Before further analysis, we will determine whether any transformation is required or not. From the Box-Cox plot of Figure 9.2 we can see that the current line is outside of the ranges (between Low & High Confidence Interval). That means transformation is

required and inverse square root transformation is recommended. So, we can conclude that the assumptions of ANOVA are not satisfied.

Design-Expert® Software
Maximum Acceleration

Lambda
Current = 1
Best = -0.4
Low C.I. = -1.07
High C.I. = 0.15

Recommend transform:
Inverse Sqrt
(Lambda = -0.5)

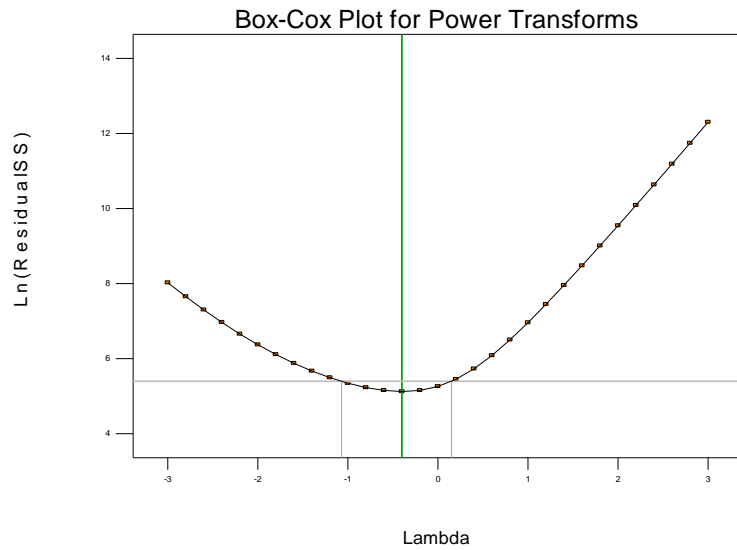


Figure 9.2 Box-Cox plot

9.6 Model Transformation

Table 9.2 shows the summary of the model after inverse square root transformations. From the fit summary table, we can see that transformation improved the model adequacy. But the suggested models remain similar (Linear or 2FI). 2FI backward elimination model is chosen for residual analysis.

Table 9.2 ANOVA Analysis After Model Transformation

ANOVA for Response Surface Reduced 2FI model						
Analysis of variance table [Partial sum of squares - Type III]						
	Sum of		Mean	F	p-value	
Source	Squares	df	Square	Value	Prob > F	
Model	0.24	9	0.026	29.27	< 0.0001	significant
<i>A-Network</i>	6.738E-004	1	6.738E-004	0.75	0.3980	
<i>B-Link Length</i>	0.029	1	0.029	31.68	< 0.0001	
<i>C-Torque Requirement Duration</i>	0.059	1	0.059	65.12	< 0.0001	
<i>D-End Effector Loading</i>	0.024	1	0.024	26.19	< 0.0001	
AB	0.061	1	0.061	68.07	< 0.0001	
AD	7.875E-003	1	7.875E-003	8.72	0.0079	
BC	0.061	1	0.061	67.46	< 0.0001	
BD	0.056	1	0.056	62.47	< 0.0001	
CD	1.417E-003	1	1.417E-003	1.57	0.2248	
Residual	0.018	20	9.031E-004			
Cor Total	0.26	29				

Std. Dev.	0.030	R-Squared	0.9294
Mean	0.29	Adj R-Squared	0.8977
C.V. %	10.49	Pred R-Squared	N/A
PRESS	N/A	Adeq Precision	23.316

$$\begin{aligned}
&1/\text{Sqrt}(\text{Maximum Acceleration}) = \\
&\quad +2.21551 \\
&+0.022592 * \text{Network} \\
&\quad -3.09650 * \text{Link Length} \\
&\quad -1.12923 * \text{Torque Requirement Duration} \\
&\quad +0.89250 * \text{End Effector Loading} \\
&\quad -3.64040 * \text{Network} * \text{Link Length} \\
&\quad -0.073127 * \text{Network} * \text{End Effector Loading} \\
&\quad +5.82053 * \text{Link Length} * \text{Torque Requirement Duration} \\
&\quad -3.59483 * \text{Link Length} * \text{End Effector Loading} \\
&\quad +0.053264 * \text{Torque Requirement Duration} * \text{End Effector Loading}
\end{aligned}$$

Figure 9.3 Mathematical Equation for Output

Figure 9.4 shows the normal plot. The actual results show that, all the data points are randomly distributed. Residual plots provide information about the normal distribution and constant variance of collected data. The results in the Box-cox plot (Figure 9.7) suggested no transformation is required.

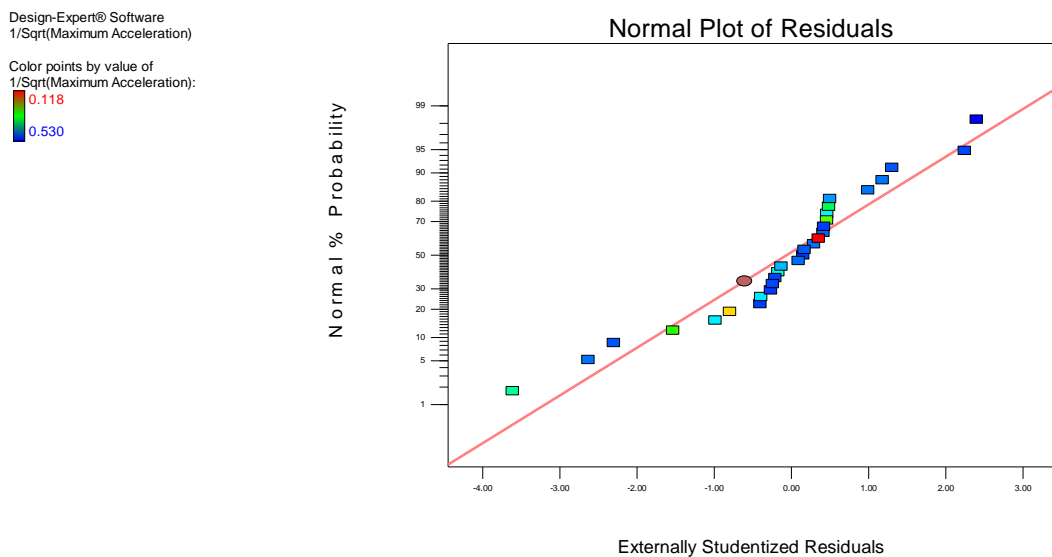


Figure 9.4 Normal plot of residuals (with inverse square root transformation)

Design-Expert® Software
 1/Sqrt(Maximum Acceleration)
 Color points by value of
 1/Sqrt(Maximum Acceleration):
 0.118
 0.530

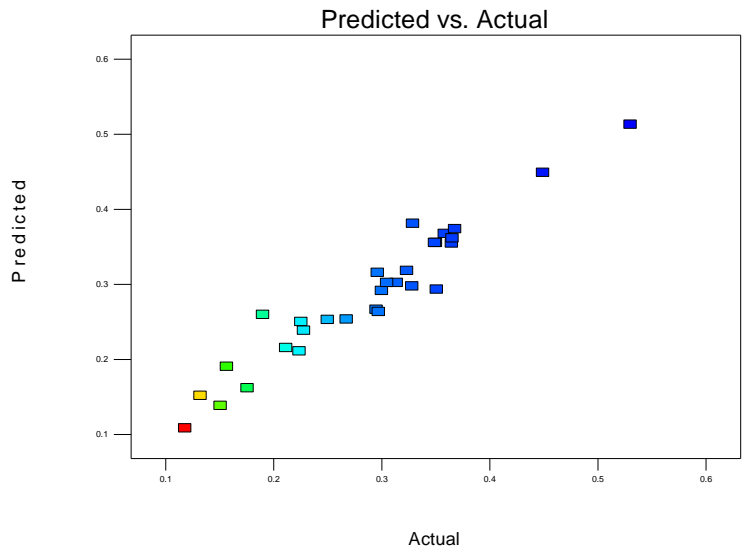


Figure 9.5 Predicted vs. actual plot (with inverse square root transformation)

Design-Expert® Software
 1/Sqrt(Maximum Acceleration)
 Color points by value of
 1/Sqrt(Maximum Acceleration):
 0.118
 0.530

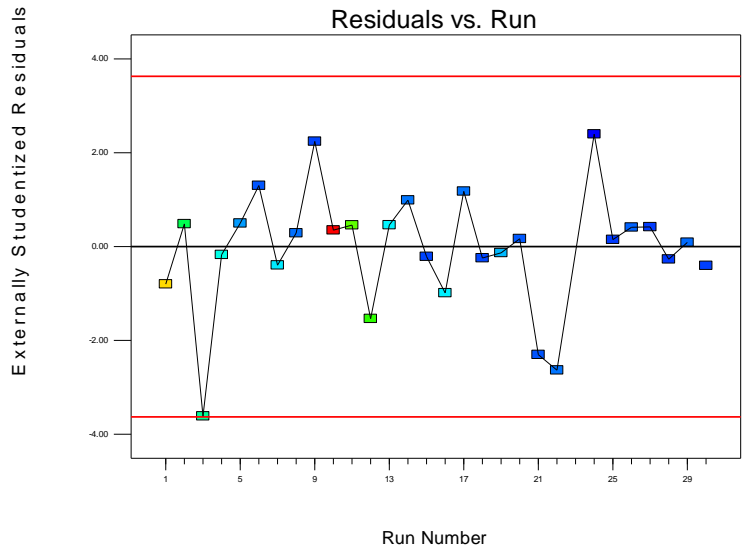


Figure 9.6 Residual vs. Run plot (with inverse square root transformation)

Design-Expert® Software
1/Sqrt(Maximum Acceleration)

Lambda
Current = -0.5
Best = -0.45
Low C.I. = -1.01
High C.I. = 0.03

Recommend transform:
Inverse Sqrt
(Lambda = -0.5)

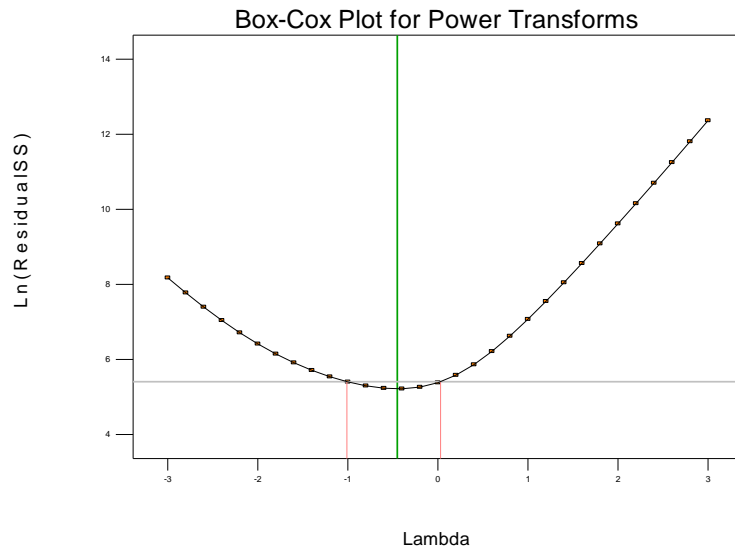


Figure 9.7 Box-cox plot (with inverse square root transformation)

9.7 Model Optimization

The model was optimized and extra runs performed for validity check. All factors were kept in range and acceleration was fixed at 50 m/s² to get the optimum runs. For the first ten combinations, obtained output is within our specified range to describe the model as a valid one. Table 9.3 shows that for the certain target acceleration all factors are in their specified range and we can determine the values for each of the factor. Output confirms the validity of the model to find the parametric combination and their respected values for certain height coverage. Here factor values are taken from their original run data sheet. For the first run, the suggested network combination is the network 3 and movement direction is vertical. Motor run time was 1.14 second. In the same way, from optimization run we can determine the ideal parametric combination based on the provided options.

Table 9.3 Optimization Run

Constraints						
		Lower	Upper	Lower	Upper	
Name	Goal	Limit	Limit	Weight	Weight	Importance
A:Network	is in range	1	5	1	1	3
B:Link Length	is in range	0.08	0.4	1	1	3
C:Torque Requirement Duration	is in range	0.8	2.5	1	1	3
D:End Effector Loading	is in range	0.5	1.5	1	1	3
Maximum Acceleration	is target = 60	1.57	72	1	1	3

Network	Link Length	Torque Requirement Duration	End Effector Loading	Movement Direction
3	0.1333	1.14	1	Level 2 of E
5	0.08	0.93	0.5	Level 2 of E
2	0.2	0.88	0.5	Level 2 of E
3	0.1333	0.92	0.5	Level 2 of E
4	0.1	0.99	1	Level 2 of E
1	0.4	0.93	0.5	Level 1 of E
3	0.1333	0.8	0.5	Level 1 of E
2	0.2	1.9	0.5	Level 1 of E
3	0.1333	1.15	1	Level 1 of E
5	0.08	1.24	1.5	Level 2 of E

9.8 Discussions

Design of Experiment (DOE) is a very effective approach for design optimization of the newly designed actuator. One important advantage is that we can include some parameters, which are not considered for equation formulation. The approach can generate an empirical mathematical model after analyzing all the data.

Chapter 10

Contributions and Future Work

10.1 Contributions

In this thesis, the dynamic behavior, kinematic formulation and experimentation of the newly designed actuator were discussed. The major contribution of this research includes the detailed analysis (kinematics and dynamics), design (SOLIDWORKS model) and control of the high performance linear actuator. Kinematic formulations are newly derived for this research. The Lagrangian based dynamic analysis is also not available for the rhombus networking. The Bond Graph model is unique and a chestnut contribution of the thesis. A DOE based optimal design approach is a new addition for linear actuator design.

Detailed control scheme of the actuator is provided in the thesis. We are controlling the motor at the base extremity.

The SOLIDWORKS model was newly designed for machine shop production of the actuator. Detailed component design of the actuator (Chapter 7), gives a clear idea about the industrial production design.

A statistical approach is provided to achieve the optimal design for a desired acceleration with a specified payload. Along with the conventional design approach, the statistical approach can be an efficient way to screen out refined parametric combinations for high performance.

The actuator performance was fully characterized by the computer simulations (Chapter 6 and Chapter 8) and validated by experimental set up (Chapter 8). The actuator possesses a very high peak acceleration of around 17g, which exceeded the initial design goal (10g).

The proposed actuator can be a good replacement of the current available prismatic or/and linear actuators for parallel robots, machine tools or any other machines.

Detailed analysis of the scissor lift mechanism gives a clear idea about their feasibility as a linear actuator. The dynamic model and the statistical analysis of the mechanism can be used for design purposes. This mechanism can be a good replacement of the conventional prismatic actuators.

10.2 Future Work

Performance of the newly designed actuator has been analyzed and its superior behavior is also investigated. The next step is to carry out further improvement of the structural design, material processing and control strategies. Overall mass of the actuator can be reduced by more efficient material selection. Detailed controller tuning procedures can be included to give the users a clear idea about precise operation with no overshoot. A better data acquisition system is needed for future work. High initial torque motor can be used, so that the actuator will not collapse under loaded condition.

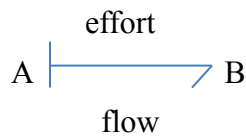
APPENDIX

Appendix A: Bond Graph and Motor Specifications

Bond Graph:

Bond graphs are a domain-independent graphical description of dynamic behavior of physical systems. This means that systems from different domains (e.g. electrical, mechanical, hydraulic, acoustical, thermodynamic, material) are described in the same way. The basis is that bond graphs are based on energy and energy exchange. Analogies between domains are more than just equations being analogous: the used physical concepts are analogous [54].

The language of bond graphs aspires to express general class physical systems through power interactions. The factors of power i.e., Effort and Flow have different interpretations in different physical domains. Yet, power can always be used as a generalized co-ordinate to model coupled systems residing in several energy domains [55].



Effort and Flow Variables for Different Physical Domains:

Systems	Effort (e)	Flow (f)
Mechanical	Force (F)	Velocity (v)
	Torque (τ)	Angular velocity (ω)
Electrical	Voltage (V)	Current (i)
Hydraulic	Pressure (P)	Volume flow rate (dQ/dt)
Thermal	Temperature (T)	Entropy change rate (ds/dt)
	Pressure (P)	Volume change rate (dV/dt)
Chemical	Chemical potential (μ)	Mole flow rate (dN/dt)
	Enthalpy (h)	Mass flow rate (dm/dt)
Magnetic	Magneto-motive force (e_m)	Magnetic flux (ϕ)

Zoltek Panex 33 Material Properties:

Physical Properties	Metric	English	Comments
Density	1.81 g/cc	0.0654 lb/in ³	
Mechanical Properties			
Tensile Strength, Ultimate	3800 MPa	551000 psi	Tow Tensile Test
Modulus of Elasticity	228 GPa	33100 ksi	In Tension; Tow Tensile Test
Electrical Properties			
Electrical Resistivity	0.00172 ohm-cm	0.00172 ohm-cm	
Component Elements Properties			
Carbon, C	95 %	95 %	

DC Motor Specifications (Maxon Model # 167131):

Values at nominal voltage	
Nominal voltage	48 V
No load speed	3100 rpm
No load current	194 mA
Nominal speed	2670 rpm
Nominal torque (max. continuous torque)	859 mNm
Nominal current (max. continuous current)	5.94 A
Stall torque	6820 mNm
Stall current	46.4 A
Max. efficiency	88 %
Characteristics	
Terminal resistance	1.03 Ω
Terminal inductance	0.82 mH
Torque constant	147 mNm/A
Speed constant	65 rpm/V
Speed / torque gradient	0.457 rpm/mNm
Mechanical time constant	3.98 ms
Rotor inertia	831 gcm ²
Thermal data	
Thermal resistance housing-ambient	1.3 K/W
Thermal resistance winding-housing	0.5 K/W
Thermal time constant winding	33.9 s
Thermal time constant motor	1200 s
Ambient temperature	-20...+100 °C
Max. winding temperature	+125 °C
Mechanical data	
Bearing type	ball bearings
Max. speed	7000 rpm
Axial play	0 - 0.14 mm
Max. axial load (dynamic)	24 N
Max. force for press fits (static)	390 N
(static, shaft supported)	6000 N

Gearhead Properties (Maxon Model # 110408):

General information	
Gearhead type	GP
Outer diameter	81 mm
Version	A
Gearhead Data	
Reduction	3.7 : 1
Absolute reduction	67/17
Max. motor shaft diameter	14 mm
Number of stages	1
Max. continuous torque	20 Nm
Max. intermittent torque	30 Nm
Direction of rotation, drive to output	=
Max. efficiency	80 %
Average backlash no load	0.5 °
Mass inertia	165 gcm ²
Gearhead length (L1)	92 mm
Max. transmittable power (continuous)	1700 W
Max. transmittable power (intermittent)	2500 W
Technical Data	
Radial play	max. 0.1 mm, 8 mm from flange
Axial play	max. 1 mm
Max. radial load	400 N, 24 mm from flange
Max. axial load (dynamic)	80 N
Max. force for press fits	1500 N
Max. continuous input speed	3000 rpm
Max. intermittent input speed	3000 rpm
Recommended temperature range	-30...+140 °C
Number of autoclave cycles	0
Product	
Weight	2300 g

Appendix B: Introduction to Design of Experiment (DOE) and Term Definitions

Design of Experiment:

This branch of applied statistics deals with planning, conducting, analyzing and interpreting controlled tests to evaluate the factors that control the value of a parameter or group of parameters. For DOE analysis Design Expert software has been used. In their online helpline there are lots of tutorials [56]. All the definitions are taken from website.

Aliased Terms:

Whenever there are fewer independent points in the design than there are terms in a model, there are parameters that cannot be estimated independently. The message for this aliased condition will be displayed prominently at several points in DESIGN-EXPERT so the user is aware that the model is inappropriate. Listings of confounded effects are known as Alias structure.

Confounded Effects:

Effects that cannot be estimated independently of each other: one is completely or partially correlated with the other.

Fractional Factorial:

An experimental design which includes only a subset of all possible combinations of factor levels, causing some of the effects to be confounded.

Resolution of a Design:

A measure of the degree of confounding for main effects (and interactions) in a fractional factorial design. In general, the resolution of a two-level fractional design is the length of the shortest-word in the defining relation. A design of resolution III confounds main effects with two-factor interactions. Resolution IV designs confound main effects with three-factor interactions and two factor interactions with other two-factor interactions. Resolution V designs confound main effects with four-factor interactions and two-factor interactions with three factor interactions.

Half Normal Plot:

The half-normal plot is used to select effects to be included in the model. Large effects (absolute values) appear in the upper-right section of the plot. The lower-left portion of the plot contains effects caused by noise rather than a true effect. Look for a noticeable gap between the large (model) effects, and the small (noise) effects. In many cases we will see a distinct inflection point or "dogleg" in the noise effects which indicate a transition between significant (model) and insignificant (noise) effects.

Pareto Chart:

The Pareto chart is an additional graphic used to display the t-values of the effects. Pareto Charts helps the reader to understand the effects better once the significant effects have been selected. Another use of the Pareto chart is to check for "one more significant effect" that was not obvious on the half-normal plot.

Box-Cox Plot:

The Box-Cox plot is a tool to help you determine the most appropriate power transformation to apply to response data.

Response Surface Methodology:

Response surface methodology (RSM) explores the relationships between several explanatory variables and one or more response variables. The method was introduced by G. E. P. Box and K. B. Wilson in 1951. The main idea of RSM is to use a sequence of designed experiments to obtain an optimal response. Box and Wilson suggest using a second-degree polynomial model to do this. They acknowledge that this model is only an approximation, but use it because such a model is easy to estimate and apply, even when little is known about the process.

Appendix C: Controller Specification and Sample MATLAB code

Controller Properties:

API Object Name	MotorControl
Motor Type	DC Motor
Number of Motor Ports	1
Velocity Resolution	0.39 % Duty Cycle
Acceleration Resolution	24.5 % Duty Cycle/s
Acceleration Min	24.5 % Duty Cycle/s
Acceleration Max	6250 % Duty Cycle/s
Acceleration Time Min	31.3 ms
Acceleration Time Max	8.2 s

Encoder Interface:

Number of Encoder Inputs	1
Count Rate Max	500000 cycles/s
Encoder Interface Resolution	x1
Update Rate	125 samples/s
Time Resolution	0.33 ms
Encoder Input Low Voltage Max	800 mV DC
Encoder Input High Voltage Min	2.1 V DC
Encoder Pull-up Resistance	2.4 k Ω

Electrical Properties:

Supply Voltage Min	9 V DC
Supply Voltage Max	28 V DC
Continuous Motor Current Max	5 A
Overcurrent Trigger	8 A
Current Consumption Min	20 mA
Current Consumption Max	100 mA
USB Speed	Full Speed

Physical Properties:

Recommended Wire Size (Power Terminal)	12 - 24 AWG
Operating Temperature Min	0 °C
Operating Temperature Max	70 °C

Analog Inputs:

Number of Analog Inputs	2
Input Impedance	900 k Ω
5V Reference Error Max	0.5 %
Update Rate	125 samples/s

Digital Inputs:

Number of Digital Inputs	2
Pull-up Resistance	15 k Ω
Low Voltage Max (True)	800 mV DC
High Voltage Min (False)	2.1 V DC
Low Voltage Trigger Length Min	4 s
High Voltage Trigger Length Min	16 s
Digital Input Voltage Max	\pm 15 V DC
Digital Input Update Rate	125 samples/s
Recommended Wire Size	16 - 26 AWG

Scissor Lift Height Formulation:

parameters

real global l;

real global H;

variables

real input;

equations

input=(H/(2*l));

output = arcsin(input);

Actuator Desired Length Calculation:

parameters

real global L;

real global H;

variables

real input;

equations

input=(H/(10*L));

output = 2*arccos(input);

Kinematic Simulation for Network # 3:

```
r=0.4;
%angular velocity from calculation
theta_dot=20.68;
%angular acceleration from calculation
alpha=-353.89;
%time required for one revolution
t_rev=2*pi/theta_dot;
%time
t=linspace(0,t_rev,200);
%required angle
theta=theta_dot*t;
%position calculation
x=6*r*cos(theta/2);
%linear velocity calculation
v=-3*r*theta_dot*sin(theta/2);
%linear acceleration calculation
a=(-3*r*alpha*sin(theta/2))-((3/2)*r*theta_dot^2*cos(theta/2));
% plot the figures
subplot(2,2,1)
plot(theta,x);
xlabel('Theta (radian)')
ylabel('Position (m)')
title('Position vs Input Angle')
subplot(2,2,2)
plot(t,v)
xlabel('Time (s)')
ylabel('Velocity (m/s)')
title('Linear Velocity vs Time')
subplot(2,2,3)
plot(t,a)
xlabel('Time (s)')
ylabel('Acceleration (m/s2)')
title('Linear Acceleration vs Time')
```

Link Position Calculation (Network # 5):

```
%Link Length%
l1=0.08;
l2=0.16;
l3=0.16;
l4=0.08;
l5=0.16;
l6=0.16;
l7=0.16;
l8=0.16;
l9=0.16;
l10=0.16;
l11=0.08;
l12=0.08;
%Link Angle in Radian%
theta1 = 2.9274;
theta2 = 0.2142;
theta3 = 2.9274;
theta4 = 0.2142;
theta5 = 0.2142;
theta6 = 2.9274;
theta7 = 2.9274;
theta8 = 0.2142;
theta9 = 0.2142;
theta10 = 2.9274;
theta11 = 0.2142;
theta12 = 2.9274;
%Position%
%Link1%
xg1=0.5*l1*cosd((180*theta1)/3.1416);
yg1=0.5*l1*sind((180*theta1)/3.1416);
%Link2%
xg2=l1*cosd((180*theta1)/3.1416)+0.5*l2*cosd((180*theta2)/3.1416);
yg2=l1*sind((180*theta1)/3.1416)+0.5*l2*sind((180*theta2)/3.1416);
%Link3%
xg3=l4*cosd((180*theta4)/3.1416)+0.5*l3*cosd((180*theta3)/3.1416);
yg3=l4*sind((180*theta4)/3.1416)+0.5*l3*sind((180*theta3)/3.1416);
%Link4%
xg4=0.5*l4*cosd((180*theta4)/3.1416);
yg4=0.5*l4*sind((180*theta4)/3.1416);
%Link5%
xg5=l4*cosd((180*theta4)/3.1416)+l3*cosd((180*theta3)/3.1416)+0.5*l5*cosd((180*theta5)/3.1416);
yg5=l4*sind((180*theta4)/3.1416)+l3*sind((180*theta3)/3.1416)+0.5*l5*sind((180*theta5)/3.1416);
%Link6%
xg6=l1*cosd((180*theta1)/3.1416)+l2*cosd((180*theta2)/3.1416)+0.5*l6*cosd((180*theta6)/3.1416);
yg6=l1*sind((180*theta1)/3.1416)+l2*sind((180*theta2)/3.1416)+0.5*l6*sind((180*theta6)/3.1416);
%Link7%
```

```

xg7=14*cosd((180*theta4)/3.1416)+13*cosd((180*theta3)/3.1416)+15*cosd((
180*theta5)/3.1416)+0.5*17*cosd((180*theta7)/3.1416);
yg7=14*sind((180*theta4)/3.1416)+13*sind((180*theta3)/3.1416)+15*sind((
180*theta5)/3.1416)+0.5*17*sind((180*theta7)/3.1416);
%Link8%
xg8=11*cosd((180*theta1)/3.1416)+12*cosd((180*theta2)/3.1416)+16*cosd((
180*theta6)/3.1416)+0.5*18*cosd((180*theta8)/3.1416);
yg8=11*sind((180*theta1)/3.1416)+12*sind((180*theta2)/3.1416)+16*sind((
180*theta6)/3.1416)+0.5*18*sind((180*theta8)/3.1416);
%Link9%
xg9=14*cosd((180*theta4)/3.1416)+13*cosd((180*theta3)/3.1416)+15*cosd((
180*theta5)/3.1416)+17*cosd((180*theta7)/3.1416)+0.5*19*cosd((180*theta
9)/3.1416);
yg9=14*sind((180*theta4)/3.1416)+13*sind((180*theta3)/3.1416)+15*sind((
180*theta5)/3.1416)+17*sind((180*theta7)/3.1416)+0.5*19*sind((180*theta
9)/3.1416);
%Link10%
xg10=11*cosd((180*theta1)/3.1416)+12*cosd((180*theta2)/3.1416)+16*cosd(
(180*theta6)/3.1416)+18*cosd((180*theta8)/3.1416)+0.5*110*cosd((180*the
ta10)/3.1416);
yg10=11*sind((180*theta1)/3.1416)+12*sind((180*theta2)/3.1416)+16*sind(
(180*theta6)/3.1416)+18*sind((180*theta8)/3.1416)+0.5*110*sind((180*the
ta10)/3.1416);
%Link11%
xg11=11*cosd((180*theta1)/3.1416)+12*cosd((180*theta2)/3.1416)+16*cosd(
(180*theta6)/3.1416)+18*cosd((180*theta8)/3.1416)+110*cosd((180*theta10
)/3.1416)+0.5*111*cosd((180*theta11)/3.1416);
yg11=11*sind((180*theta1)/3.1416)+12*sind((180*theta2)/3.1416)+16*sind(
(180*theta6)/3.1416)+18*sind((180*theta8)/3.1416)+110*sind((180*theta10
)/3.1416)+0.5*111*sind((180*theta11)/3.1416);
%Link12%
xg12=14*cosd((180*theta4)/3.1416)+13*cosd((180*theta3)/3.1416)+15*cosd(
(180*theta5)/3.1416)+17*cosd((180*theta7)/3.1416)+19*cosd((180*theta9)/
3.1416)+0.5*112*cosd((180*theta12)/3.1416);
yg12=14*sind((180*theta4)/3.1416)+13*sind((180*theta3)/3.1416)+15*sind(
(180*theta5)/3.1416)+17*sind((180*theta7)/3.1416)+19*sind((180*theta9)/
3.1416)+0.5*112*sind((180*theta12)/3.1416);

%End Effector Position%
xg_e=11*cosd((180*theta1)/3.1416)+12*cosd((180*theta2)/3.1416)+16*cosd(
(180*theta6)/3.1416)+18*cosd((180*theta8)/3.1416)+110*cosd((180*theta10
)/3.1416)+111*cosd((180*theta11)/3.1416);
yg_e=11*sind((180*theta1)/3.1416)+12*sind((180*theta2)/3.1416)+16*sind(
(180*theta6)/3.1416)+18*sind((180*theta8)/3.1416)+110*sind((180*theta10
)/3.1416)+111*sind((180*theta11)/3.1416);

```

MATLAB Function for Control SIMULINK Model:

```
function y = fcnarmdynamics(u)
m1=0.216;
m2=0.216;
m3=0.216;
m4=0.216;
l1=0.4;
l2=0.4;
l3=0.4;
l4=0.4;
%g=9.81;

torque=u(1);
theta=u(2);
%dtheta=u(3);

M=((m1+3*m2)/6)*(l1^2)+m2*((l2^2)/6)+((m2*l1*l2)/2)*cos(theta)+
m3*((l3)^2/6)+ m3*((l2*l4*cos(theta))/2)+((m4+3*m3)/6)*(l4^2);
M_inverse=inv(M);

%N=[-m2*a1*a2*sin(theta1)*(dtheta1*dtheta2+((dtheta2)^2/2));
(m2/2)*a1*a2*((dtheta1)^2/2)*sin(theta2)]; %without friction
%N=[-
m2*a1*a2*sin(theta1)*(dtheta1*dtheta2+((dtheta2)^2/2))+ (0.1*dtheta1);
(m2/2)*a1*a2*((dtheta1)^2/2)*sin(theta2)+(0.1*dtheta1)]; %with friction

%G=[((m1+m2)/2)*g*a1*cos(theta1)+(m2/2)*g*a2*cos(theta1+theta2);
m2*g*(a2/2)*cos(theta1+theta2)];
y = M_inverse*(torque); %#ok<*MINV>
```

References

- [1] J. P. Merlet (2006), *Parallel Robots*, Second Edition, Springer, INRIA, France.
- [2] B. Yao, Y. Hong, C. Hu, and Q. Wang, “Precision motor control of linear motor drive systems for micro/nano-positioning,” *Micro Nano China 2007*, January 2007, Sanya, Haina, China.
- [3] Gough, V. E. and Whitehall, S. G. (1962), “Universal tyre testing machine”, *Proceedings of the 9th International Automobile Technical Congress, discussion*, Federation Internationale des Societes d Ingenieurs des Techniques de Automobile (FISITA) (Ed. G. Eley), (IMechE 1, London, UK), pp. 117137.
- [4] Rolland, L. 2010, “Kinematic Synthesis of a New Generation of Rapid Linear Actuator for High Velocity Robotics”, *Advanced Strategies for Robot Manipulators*, S. Ehsan Shafiei (Ed.), ISBN: 978-307-099-5.
- [5] A. Alleyne, “Nonlinear force control of an electro hydraulic actuator,” *In proc. Japan/USA Symposium, Flexible Automation*, Boston, MA, 1996, pp. 193-200.

- [6] N. Niksefat, N Sepheri, “ Designing Robust Force Control of Hydraulic Actuator’s Despite systems and Environmental Uncertainties”, *IEEE control system Magazine*, 2001, pp. 66-77.
- [7] Conrad and C.J.D. Jensen, “Design of hydraulic force control systems with state estimate feedback,” *In Proc. IFAC 10th Triennial Congress*, Munich, Germany, 1987, pp. 307-312.
- [8] N. Niksefat and N. Sepehri, “Robust force controller design for an electro hydraulic actuator based on nonlinear model,” *In Proc. IEEE Conf. Robotics and Automation*, Detroit, MI, 1999, pp. 200-206.
- [9] Altare, A. Vacca, C. Ritcher, “A Novel Design for an Efficient and Compact Electro-hydraulic Actuator”, *IEEE Aerospace Conference*, May 2014, MT, USA.
- [10] Wang, J., Pu, J. and Moore, P.R. (1997), “A practicable control strategy for servo pneumatic actuator systems”, *Control Eng. Pract.*, Vol. 7, pp. 1483-8.
- [11] C. Kim, J. H. Chung, “Application of an active pneumatic actuator to robotic deburring”, *Industrial Robotics: An International Journal*, vol. 34/6, pp. 487-494, 2007.

- [12] Okamura M., Ohshige T. and Watanabe M., “High Speed and High Accuracy XY-Stage for Electronic Assembly”, *Fourth IEEE/CHMT European International Electronic Manufacturing Technology Symposium*, Proceedings, pp.104-107, 1988.
- [13] Meisser C., Eggenschwiler H. and Nehls W., “Einrichtung zur Durchführung der Zustellbewegung eines Arbeitsorgans zu einer Arbeitsstation”, *European Patent Application No. 0317787B1*, ESEC SA, 1988.
- [14] T. Niino, S. Egawa and T. Higuchi, “High-Power and High efficiency Electrostatic Actuator”, *Proc. 1993 IEEE Workshop on Micro Electro Mechanical Systems*, (1993) 236-241.
- [15] T. Niino, T. Higuchi and S. Egawa, “Dual Excitation Multiphase Electrostatic Drive”, *Proc. 1995 IEEE IAS annual meeting (1995)*, pp. 1318-1325.
- [16] R. M. Robinson, C. S. Kothera, B. K. S. Woods, R. D. Vockee and N. M. Wereley, “High Specific Power Actuators for Robotic Manipulators”, *Journal of Intelligent Material Systems and Structure*, vol. 22, 2011, pp. 1501-1511.
- [17] Klute, G., Czerniecki, J. and Hannaford, B., “Artificial Muscles: Actuators for Bio-robotic Systems,” *International Journal of Robotics Research* (2002), 21:295_309.

[18] Lightner, S. and Lincoln, R., “The Fluidic Muscle: A ‘New’ Development,” *The International Journal of Modern Engineering*, 2002, 2:8 pages.

[19] Woods, B.K.S., Gentry, M., Kothera, C.S., and Wereley, N.M., "Fatigue Life Testing of Swaged Pneumatic Artificial Muscles for Aerospace Morphing Applications," *51st AIAA/ASME/ASCE/AHS/ASC Structures, Structural Dynamics, and Materials Conference*, 12-15 April 2010, Orlando, FL, AIAA 2010_2662.

[20] www.wikipedia.org

[21] K. Takemura, H. Kozuki, K. Edamura and S. Yokota, “A micromotor using electro-conjugate fluid - Improvement of motor performance by using saw-toothed electrode series”, *Sensors and Actuators A: Physical*, 140 (2007) 131-137.

[22] Baughman, Ray H., Cui, Changxing, Zakhidov, Anvar A., Iqbal, Zafar, Barisci, Joseph N., Spinks, Geoff M., Wallace, Gordon G., Mazzoldi, Alberto, de Rossi, Danilo, Rinzler, Andrew G., Jaschinski, Oliver, Roth, Siegmund, Kertesz, Miklos, “Carbon nanotube actuators”, *Science*, 284(5418), 1999.

[23] K. Uchino, “Piezoelectric Actuators 2006”, *Journal of Electro ceramics*, August 2008, Volume 20, Issue 3-4, pp 301-311.

[24] Y. Okamoto, R. Yoshida, H. Sueyoshi, *Konica Minolta Tech. Report 1*, 23 (2004).

- [25] S. Kawashima, O. Ohnishi, H. Hakamata, S. Tagami, A. Fukuoka, T. Inoue, S. Hirose, *Proc. IEEE Int'l Ultrasonic Symp.*, 1994, France (1994).
- [26] K. Uchino, “*Piezoelectric Actuators and Ultrasonic Motors*”, (Kluwer, Norwell, MA 1996).
- [27] K. Uchino, “*Ferroelectric Devices*” (CRC, Dekker, NY, 2000).
- [28] K. Uchino, “*Micromechatronics*” (CRC, Dekker, NY 2003).
- [29] Clavel R., “DELTA, a Fast Robot with Parallel Geometry”, *Int. Symp. On Industrial Robots (ISIR)*, pp. 91-100, 1988.
- [30] J. C. Compter, “Electro-dynamic planar motor,” *Precision Eng.*, vol. 28, no. 2, pp. 171–180, Apr. 2004.
- [31] W. J. Kim, D. L. Trumper, and J. H. Lang, “Modeling and vector control of a planar magnetic levitator,” *IEEE Trans. Ind. Appl.*, vol. 34, no. 6, pp. 1254–1262, Nov./Dec. 1998.
- [32] A. J. Hazelton, M. B. Binnard, and J. M. Gery, “Electric motors and positioning devices having moving magnet arrays and six degrees of freedom,” *U.S. Patent 6 208 045*, Mar. 27, 2001.

- [33] N. Korenaga, "Alignment apparatus and exposure apparatus using thesame," *U.S. Patent 7 075 198*, Jul. 11, 2006.
- [34] J. C. Compter, P. C. M. Frissen, and J. van Eijk, "Displacement device," *Patent WO 2006/075 291 A2*, Jul. 20, 2006.
- [35] C. M. M. van Lierop, J. W. Jansen, A. A. H. Damen, and P. P. J. van den Bosch, "Control of multi-degree-of-freedom planar actuators," *In Proc. IEEE Int. CCA*, Munich, Germany, Oct. 2006, pp. 2516–2521.
- [36] F. Baronti, A. Lazzeri, F. Lenzi, R. Roncella, R. Saletti, and S. Saponara, "Voice Coil Actuators: From Model and Simulation to Automotive Application," *35th Annual IEE Conference on Industrial Electronics (IECON'09)*, 2009, pp. 1805-1810.
- [37] W. Robertson, B. Cazzolato, and A. Zander, "Parameters for Optimizing the Forces Between Linear Multipole Magnetic Arrays," *IEEE Magnetic Letters*, Vol. 1, 2010.
- [38] X.M. Feng, Z.J. Duan, Y. Fu, and A.L. Sun, "The technology and Application of Voice Coil Actuator," *2nd International Conference on Mechanical Automation and Control Engineering (MACE)*, 2011, pp. 892-895.

- [39] K. Tsuchiya, Y. Todaka and M. Umemoto, “TEM Investigation of Intermediate Phase Transformation and Micro modulation in Ni–Mn–Ga Ferromagnetic Shape memory Alloys”, *Mater. Sci. Tech.*, 24 (2008) 920-926.
- [40] Y. Okimori, T. Inamura, H. Hosoda and K. Wakashima, “Diffusion Bonding of Co to TiAu High Temperature Shape Memory Alloy”, *Materials Transactions*, 49 (2008) 1998-2005.
- [41] T. Higuchi, A. Horikoshi and T. Komori, “Development of an actuator for super clean rooms and ultra-high vacuum”, *Proc. of 2nd International Symposium on Magnetic Bearings*, Tokyo, Japan, (1990) 115-122.
- [42] Yasui, A. Yamamoto and T. Higuchi, “Non-Contact Levitation control System for Electrostatic Motor”, *Proc. Of 8th International Symposium on Magnetic Bearings*, Mito, Japan, (2002), pp. 175-180.
- [43] Scheiner, C. (1631), “*Pantographice, seu ars delineandi res quaslibet per parallelogrammum lineare seu cavum, mechanicum, mobile*. Romae: Ex typographia Ludouici Grignani, sumptibus Hermanni Scheus, vol. 12, 108 pages.
- [44] <https://www.cs.cmu.edu/~rapidproto/mechanisms/chpt5.html>

- [45] Moon, F.C. (2007) *The Machines of Leonardo Da Vinci and Franz Reuleaux*. Volume on Kinematics of Machines from the Renaissance to the 20th Century, Series on History of Mechanism and Machine Science, Springer Netherlands, 417 pages.
- [46] Reuleaux, F. (1876) *Kinematics of Machinery: Outlines of a Theory of Machines*. Macmillan and Co., London.
- [47] Ren G. Dong, Christopher S. Pan, Jared J. Hartsell, Daniel E. Welcome, Tim Lutz, Anne Brumfield, James R. Harris, John Z. Wu, Bryan Wimer, Victor Mucino, Kenneth Means, “An Investigation on the Dynamic Stability of Scissor Lift.”
- [48] Geoff Rideout and Jeffrey L. Stein, “An Energy-Based Approach to Parameterizing Parasitic Elements for Eliminating Derivative Causality”, *International Conference on Bond Graph Modeling (ICBGM' 2003)*.
- [49] Tao Liu¹, Jian Sun, “Simulative Calculation and Optimal Design of Scissor Lifting Mechanism,” *2009 Chinese Control and Decision Conference (CCDC 2009)*.
- [50] Lung-Wen Tsai (1999), “*Robot analysis: the mechanics of serial and parallel manipulators*”, Wiley, New York.
- [51] http://web.mit.edu/emech/dontindex-build/full-text/emechbk_8.pdf

[52] www.phidgets.com

[53] T. Rahman, D. Hicks, M. R. Hossain, and Nicholas Krouglicof, “Digital Hardware Implementation of an Active Disturbance Rejection Controller for a Highly Dynamic Parallel Orientation Manipulator”, *2014 IEEE International Conference on Robotics & Automation (ICRA)*, Hong Kong Convention and Exhibition Center, May 31 - June 7, 2014. Hong Kong, China

[54] Jan F. Broenink, “Introduction to Physical Systems Modelling with Bond Graphs”, University of Twente, Dept EE, Control Laboratory.

[55] www.bondgraphs.com

[56] <http://www.statease.com/dx9.html>